NATIONAL TECHNICAL UNIVERSITY OF ATHENS

SCHOOL OF CHEMICAL ENGINEERING
DEPARTMENT I: DEPARTMENT OF CHEMICAL SCIENCES

DOCTORAL DISSERTATION

DIFFUSION STUDIES OF FLUIDS IN MESOPOROUS AND NANOPOROUS MATERIALS USING NUCLEAR MAGNETIC RESONANCE (NMR) METHODS

LYDIA GKOURA

ATHENS

2019

ΕΘΝΙΚΟ ΜΕΤΣΟΒΙΟ ΠΟΛΥΤΕΧΝΕΙΟ

ΣΧΟΛΗ ΧΗΜΙΚΩΝ ΜΗΧΑΝΙΚΩΝ
ΤΟΜΕΑΣ Ι: ΧΗΜΙΚΩΝ ΕΠΙΣΤΗΜΩΝ

ΔΙΔΑΚΤΟΡΙΚΗ ΔΙΑΤΡΙΒΗ

ΜΕΛΕΤΗ ΤΗΣ ΔΙΑΧΥΣΗΣ ΡΕΥΣΤΩΝ ΣΕ ΜΕΣΟΠΟΡΩΔΗ ΚΑΙ ΝΑΝΟΠΟΡΩΔΗ ΣΥΣΤΗΜΑΤΑ ΜΕ ΜΕΘΟΔΟΥΣ ΠΥΡΗΝΙΚΟΥ ΜΑΓΝΗΤΙΚΟΥ ΣΥΝΤΟΝΙΣΜΟΥ (NMR)

ΛΥΔΙΑ ΓΚΟΥΡΑ

ΑΘΗΝΑ

2019

DOCTORAL DISSERTATION

Diffusion Studies Of Fluids in Mesoporous and Nanoporous Materials using Nuclear Magnetic Resonance (NMR) Methods

Lydia K. Gkoura

THREE-MEMBER ADVISORY COMMITTEE:
Margarita Beazi-Katsioti, Professor NTUA **(Supervisor)**
Dimitrios Karonis, Professor NTUA
George Papavassiliou, Researcher A – Director of research NCSR Demokritos

SEVEN-MEMBER EXAMINATION COMMITTEE

Margarita Beazi-Katsioti,
Professor NTUA

Dimitrios Karonis,
Professor NTUA

George Papavassiliou,
Researcher A – Director of research
NCSR Demokritos

Dimitrios Gournis,
Professor UoI

Konstantina Kollia,
Professor NTUA

George Romanos,
Researcher A – Director of research NCSR
Demokritos

Michael Fardis,
Researcher A – Director of research
NCSR Demokritos

Examination Date 05/07/2019

ΔΙΔΑΚΤΟΡΙΚΗ ΔΙΑΤΡΙΒΗ

Μελέτη της Διάχυσης Ρευστών σε Μεσοπορώδη και Νανοπορώδη Συστήματα με Μεθόδους Πυρηνικού Μαγνητικού Συντονισμού (NMR)

ΛΥΔΙΑ ΚΩΝΣΤΑΝΤΙΝΟΥ ΓΚΟΥΡΑ

ΤΡΙΜΕΛΗΣ ΣΥΜΒΟΥΛΕΥΤΙΚΗ ΕΠΙΤΡΟΠΗ:

Μαργαρίτα Μπεάζη-Κατσιώτη, Καθηγήτρια Ε.Μ.Π **(Επιβλέπουσα)**
Δημήτριος Καρώνης, Καθηγητής Ε.Μ.Π
Γεώργιος Παπαβασιλείου, Ερευνητής Α΄ ΕΚΕΦΕ Δημόκριτος – Διευθυντής Ερευνών

ΕΠΤΑΜΕΛΗΣ ΕΞΕΤΑΣΤΙΚΗ ΕΠΙΤΡΟΠΗ

Μαργαρίτα Μπεάζη-Κατσιώτη,
Καθηγήτρια Ε.Μ.Π

Δημήτριος Καρώνης,
Καθηγητής Ε.Μ.Π

Γεώργιος Παπαβασιλείου,
Ερευνητής Α΄ ΕΚΕΦΕ Δημόκριτος –
Διευθυντής Ερευνών

Δημήτρης Γουρνής
Καθηγητής Πανεπιστήμιο
Ιωαννίνων

Κωνσταντίνα Κόλλια
Καθηγήτρια Ε.Μ.Π.

Γεώργιος Ρωμανός
Ερευνητής Α΄ ΕΚΕΦΕ Δημόκριτος –
Διευθυντής Ερευνών

Μιχαήλ Φαρδής
Ερευνητής Α΄ ΕΚΕΦΕ Δημόκριτος –
Διευθυντής Ερευνών

Ημερομηνία εξέτασης 05/07/2019

«Η έγκριση της διδακτορικής διατριβής από την Ανωτάτη Σχολή Χημικών Μηχανικών του Ε.Μ.Πολυτεχνείου δεν υποδηλώνει αποδοχή των γνωμών του συγγραφέα. (Ν. 5343/1932, ΄Αρθρο 202)».

ΠΕΡΙΛΗΨΗ

Η διατριβή αυτή αφορά τις μετρήσεις συντελεστή αυτοδιάχυσης (D) μέσω μεθόδων πυρηνικού μαγνητικού Συντονισμού (NMR). Οι μετρήσεις πραγματοποιήθηκαν σε δυο κατηγορίες υλικών: νερό περιορισμένο σε νανοσωλήνες άνθρακα καθώς και ιοντικό υγρό περιορισμένο σε δυο μεσοπορώδη δομές.

Οι νανοσωλήνες άνθρακα (CNTs Carbon Nanotubes) έχουν προσελκύσει το ενδιαφέρον των ερευνητών σε παγκόσμιο επίπεδο, λόγω των πολυάριθμων εφαρμογών τους σε ένα ευρύ φάσμα πεδίων που εκτείνεται από την ιατρική και τη φαρμακευτική ως την ενέργεια και το περιβάλλον και από την ηλεκτρονική και τις τηλεπικοινωνίες ως τη βιομηχανία και την αεροδιαστημική. Επιπλέον, το συμμετρικό σχήμα και η υψηλή μηχανική, χημική και θερμική σταθερότητά τους εξασφαλίζουν καλά καθορισμένες ιδιότητες μεταφοράς και καθιστούν τους CNTs ιδανικά πρότυπα συστήματα για τη μελέτη φαινομένων μεταφοράς σε περιορισμένες γεωμετρίες με διαστάσεις στη νανοκλίμακα. Κατά συνέπεια η μελέτη της διάχυσης του ύδατος σε νανοσωλήνες άνθρακα είναι ιδιαίτερα χρήσιμη στις προσπάθειες κατανόησης της ροής νερού μέσω υδρόφοβων νανοδιαύλων για την αξιοποίηση των CNTs ως δομικά στοιχεία σε διατάξεις τεχνολογίας νέας γενιάς. Αρκετές μελέτες, στην πλειοψηφία τους θεωρητικές, έχουν διεξαχθεί μέχρι σήμερα προκειμένου να διερευνηθεί η αλληλεπίδραση μεταξύ του νερού και της επιφάνειας των νανοσωλήνων άνθρακα (CNTs). Ωστόσο, οι πειραματικές μελέτες είναι ακόμα ολιγάριθμες και έχουν περιορισμένες δυνατότητες με αποτέλεσμα να εξακολουθούν να υπάρχουν αμφιλεγόμενα αποτελέσματα.

Τα τελευταία χρόνια το ενδιαφέρον της επιστημονικής κοινότητας έχει επικεντρωθεί στην ιδιάζουσα συμπεριφορά που παρουσιάζει η ροή νερού μέσα από υδρόφοβους CNTs. Πρόσφατες θεωρητικές και πειραματικές μελέτες καταδεικνύουν ότι τα μόρια του νερού, όταν περιορίζονται σε νανοδιαύλους με διαστάσεις συγκρίσιμες με το μέγεθός τους, εμφανίζουν ιδιόρρυθμη συμπεριφορά, με κύριο χαρακτηριστικό την εξαιρετικά αυξημένη ροή νερού. Η ιδιόμορφη ροή στο εσωτερικό των νανοσωλήνων αποτυπώνεται στις τιμές του συντελεστή αυτοδιάχυσης D των πρωτονίων του νερού, που βρέθηκαν να είναι μεγαλύτερες από το συντελεστή D του ελεύθερου νερού για τα μόρια που κινούνται κατά μήκος του άξονα στο κέντρο των σωλήνων. Το φαινόμενο αυτό έχει ιδιαίτερα σημαντικό αντίκτυπο σε πολλές εφαρμογές των CNTs, από την εστιασμένη χορήγηση φαρμάκων μέχρι τις μεμβράνες νέας γενιάς, οι οποίες απαιτούν την παροχή υγρών, κυρίως υδατικών διαλυμάτων, μέσω του εσωτερικού των νανοσωλήνων άνθρακα.

Ο Πυρηνικός Μαγνητικός Συντονισμός NMR θεωρείται μια από τις πιο σημαντικές μη επεμβατικές τεχνικές για την μελέτη συμπεριφοράς ρευστών περιορισμένων σε μεσοπορώδη και νανοπορώδη στερεά συστήματα. Βασίζεται στην αλληλεπίδραση των πυρηνικών σπίν με ένα εξωτερικό μαγνητικό πεδίο, καθώς και στην αλληλεπίδραση των πυρηνικών σπίν με τα γειτονικά πυρηνικά και μη συζευγμένα ηλεκτρονικά σπίν. Αυτό την καθιστά εξαιρετικά ευαίσθητη στο τοπικό ατομικό περιβάλλον, επιτρέποντας τη μελέτη της ατομικής και μοριακής δυναμικής σε χρονικές κλίμακες που εκτείνονται από νανοδευτερόλεπτα έως και ώρες ή ακόμα και εβδομάδες ή μήνες.

Η εφαρμογή των συμβατικών τεχνικών Πυρηνικού Μαγνητικού Συντονισμού μίας διάστασης (1D-NMR) για την μελέτη της μοριακής δυναμικής των ρευστών περιλαμβάνει την παρακολούθηση και καταγραφή της φασματικής γραμμής, των χρόνων εφησυχασμού T_1 (σπίν-πλέγματος) και T_2 (σπίν-σπίν) και της σταθεράς αυτοδιάχυσης D των εξεταζόμενων πυρήνων. Προκύπτουν σημαντικές πληροφορίες για την κινηματική και τις αλληλεπιδράσεις τόσο σε ατομικό επίπεδο στο τοπικό περιβάλλον των πυρήνων όσο και για συλλογικές κινήσεις. Έτσι, από πειραματικές μελέτες ^{1}H 1D-NMR των πρωτονίων (^{1}H) στα μόρια του νερού συλλέγονται πληροφορίες για τους πιθανούς μηχανισμούς διάχυσης του νερού στο εσωτερικό των CNTs. Οι τεχνικές 1D-NMR όμως δεν μπορούν να διαχωρίσουν πιθανές διαφορετικές συνεισφορές στη μοριακή διάχυση ή στους μηχανισμούς εφησυχασμού ούτε να διακρίνουν τις πιθανές συσχετίσεις μεταξύ των διακριτών συνεισφορών.

Στην παρούσα διατριβή πραγματοποιούνται για πρώτη φορά πειραματικές μετρήσεις μέσω των οποίων έγινε δυνατό να διακριθούν διαφορετικές συνιστώσες στη ροή του νερού στο εσωτερικό των νανοσωλήνων εφαρμόζοντας μια πρωτοποριακή μέθοδο που συνδυάζει τεχνικές (D-T_2 και T_1 -T_2) της φασματοσκοπίας Πυρηνικού Μαγνητικού Συντονισμού δύο διαστάσεων 2D-NMR με προηγμένους αλγορίθμους αντιστροφής Tikhonov. Στην επεξεργασία των πειραματικών δεδομένων, εφαρμόστηκαν προηγμένοι αλγόριθμοι αντιστροφής δύο διαστάσεων, ώστε να προσδιοριστούν η κατανομή του συντελεστή αυτοδιάχυσης D του νερού και να συσχετιστεί με τις αντίστοιχες κατανομές των χρόνων T_1, T_2.

Αρχικά μελετήθηκαν η διάχυση νερού μέσα σε CNTs με μονό και διπλό τοίχωμα (SWCNT και DWCNT). Η μέθοδος αυτή έδωσε τη δυνατότητα να παρατηρήσουμε πειραματικά τη διάχυση του νερού στη νανοκλίμακα και να διακριθούν ομάδες μορίων μέσω θερμοκρασιακών μετρήσεων από 265K έως 300K με διαφορετική δυναμική-κινηματική συμπεριφορά. Παρατηρήθηκε ότι κατά τη ροή νερού μέσα από CNTs το τοπικό περιβάλλον δεν είναι το ίδιο για όλα τα μόρια του ρευστού. Σε κάθε περίπτωση οι μηχανισμοί εφησυχασμού και διάχυσης καθορίζονται από το τοπικό περιβάλλον και τις αλληλεπιδράσεις των μορίων, με αποτέλεσμα η κάθε ομάδα μορίων νερού να δίνει ένα ξεχωριστό σήμα NMR με διαφορετικό συντελεστή αυτοδιάχυσης. Παρατηρήθηκε μια κατανομή τιμών των χρόνων εφησυχασμού και της σταθεράς διάχυσης που αντανακλά την κατανομή μορίων νερού σε διαφορετικά δυναμικά περιβάλλοντα στα τοιχώματα και στο εσωτερικό των νανοσωλήνων.

Με την μέθοδο που αναπτύχθηκε στην παρούσα διατριβή έγινε δυνατό να παρατηρηθούν για πρώτη φορά πειραματικά διαφορετικές ομάδες νερού στα τοιχώματα και κατά μήκος του άξονα των νανοσωλήνων και να επιβεβαιωθούν για πρώτη φορά πειραματικά οι προβλέψεις των θεωρητικών μοντέλων (MD Molecular Dynamics). Η πειραματική μέθοδος NMR που αναπτύχθηκε υπερτερεί έναντι των θεωρητικών υπολογισμών MD λόγου του ότι η χρονική κλίμακα των πειραμάτων διάχυσης NMR είναι 2-3 τάξεις μεγέθους μεγαλύτερη από την αντίστοιχη κλίμακα της μεθόδου MD. Το γεγονός αυτό επέτρεψε την παρακολούθηση πολύ αργών κινήσεων ούτως ώστε να μελετηθεί η ιδιόμορφη διάχυση του νερού εντός των νανοσωλήνων άνθρακα. Οπότε εφαρμόζοντας την τεχνική 2D D-T_2 και T_1-T_2 ^{1}H NMR σε SWCNT και DWCNT νανοσωλήνες παρατηρήθηκε μια πολυστρωματική δομή στη διάχυση του νερού στους DWCNTs και την παρουσία μιας «γρήγορης» συνιστώσας διάχυσης που απεικονίζει τη ροή μορίων νερού κατά μήκος του κεντρικού άξονα του νανοσωλήνα.

Σε δεύτερο στάδιο της παρούσας διατριβής πραγματοποιήθηκαν πειραματικές μετρήσεις με την ιδια μεθοδολογία σε νανοσωλήνες άνθρακα με διαφορετικές τιμές εσωτερικής διαμέτρου από 1.1 nm ως 6 nm στην περιοχή θερμοκρασιών από τους 265K ως τους 300K, με σκοπό να αποσαφηνιστεί ο ρόλος που παίζει το μέγεθος της διαμέτρου στο μηχανισμό διάχυσης του νερού. Πραγματοποιήθηκε πειραματικά ο προσδιορισμός μίας βέλτιστης διαμέτρου μεταξύ 3.0nm-4.5nm για την οποία μεγιστοποιείται η ταχύτητα ροής των μορίων νερού στους CNTs.

Επιπλέον, τα αποτελέσματά υποδεικνύουν ότι σε αυτές τις διαμέτρους το νερό στα CNTs αναλύεται περαιτέρω σε δύο συνιστώσες διάχυσης με την κεντρική κατά μήκος του άξονα του νανοσωλήνα να παρουσιάζει εκπληκτικές ιδιότητες μεταφοράς, όπως αναφέρθηκε και νωρίτερα, με τιμές D κυμαινόμενες από δύο έως σχεδόν τέσσερις φορές μεγαλύτερες από τις τιμές D του ελεύθερου νερού.

Στο τελευταίο στάδιο της παρούσας διατριβής μελετήθηκε σε ένα μεγάλο εύρος θερμοκρασιών η συμπεριφορά ενός ιοντικού υγρού σε υγρή μορφή καθώς και προσροφημένο σε δυο μεσοπορώδεις δομές.

Τα ιοντικά υγρά (ΙΥ) είναι άλατα με αρκετά χαμηλό σημείο τήξεως, μικρότερο από 100^{o}C, τα οποία φέρουν οργανικά κατιόντα, που είναι ογκώδη και μικρής συμμετρίας, ενώ τα ανιόντα τους μπορεί να είναι ανόργανα ή οργανικά. Αυτά τα άλατα συναντώνται συνήθως ως υγρά σε θερμοκρασία δωματίου, οπότε αναφέρονται ως ιοντικά υγρά θερμοκρασίας δωματίου (Room Temperature Ionic Liquids, RTILs). Οι ενδιαφέρουσες φυσικοχημικές ιδιότητές τους, ο διαφορετικός τρόπος συμμετοχής τους (ως διαλύτες) σε αντιδράσεις και η σημαντική ικανότητα δέσμευσης ορισμένων αερίων, όπως το CO_2, έχουν προσελκύσει ιδιαίτερα έντονο ερευνητικό ενδιαφέρον. Τα ιοντικά υγρά (ΙΥ) υπερτερούν έναντι των συμβατικών διαλυτών για τη δέσμευση του CO_2 και διαθέτουν φιλική προς το περιβάλλον συμπεριφορά, καθώς έχουν μεγάλη περιοχή θερμοκρασιών υγρής κατάστασης και χαρακτηρίζονται από αμελητέα τάση ατμών και πτητικότητα. Συστήματα υποστηριζόμενης φάσης ιοντικών υγρών (ιοντικά υγρά μέσα σε μεσοπορώδη δομές) έχουν πολλαπλές εφαρμογές όπως σε διεργασίες δέσμευσης και διαχωρισμού αερίων, διεργασίες κατάλυσης, λιπαντικά, νανοσύνθετα υλικά, πυκνωτές, καύσιμα κ.α. Η απόδοση όλων αυτών των διεργασιών εξαρτάται κυρίως από την ιοντική μεταφορά των ιοντικών υγρών στη νανοκλίμακα. Η φασματοσκοπία Πυρηνικού Μαγνητικού Συντονισμού (NMR) έχει αποδειχθεί ότι είναι ένα πολύ σημαντικό μη επεμβατικό εργαλείο για τη διερεύνηση της δυναμικής και των ιδιοτήτων των ILs. Συγκεκριμένα, πειράματα NMR στην γραμμική περιοχή βαθμίδας πεδίου υπεραγώγιμου μαγνήτη επιτρέπουν τον άμεσο υπολογισμό του συντελεστή αυτοδιάχυσης D.

Πραγματοποιήθηκαν θερμοκρασιακές μετρήσεις πρωτονίου ^{1}H NMR με συμβατικές μονοδιάστατες και δισδιάστατες τεχνικές Πυρηνικού Μαγνητικού Συντονισμού καθώς και μετρήσεις των χρόνων εφησυχασμού T_1 (σπίν-πλέγματος), και T_2 (σπίν-σπίν) και της σταθεράς αυτοδιάχυσης D στο ιοντικό υγρό BMIM TCM σε ελεύθερη μορφή καθώς και προσροφημένο σε δύο πορώδη δομές πυριτίου διαφορετικού μεγέθους πόρων και γεωμετρίας, το MCM-41 (Mobile Composition of Matter No41) και το SBA-15 (Santa Barbara Amorphus No15). Οι μετρήσεις διεξήχθησαν στις παρυφές του πεδίου Υπεραγώγιμου μαγνήτη 4.7 T με γραμμική βαθμίδα μαγνητικού πεδίου 34.7 T/m στην περιοχή θερμοκρασιών 100K έως 400K με θέρμανση.

Μελετήθηκε θερμοκρασιακά η δυναμική του ιοντικού υγρού BMIM TCM που περιορίζεται στο MCM-41 και το SBA-15 ως συνάρτηση της θερμοκρασίας. Για να διερευνηθεί η επίδραση της θερμικής επεξεργασίας τα αποτελέσματα συγκρίθηκαν με τις τιμές που λήφθηκαν για το ιοντικό υγρό σε ελεύθερη μορφή και οι μετρήσεις υποδεικνύουν την ύπαρξη δύο ελαχίστων στον χρόνο εφησυχασμού T_1 η οποία οφείλεται στην εμφάνιση μεταβατικής φάσης του ιοντικού υγρού σε μια υαλώδη φάση. Πραγματοποιήθηκε πειραματικός υπολογισμός του χρόνου συσχέτισης μέσω του χρόνου εφησυχασμού T_1 και μέσω θεωρητικών μοντέλων Πυρηνικού Μαγνητικού Συντονισμού της θεωρίας BPP (Bloembergen-Purcell-Pound theory-BPP theory) εντοπίστηκαν πειραματικά 2 ελάχιστα που υποδηλώνουν μετάβαση φάσης του ιοντικού υγρού.

ΛΕΞΕΙΣ ΚΛΕΙΔΙΑ: Πυρηνικός Μαγνητικός Συντονισμός, Νανοσωλήνες Άνθρακα, Ιοντικά Υγρά

ABSTRACT

In this dissertation we considered self-diffusion coefficient (D) and relaxation measurements by nuclear magnetic resonance (NMR) methods. The measurements were carried out in two categories: water confined in different types of carbon nanotubes as well as an ionic liquid in bulk form and confined into two mesoporous structures.

Carbon Nanotubes (CNTs) have attracted considerable interest by researcher community the recent years, because of their numerous applications in a wide range of fields ranging from medicine and pharmaceuticals to energy, environment, electronics and telecommunications to industry and aerospace. In addition, their symmetrical shape and high mechanical, chemical and thermal stability ensure well-defined transport properties and make CNTs ideal prototype systems for studying transport phenomena in confined geometries in nanoscale. Consequently, the study of diffusion of water inside carbon nanotubes is extremely useful in attempts to understand the flow of water through hydrophobic nanostructures to exploit CNTs as building blocks in a new generation of technology devices. Several studies, mostly theoretical , have been conducted so far in order to investigate the interaction between water and the surface of CNTs. However, experimental studies are still scarce and have limited potential, resulting in controversial results.

In recent years, the interest of the scientific community has focused on the particular behavior of the flow of water through hydrophobic CNTs. Recent theoretical and experimental studies have shown that water molecules when confined to Nanoporous materials of dimensions comparable to their size, exhibit peculiar behavior, such as one of the main characteristic is the exceptionally high water flow. The peculiar fast flow inside the nanotubes is imprinted on the values of the self-diffusion coefficient D of the protons of water, and it is found to be greater than the diffusion coefficient D of free water for the molecules moving along the axis at the center of the tubes. This phenomenon has a particularly significance impact on many CNTs applications, from targeted drug delivery systems to new generation membranes, which require the supply of liquid through the interior of carbon nanotubes.

Nuclear Magnetic Resonance is considered to be one of the most important non-invasive techniques to study the behavior of fluids when confined into mesoporous and nanoporous solid materials. It is based on the interaction of nuclear spins with an external magnetic field,

as well as on the interaction of nuclear spins with neighboring nuclear and unconjugated electron spins. This makes the technique it extremely sensitive to the local atomic environment, allowing the study of atomic and molecular dynamics in time ranges ranging from nanosecond to hours or even weeks or months.

The application of one dimension conventional Nuclear Magnetic Resonance (1D-NMR) techniques to study the molecular dynamics of fluids involves the observation and recording of the spectral line, the relaxation time T_1 (spin-lattice) and T_2 (spin-spin) along with the self-diffusion coefficient D of the under investigation nuclei. Significant information on the dynamics and the interactions both at atomic level and at the local environment as well as for the translational motions of the molecules. Thus, from experimental ^{1}H 1D-NMR studies of protons (^{1}H) in water molecules, we retrieve information on possible water diffusion mechanisms inside CNTs. Therefore, 1D-NMR techniques cannot distinguish the potential different contributions to molecular diffusion or in the relaxation mechanisms nor distinguish the possible correlations between the discrete contributions.

In this dissertation experimental measurements were made for the first time and it became possible to distinguish different diffusion coefficient components in the water flow inside the nanotubes by applying a pioneering method that combines two dimensional techniques (D-T_2 και T_1 -T_2) of 2D Magnetic Resonance Spectroscopy with an modified version of advanced Tikhonov Inversion algorithms. In the experimental data analysis, advanced two-dimensional inversion algorithms were used to determine the distribution of the self-diffusion coefficient D of water in order to correlate them with the distributions in the relaxation times T_1 and T_2.

Initially, water diffusion into single and double wall CNTs (SWCNT and DWCNT) was studied. This method allowed us to investigate experimentally the diffusion of water at the nanoscale and to distinguish different groups of molecules through temperature studies from 265K up to 300K with different dynamics-kinematic behavior. It was observed that when water flows through CNTs the local environment is not the same for all the fluid water molecules. In each case, the relaxation and diffusion mechanisms are determined by the local environment and the interactions of the molecules, resulting in each group of water molecules giving a separate NMR signal with a different self-diffusion coefficient. A distribution on the values of relaxation times and diffusion coefficient values was observed which reflects into the distribution of water molecules in different dynamic environments close to the walls and close to the axis of the nanotube.

By the method developed in this dissertation it was possible to observe experimentally for the first time different water groups on the walls and along the axis of the nanotubes and to confirm the predictions of the theoretical models (MD Molecular Dynamics) that exist in the literature. The experimental NMR method developed is advantageous than MD simulations because the time scale of the NMR diffusion experiments was 2-3 orders of magnitude larger than the MD scale. This allowed us to be able to observe very slow movements of the studied molecules in order to study the peculiar diffusion of water inside CNTs. By applying 2D D-T_2 and T_1-T_2 ^1H NMR techniques to study water inside SWCNT and DWCNT nanotubes, a multilayer structure was observed in the diffusion of water in DWCNTs and the presence of a "fast" diffusion component resulting on a fast diffusion of water molecules along the central axis of the nanotube.

In the second stage of the present study, experimental measurements were conducted using the same methodology on carbon nanotubes with different values of internal diameter ranging from 1.1 nm to 6 nm in the temperature range from 265K up to 300K in order to disentangle the effect of the diameter on the water diffusion mechanism. It was experimentally identified the optimum diameter between 3.0nm-4.5nm which we observed an enhancement on the flow of water molecules inside the CNTs.

In addition, the results indicate that in these diameters the water inside CNTs is further analyzed in two diffusion components with the central longitudinal axis component of the nanotube exhibiting surprising fast transport properties as mentioned earlier, with D values ranging from two to almost four times higher than the D values of free water.

In the final stage of the present study, the behavior of an ionic liquid in bulk form as well as confined in two mesoporous structures was studied in a wide range of temperatures.

Ionic Liquids (ILs) are a novel class of materials which are salts having a melting points less than 100 °C and they consist by organic cations, which are bulky and with low symmetry, while their anions may be inorganic or organic. These salts are usually met as liquids at room temperature, so they are referred to as Room Temperature Ionic Liquids (RTILs). Their interesting physicochemical properties, the different ways in which they are involved (as solvents) in reactions and the significant ability to capture certain gases, such as CO_2, have attracted a particularly strong the interest of the research community. Ionic liquids (ILs) are superior compared to conventional solvents in the capture of CO_2 and have an environmental friendly behavior as they are characterized by negligible vapor pressure and volatility. Supported Ionic Liquid Phase Systems (ionic liquids confined in mesoporous structures) have multiple applications such as gas capture and separation processes, catalysis

processes, lubricants, nanocomposite materials, capacitors, fuels, etc. The performance of all these processes depends mainly on the ionic transfer of ionic liquids at nanoscale. Nuclear Magnetic Resonance (NMR) spectroscopy has been shown to be a very important non-invasive tool for investigating the dynamics and properties of ILs. In particular, NMR experiments in the fringe field of a superconducting magnet which ranges linearly allows us for the direct calculation of the self-diffusion coefficient D.

^{1}H NMR temperature studies were performed with conventional one-dimensional and two-dimensional Nuclear Magnetic Resonance spectroscopy techniques as well as measurements of T_1 (spin-lattice) and T_2 (spin-spin) and D self-diffusion coefficients of BMIM TCM ionic liquid in bulk form as well as confined into two mesoporous silica structures of different pore size and geometry, MCM-41 (Mobile Composition of Matter No41) and SBA-15 (Santa Barbara Amorphus No15). The measurements were conducted in the fringe field of the superconducting magnet 4.7T with a gradient varying linearly of the value of 34.7 T/m in the temperature range 100K to 400K while heating.

The reorientational dynamics of the BMIM TCM ionic liquid limited to MCM-41 and SBA-15 as a function of temperature was studied in order to investigate the effect of thermal treatment and the results were compared with the values obtained for the bulk ILs and the results indicate the existence of two minima in the T_1 values due to the occurrence of a transition phase of the ionic liquid in a glassy supercooled state. Experimental calculation of correlation time was carried out through T_1 and T_2 relaxation times and by the use of theoretical models of BPP theory (Bloembergen-Purcell-Pound theory) we experimentally identified two local minima indicating a phase transition of the ionic liquid.

KEYWORDS: Nuclear Magnetic Resonance NMR, Carbon Nanotubes CNTs, Ionic Liquids ILs

Acknowledgements

There are some people I’d like to thank, for helping me in one way or another, during the last 4.5 years. First of all I would like to thank Prof. Margarita Beazi-Katsioti, Prof. Dimitrios Karonis and Dr George Papavassiliou who contributed to my scientific education and training throughout my years of study at the National and Technical University of Athens and in the National Centre for Scientific Research Demokritos. Also I would like to thank Professor Dimitrios Gournis, Professor Konstantina Kollia and Dr.George Romanos for the honor they made me to participate in the advisory committee of my thesis.

I would like to express my gratitude, first and foremost, to my advisor Dr George Papavassiliou for being a great mentor in person and in research and for the inspiration he provided me by his hardworking and passionate attitude in research.

Thanks is also extended to Dr. Michael Fardis for his scientific guidance in all aspects of research. I would also like to thank the NMR post doc group members Dr. Nikos Panopoulos and Dr. Marina Karagianni and also Dr. George Diamantopoulos for their continued support and for their collaboration and contribution during this period.

I would also like to thank the PhD Candidates and lab and office mates Athanasios Anastasiou, Savvas Orfanidis and Mohammed Subrati for making my experience in the lab the most incredible one.

My sincere thanks also goes to Dr. Marios Katsiotis who provided me with the opportunity to join the NMR team in Demokritos as a PhD Student, without him I wouldn’t have the chance to be part of this research team.

I would like to thank plenty of friends I cannot include them all here, but special thanks goes to my friend Sotiria.

Finally, I would like to thank my family especially my parents, my sister Valeria and Antonis for the endless support throughout the years. But most of all, I would like to thank Christoforos for the endless encouragement and the unbelievable support in all levels.

PUBLICATIONS

Papers in peer review journals

^{1}H NMR study of dynamics of 1-Butyl-3-methylimidazolium Tricyanmethanide Ionic Liquid under Confinement in SBA-15 and MCM-41 Mesoporous Silica

L. Gkoura, N.Panopoulos, J. Hassan, M.Karagianni, M. Beazi-Katsioti, D. Karonis, M. Fardis, G. Romanos and G. Papavassiliou

-To be submitted-

The Peculiar Size Dependent Ultrafast Water Diffusion in Carbon Nanotubes: A Combined 2D NMR Diffusion-Relaxation (D-T_2) and Molecular Dynamics Simulations Study

L. Gkoura, G. Diamantopoulos, D. Homouz, S. Alhassan, M. Beazi-Katsioti, A. Anastasiou, G. Romanos, M. Fardis, J. Hassan and G. Papavassiliou

The Journal of Physical Chemistry C, ACS Publications

-Accepted to be published-

^{1}H NMR Tests on Damaged and Undamaged XLPE Samples and SiR Samples

L. Gkoura, T. Wang, A. Anastasiou, N. Harid, , H. Griffiths, M. Haddad, M. Fardis and M.Karagianni

IEEE 2019 Special Issue of High Voltage on Monitoring and Diagnostics in High Voltage Engineering

-Accepted to be published-

Ultrafast Stratified Diffusion of Water inside Carbon Nanotubes. Direct Experimental Evidence With 2D D−T_2 NMR Spectroscopy

J. Hassan, G. Diamantopoulos, L. Gkoura, M. Karagianni, S. Alhassan, S.V.Kumar, M.S. Katsiotis, T. Karagiannis, M. Fardis, N. Panopoulos, H. J. Kim, M. Beazi-Katsioti and G. Papavassiliou

The Journal of Physical Chemistry C 2018 122 (19), 10600-10606 DOI: 10.1021/acs.jpcc.8b01377

Papers in International Conferences

Size Dependent Ultrafast Water Flow in Carbon Nanotubes. A Combined 2D ^{1}H NMR Diffusion-Relaxation (D-T_2) and Molecular Dynamics Simulations Study

L. Gkoura, J. Hassan, M. Beazi-Katsioti, D. Karonis, M.Fardis and G. Papavassiliou

21th Euromar-15th Ismar International Conference on Magnetic Resonance Spectroscopy 2019, Berlin, Germany, 25-30 August 2019 *(Abstract accepted)*

Magnetic Nanoparticles for Oil Reservoir Characterization

G. Papavassiliou, S. Alhassan, A. Anastasiou, M. Subrati, S. Orfanidis, L. Gkoura, M. Fardis, M. Karagianni, D. Gournis, H. J. Kim, and S. Pantelides

NanoTech Poland 2019 ,International Conference and Exhibition Poznań, Poland 5th-9th June 2019

Tracking Ferrofluids beneath Earth Surface: A Novel Electro-Magnetic Tomography Method for High Resolution Imaging of Oil Reservoirs

G. Papavassiliou, S. Alhassan, A. Anastasiou, M. Subrati, S. Orfanidis, A. Kilybay, M. Fardis, M. Karagianni, L. Gkoura, D. Gournis, S. Pantelides and H. J. Kim

8th Workshop on Current trends in Molecular and Nanoscale Magnetism, Rhodes, Greece 27-31 May 2019

Study of Water Dynamics inside Carbon Nanotubes using NMR Spectroscopy

J. Hassan, L. Gkoura and G. Papavassiliou

17th International Conference on Emerging Materials and Nanotechnology, Theme: Unearthing the Researches in Materials Science and Nanotechnology, Emerging Materials Congress 2019, Berlin, Germany, 7-8 March 2019

^{1}H NMR Tests on Damaged and Undamaged XLPE Samples

T. Wang, L. Gkoura, N. Harid, G. Papavassiliou and H. Griffiths

IEEE 2018 International Conference on High Voltage Engineering and Application, Athens, Greece, 10-13 September 2018

New Information On Water Flow Inside Carbon Nanotubes Revealed by 2D NMR Correlation Spectroscopy

J. Hassan, G. Diamantopoulos, L. Gkoura and G. Papavassiliou

Nanotech Dubai 2016 & GAMS 2016, Dubai, UAE,5-7 December 2016

Papers in Panhellenic Conferences

^{1}H NMR Studies on the Structure, Phase and dynamics of bulk and confined Ionic Liquids

L. Gkoura, G. Papavassiliou, G. Romanos, M. Karagianni, M. Fardis, D. Karonis and M. Beazi-Katsioti

Conference:12th Scientific Conference of Chemical Engineering Athens, Greece, 29-31 May 2019

Poster Session

"Development of Innovative Cement Materials and Application in the Construction"

NTUA: M. Beazi-Katsioti,P Tsakiris, N. Katsiotis ,D. Velissariou, L. Karavokiros, M. Apostolis, A. Tsiolis, V. Skvelvaniti

NCSR Demokritos: , L. Gkoura ,G. Papavassiliou, P.Chatzifotis

Poster Session at National Hellenic Research Foundation, 13 June 2016

Contents

TABLE OF FIGURES 32

1. THEORY 38

1.1 Nuclear Magnetic Resonance 38
  1.1.1 Basic Principles of Nuclear Magnetic Resonance 39
  1.1.2 Classical description 40
  1.1.3 Quantum mechanical description 43
  1.1.4 Bloch equations 45
  1.1.5 FID- Spin Echo 47
  1.1.6 T_2 Relaxation and Carr-Purcell-Meiboom-Gill pulse sequence 51
  1.1.7 T_1 Relaxation and Saturation / Inversion Recovery pulse sequences 52
  1.1.8 BPP Theory 53
  1.1.9 Liquid Fragility 56
  1.1.10 Introduction to MAS NMR 61

1.2 Diffusion 63
  1.2.1 Random walk and Brownian motion 63
  1.2.2 NMR and Diffusion in a Field Gradient 66
  1.2.3 NMR and Diffusion in Porous Media 68

1.3 2D D-T_2 and T_1-T_2 Correlation NMR techniques 69

1.4 Tikhonov Regularization algorithm 70

2. EXPERIMENTS 74

2.1 Experimental Apparatus 74

2.2 Setting up a solid-state NMR experiment 79

3. CARBON NANOTUBES CNTS 80

3.1 Single Wall Carbon Nanotubes (SWCNTs) Double Wall Carbon Nanotubes (DWCNTs) and Multi Wall Carbon Nanotubes (MWCNTs) 82
  3.1.1 Materials 82

3.2 Unveiling the ultrafast stratified diffusion of water inside carbon nanotubes; direct experimental evidence with 2D D-T_2 NMR spectroscopy 85

3.2.1 Preparation of the samples for NMR measurements 85

3.2.2 ^{1}H NMR T_1, T_2 and T_1 -T_2 relaxation analysis of water in CNTs 87

3.2.3 MAS NMR T_1 relaxation analysis of water in CNTs 93

3.2.4 2D ^{1}H D - T_2 relaxation analysis of water in CNTs 95

3.2.5 T_2 Projection of D-T_2 contour plots 103

3.2.6 D Projections of D-T_2 contour plots 105

3.2.7 Conclusions 113

3.3 The Peculiar Size Dependent Ultrafast Water Diffusion in Carbon Nanotubes: A Combined 2D NMR Diffusion-Relaxation (D-T_2) and Molecular Dynamics Simulations Study 114

3.3.1 Molecular Dynamics Simulations 116

3.3.2 NMR Experiments 118

3.3.3 Conclusions 131

4. IONIC LIQUIDS 132

4.1 Introduction 132

4.2 Studies of the Reorientational dynamics derived from temperature dependent NMR diffusion and relaxation data of Ionic Liquid and supported in two Mesoporous materials 133

4.2.1 Materials 134

4.2.2 T_1 , T_2 and D Diffusion and Relaxation Measurements 138

4.2.3 Relaxation times T_1 T_2 143

4.2.4 Self-Diffusion Coefficient and correlation with viscosity 151

4.3 Conclusions 156

5. GENERAL CONCLUSIONS AND FUTURE WORK 158

6. REFERENCES 160

Table of Figures

Figure 1. The classical model of the formation of net nuclear magnetization in a sample. In the absence of a magnetic field, the individual nuclear magnetic moments (represented by the vector arrows) have random orientation so that there is no net magnetization. In the presence of an applied magnetic field the nuclear magnetic moments are aligned preferentially with the applied field, except that thermal effects cause a distribution of orientations rather than perfect alignment. Nevertheless, there is a net nuclear magnetization [8] 40

Figure 2. Precession under Larmor frequency in a static magnetic field. The large arrow indicates the external magnetic field, the small arrow the spin angular momentum of the particle 42

Figure 3. Component of angular momentum along the magnetic field direction for an s orbital (with spin quantum number s = 1/2). The radius of the circle is $3/2h$ The energy levels for a spin- 1/2 nucleus in an applied magnetic field B_0. The levels are labelled according to their magnetic quantum number, *m* 45

Figure 4. Evolution of the nuclear spin magnetization in the laboratory frame in a longitudinal field B_0 and a transverse rotating field B_1 46

Figure 5. The induction of an NMR signal and the Free Induction Decay FID [13] 48

Figure 6. Longitudinal and transverse relaxation.. 49

Figure 7. Spin-echo pulse sequence: the magnetization is tipped by a 90 pulse and the spins start to phase out on the xy plane forming a FID signal. A second pulse flipped the spins 180 and they regroup then dephase again forming the spin echo signal 50

Figure 8. Hahn -echo pulse sequence 50

Figure 9. CPMG pulse sequence.. 51

Figure 10. The spin-lattice relaxation time T_1 with a saturation recovery technique (a) a $\pi/2$ pulse is followed by a variable delay time which allows the growth of longitudinal magnetization M_z as it increases. The $\pi/2-\pi$ spin-echo sequence "inspects" the recovery of this magnetization which is reflected in (b) where the constant of the exponential growth is T_1.. 52

Figure 11. Spectral density function vs $\omega\tau_c$[15] 54

Figure 12. Dependence of Relaxation times T_1 and T_2 vs Correlation time τ_c according to the simplified theory in which all interactions are assumed to have the same correlation time [3]..................... 55

Figure 13. Molecules of a liquid (a) translation mobility and (b) rotational mobility [8]....................... 57

Figure 14. In an anisotropic liquid, the molecular mobilities depend on the direction in space [8] 57

Figure 15. Arrhenius plot.. 58

Figure 16. Liquid viscosity as a function of scaled temperature (T_g/T), illustrating Angell's strong fragile classification. The viscosities of strong liquids have a nearly temperature-independent activation energy, while the effective activation energy for fragile (less strong) liquids dramatically increases with temperature on approaching the glass transition temperature, T_g. 60

Figure 17. Representation of a magic-angle spinning experiment. The sample is spun rapidly in a cylindrical rotor about a spinning axis oriented at the magic angle (b = 54.74°) with respect to the applied magnetic field B_0. [9] 61
Figure 18. Self-Diffusion coefficient Vs Diffusion coefficient under equilibrium and non-equilibrium conditions respectively [23] 64
Figure 19. Spatial distribution of particles due to self-diffusion. The initial position is z-z_0=0 and for self-diffusion coefficient of water at 298K. [23] 65
Figure 20. RF Frequency vs z axis and slice selection 66
Figure 21. Larmor frequency in magnetic field gradient 67
Figure 22. D-T2 Pulse Sequence 69
Figure 23. The key stages in the inversion of 2D relaxation or diffusion data [29] 71
Figure 24. Graphical Representation of the transformation of data matrix G into vector g and then the optimization problem expressed in vector matrix notation (gray scale denotes black-maximum signal, white-zero signal) [29] 72
Figure 25. The compressed optimization problem and the reshape of the solution f into a matrix [29] 73
Figure 26. NMR Laboratory of INN at NCSR Demokritos 74
Figure 27 NMR Spectrometer at INN 75
Figure 28. RF Generator 76
Figure 29. NI PXI-1031 76
Figure 30. Home build NMR probe head able to conduct measurements in 100MHz 77
Figure 31 NMR Probe 78
Figure 32. Schematic presentation of the fringe field of a Superconducting magnet 79
Figure 33. Diagram of B vs z of the magnetic field. The field gradient is constant and linear for a certain area of z 79
Figure 34. Rolling up a carbon nanotube 80
Figure 35. Multiple layers of CNTs 81
Figure 36. Chiral Vector of CNTs 81
Figure 37. TEM images for the SWCNT (left) of outer/inner diameter of ~ 2/1.2 nm and DWCNT (right) of diameter of ~5/3.5 nm 83
Figure 38. Representative TEM images of the MWCNT samples. The inner diameter of CNTs is indicated within each image 84
Figure 39. Preparation of the samples for NMR measurements 85
Figure 40. Diffusion profile of water in SWCNTs and DWCNTs at room temperatures at different water content. For better visualization the spectra are rescaled accordingly. Upon the lowering water content, the profile moves toward higher values of D, in agreement with MD simulation results [37] 86
Figure 41. ^{1}H NMR CPMG spin echo decay of water in DWCNT, at room temperature, in a magnetic field 9.4 T (400 MHz). The yellow line is the theoretical fit by applying the 1D Tikhonov regularization inversion 87

Figure 42. The graph shows the relevant ^{1}H T_2 distribution (gray circles), ^{1}H T_1 distribution (cyan circles) as well as T_2 distribution obtained from 2D D-T_2 (green circles) 88

Figure 43. The T_1-T_2 NMR pulse sequence used in the experiments 89

Figure 44. The CPMG spin-echo decay for three different t_D time 89

Figure 45. Contour plot of the static (no MAS) ^{1}H NMR T_1−T_2 spectrum of water in DWCNTs obtained with the help of a 2D Tikhonov inversion algorithm in 3.5 nm DWCNTs sample, at room temperature. On the basis of the T_2/T_1 ratios, three different water groups; bulk, interstitial and nanotube are resolved 91

Figure 46. The Inversion Recovery curve as obtained by recording the signal intensity of the first spin-echo 92

Figure 47. T_1 distribution by implementing 1D Tikhonov inversion algorithm on the relaxation data presented in Figure 46 92

Figure 48. ^{1}H MAS NMR T_1 analysis of water in DWCNTs, at room temperature. The right panel shows the relevant ^{1}H MAS NMR spectrum at spinning frequency of 12 kHz. Peak 1 corresponds to bulk water and the broad peak 2 to nanotube/interstitial water. The main panel shows ^{1}H MAS NMR relaxation data from the shaded areas of the spectrum (saturation recovery curves). The solid lines are theoretical fits by using an 1D inversion algorithm. 93

Figure 49. T_1 distributions of bulk and confined water, respectively, obtained by the inversion.......... 94

Figure 50. Upper panel: 2D D - T2 NMR pulse sequence used for the measurements 95

Figure 51. CPMG spin-echo decay of water in saturated SWCNTs, at room temperature, acquired at three different t_D values 96

Figure 52. The signal intensity of the first spin-echo versus t_D and the solid line is the fit-line using Eq.1 97

Figure 53. Decay of the first spin echo in the CPMG echo train of the external water (white circles) and the nanotube water (yellow circles) in DWCNTs as a function of t_D at RT. The blue and black lines in the inset are the theoretical curves acquired using Eq.53 for isotropic 3D and Eq.56 for restricted 1D diffusion, respectively 99

Figure 54. Self-diffusion coefficient D distribution simulations acquired by implementing a 1D Tikhonov regularization algorithm on the theoretical ^{1}H NMR Spin Echo decays of 100

Figure 55. Contour plots of 1H NMR D−T_2 spectra of water in SWCNT (left panel) and DWCNT (right panel) at selected temperatures. Two main components are seen at each temperature, corresponding to nanotube water confined in the CNTs (low T_2 values) and interlayer and bulk water external to the CNTs (high T_2 values). Plots at the left side of the contour plots are the relevant D projections... 102

Figure 56. Water T_2 projections obtained from 2D D-T_2 contour plots in (a) SWCNTs and (b) DWCNTs. For clarity, the projections have been normalized. Fits (dashed lines) were performed with inversion of a stretched exponential spin echo decay and a log-norm distribution of T_2. The short and long T_2 components correspond to the nanotube and the interstitial water 103

Figure 57. Temperature dependence of water-T_2 inside a) SWCNT and b) DWCNT samples. The green and cyan data-points are nanotube and interstitial water T_2 components, respectively............. 104

Figure 58. D projections of nanotube water in (a) SWCNTs and (b) DWCNTs. The insets show the selected areas of projection. For better visualization spectra are normalized to one. The red line at 275 K in SWCNT is the simulation curve of water diffusion in a bundle of randomly oriented CNTs. The dark cyan line is the relevant simulation curve of unrestricted bulk water diffusion. In DWCNTs, nanotube water shows stratified fast diffusion. The red line corresponds to shell water as in SWCNTs, whereas the cyan line represents the axial fast nanotube water component. 105

Figure 59. Comparison of the self-diffusion coefficient D distribution of water in (i) fully hydrated DWCNTs at 285K (black line in the upper panel) and (ii) partially hydrated DWCNTs at 293K (black line in the lower panel), as obtained from D-T_2 experiments with simulated data (blue lines). It is noticed that simulated data acquire similar T_2 distribution with the experimental data but only one D-value, D = 1:8 x 10^{-9} m^2/sec. 106

Figure 60. The D-projection of water in fully water hydrated DWCNTs at room temperature, as obtained from the relevant D-T_2 spectrum. The blue/red lines correspond to the individual D-projections of the external/nanotube water with the high (short) T_2 values..........107

Figure 61. ^{1}H NMR D−T_2 spectrum of DWCNTs with intermediate water content corresponding to the black line in panel. Left panel D-profile of water in SWCNTs and DWCNTs, at room temperature at different water content (Figure 40). Upper panel: T_2 projection obtained from 2D D-T_2 contour plot of DWCNTs..........109

Figure 62. Schematic presentation of water diffusion in SWCNTs (left panel) and DWCNTs (right panel). Water structure has been sketched by combining D−T_2 NMR experimental data with recent MD[59, 62] The green peaks in panels are sketches of the relevant water density. 110

Figure 63. Inverse of the experimental self-diffusion coefficient 1/D as a function of 1000/T. The blue line shows the temperature dependence of an ideal "strong" liquid following Arrhenius law. The solid black and the dashed cyan lines are theoretical fits as described in the text..........111

Figure 64. Snapshots from MD simulations of water molecules arrangements inside CNT nanotubes of different sizes (green: carbon atoms of the CNT wall, red: Oxygen atoms white: Hydrogen atoms and black shaded-circles represent different water layers). 117

Figure 65. 2D ^{1}H NMR D- T_2 contour-plots of water inside CNT of sizes 1.1nm, 3.5nm, 5.0nm and 5.5nm, at selected temperatures (270 K and 285 K). Two main T_2 peaks are observed, corresponding to two different water reservoirs (interstitial and nanotube water) – as seen in the T_2 projection for a 1.1nm sample at 285 K. Plots are rescaled accordingly to improve visualization..........118

Figure 66. T_2 distributions of water inside 5.0 nm and 6.0nm MWCNT, at three different temperatures (a) 285K (b) 275K and (c) 265K. 120

Figure 67. ^{1}H NMR Diffusion projections (solid lines) from the 2D D-T_2 spectra of the internal nanotube water in different CNT sizes, at 285 K. Diffusion projections at certain CNT sizes (3.0nm, 3.5nm and 4.5nm) are resolved into two components (dashed curves), represented by the main and the shoulder peaks 121

Figure 68. Water local density inside different CNT sizes along with their corresponding models obtained using MD simulations, at room temperature. The x-axis is the CNT inner diameter where

zero represents the center of the nanotube. Self-diffusion coefficients for the observed water layers inside CNTs were also calculated. 123
Figure 69. . Experimental 1/D vs. 1000/T of the nanotube water in CNTs of various sizes. The blue lines (in both the main figure and the inset) are theoretical 1/D vs. 1000/T curves of an ideal “strong” liquid obeying the Arrhenius law. The yellow circles and the black line are the experimental values of bulk water and the relevant power law fit. The self-diffusion data of bulk water at temperatures below 260 K were taken from ref [104] . In CNT sizes 3.0, 3.5, and 4.5 nm, two water groups are resolved with different dynamics (slow and fast) with fitting parameters T_s=218 K, γ=--3 (3.5nm, 4.5nm) and γ=-5 (3.0nm). The grey and the black dashed-lines are the power line fits of the data of the fast nanotube water group. The blue arrows are the relevant liquidus temperatures T_l. The inset is magnification of the 1/D vs. 1000/T curves of the fast water component for CNT sizes 3.0, 3.5, and 4.5 nm. 125
Figure 70. Temperature dependence of the inverse self-diffusion coefficient 1/D as a function of 1000/T of the bulk water (yellow circles).The blue line is the fit of an ideal strong liquid obeying Arrhenius law 128
Figure 71. . NMR experimental self-Diffusion coefficients of the shell nanotube water group versus CNT sizes, at different temperatures (285K, 275K, 270K and 265K). The black solid triangles are our MD simulation results, at room temperature which are similar to those previously reported [61]. The lines are guides to the eye. The inset shows the CNT diameter of maximum diffusion (diffusion peak) at each measured temperature. 129
Figure 72. Structure of Ionic Liquid used in this study BMIM TCM 134
Figure 73. 3D representation of BMIM cation 1-butyl-3-methylimidazolium $C_8H_{15}N_2$ 135
Figure 74. Tricyanomethanide C_4N_3 135
Figure 75. NMR samples of ILs and IL in SBA-15 and MCM-41 136
Figure 76. DSC thermographs of the bulk and immobilized (supported) Ionic Liquid BMIM TCM after quenching [156] 137
Figure 77. Inversion Recovery Pulse Sequence 138
Figure 78. Fitted experimental data of T1 relaxation measurements at selected temperatures 139
Figure 79. Relaxation time T_1 as a function of temperature during heating from 100K up to 400K.. 140
Figure 80. Hahn spin echo measurements for the 3 different samples 141
Figure 81. Spin-spin relaxation studies in BMIM TCM and under confinement 142
Figure 82. Inverse Diffusion coefficients versus 1000/T as obtained by NMR experiments for bulk and confined BMIM TCM (black circles) in MCM-41 (grey circles) and SBA-15 (red circles) 143
Figure 83. T_1 spin-lattice relaxation time as a function of temperature for BMIM TCM and confined in SBA-15 and MCM-41 silica porous media. The measurements were performed in the stray field of a 4.7 T Bruker superconductive magnet providing a 34.7 T/m constant magnetic field gradient at ^{1}H NMR frequency of 101.123 MHz while heating from 100K. The red and the purple curves are the theoretical fits according to the BBP model and LS model free approach. The cyan curve is the theoretical fit of the applying these two models in the specific temperature ranges. 146

Figure 84. Temperature dependence of ^{1}H NMR relaxation times T_1 and T_2 measured for BMIM TCM 147

Figure 85. Plot of correlation frequencies obtained by the use of two different models BPP theoretical fit and LS Model Free approach. 148

Figure 86. Arrhenius plot of correlation frequencies vs time 149

Figure 87. T_1 spin-lattice relaxation time as a function of temperature for BMIM TCM and confined in SBA-15 and MCM-41 silica porous media. The measurements were performed in the stray field of a 4.7 T Bruker superconductive magnet providing a 34.7 T/m constant magnetic field gradient at ^{1}H NMR frequency of 101.123 MHz. The solid black grey and red curves are the theoretical fits according to the BBP model and LS model free approach 150

Figure 88 Arrhenius plots of diffusion coefficients for D measured by ^{1}H NMR experiments for BMIM TCM and for the IL confined in SBA-15 and MCM-41. The lines denote fits by VFT equation (black line grey line and red line) for each sample. . The lines were calculated by using the best-fit parameters given in Table 1. 152

Figure 89. Diffusion coefficient plot versus $kT/\pi\eta$ for the BMIM TCM IL. Linear fits are applied for two different regions shown by the red and the blue solid lines and the calculated values of cr_s are 1.3nm and 0.86nm respectively 154

1. Theory

1.1 Nuclear Magnetic Resonance

The evolution of quantum theory in the 1920s paved the way for the discovery of Nuclear Magnetic Resonance (NMR) as the concept of spin was developed. Stern and Gerlach's eminent experiment in 1922 examined the behaviour of a beam of silver atoms passing through a magnetic field: they observed a discrete number of deflected beams, rather than a continuous range of deflection, confirming that the particles possessed an intrinsic angular momentum of certain quantized values. Uhlenbeck and Goudsmit proposed the concept of an electron spinning around its own axis in 1925, with angular momentum and a magnetic dipole moment resulting from the spinning electrical charge. Pauli had first suggested in 1924 that nuclei possess spin in his explanation for the origin of hyperfine splitting in atomic optical spectra. He went on to formulate a theoretical framework of spin angular momentum in 1927. The nuclear spin was first observed by Stern, Frisch and Estermann in 1933 after they adapted their equipment to measure the magnetic moment of the proton in a beam of hydrogen molecules. In 1938 Isidor Rabi extended the Stern Gerlach experiment and he managed to measure nuclear spin in lithium isotopes and protons[1, 2].

The first observations of the NMR phenomenon were made in December of 1945 when Purcell, Torrey and Pound (Purcell group at Harvard University) detected weak radio frequency signals generated by the nuclei of the atoms in 1Kg of paraffin wax. At the same time Bloch, Hansen and Packard (Bloch group at Stanford University) they observed radio frequency signals coming from the atomic nuclei of water. In 1952, Felix Bloch and Edward M. Purcell shared the Nobel Prize in Physics for their discovery [3]. The two aforementioned experiments actually discovered that magnetic nuclei could absorb energy in the radiofrequency band when exposed to a magnetic field which was actually the birth of the Nuclear magnetic Resonance. Since then NMR has become an incredible noninvasive tool to investigate matter .

Nuclear magnetic resonance is, like all atomic physics phenomena, a fundamentally quantum mechanical process. Nuclear Magnetic Resonance (NMR) is a powerful spectroscopic technique frequently used in Physics, Chemistry, Geology, Medicine , Archaeology and Biology for the study of matter. In principle, it is possible to perform NMR experiments on every nucleus with nuclear spin I not equal to zero.

The NMR phenomenon relies basically on the interaction of the magnetic dipolar moment of the nucleus with the magnetic field and of the electric quadrupole moment with the electric field gradient. The information obtained from the experiments gives us information about the local magnetic, electrical and structural properties of the system under investigation and microscopic build up and phase transitions.

In this NMR theory section we are going to present the NMR basics and introduce shortly the used methods and expected effects. For deeper consideration for NMR spectroscopy we cite the NMR books of A. Abragam Ref. [4], C.P. Slichter Ref. [5], P.Callaghan [6] and E. Fukushima [7].

1.1.1 Basic Principles of Nuclear Magnetic Resonance

Matter is made of atoms which are made of electrons and nuclei. Each atomic nucleus has four important physical properties: mass, electric charge, magnetism and spin. Many atomic nuclei possess angular momentum or spin. NMR is a quantum mechanical phenomenon of nuclear spin.

It is well known from Nuclear Physics the atomic nucleus consists of neutrons and protons. Neutrons and protons are known collectively as nucleons. An atomic nucleus is specified by three numbers: the atomic number, the mass number, and the spin quantum number.

The atomic number Z specifies the number of protons inside the nucleus. The electric charge of the nucleus is Ze. The electric charge of the nucleus determines the chemical properties of the atom of which the nucleus is a part. The mass number specifies the number of nucleons in the nucleus, i.e. the total number of protons and neutrons. Nuclei with the same atomic number but different mass numbers are called isotopes. NMR is mainly concerned with stable isotopes. Stable nuclei are usually formed from approximately equal numbers of protons and neutrons.[8]

1.1.2 Classical description

Proton and neutron have magnetic moments ($2.79\mu_n$ and $-1.91\mu_n$ respectively where $\mu_n=eh/2m_p$) [4, 6]. As a result all atomic nuclei with odd atomic number, odd mass number or with both these odd number, exhibit a nonzero total angular momentum J and a non-zero magnetic moment μ.

When a nuclei is inserted in a static uniform magnetic field the net magnetization which is equivalent to a bulk magnetic moment arising from the nuclei in a sample is M and it is the vectorial sum of all individual magnetic moments associated with all the nuclei as seen in Figure 1.

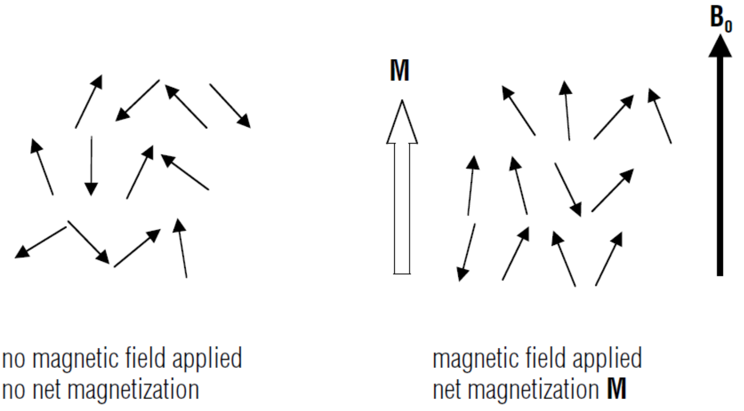

Figure 1. The classical model of the formation of net nuclear magnetization in a sample. In the absence of a magnetic field, the individual nuclear magnetic moments (represented by the vector arrows) have random orientation so that there is no net magnetization. In the presence of an applied magnetic field the nuclear magnetic moments are aligned preferentially with the applied field, except that thermal effects cause a distribution of orientations rather than perfect alignment. Nevertheless, there is a net nuclear magnetization [8]

The sum of all magnetic moments μ_i will be the net magnetization M as follows:

$$\mathbf{M} = \sum_i \boldsymbol{\mu}_i \tag{1}$$

where μ_i is the magnetic moment associated with the ith nucleus. Each nuclear magnetic moment is related to the nuclear spin I_i of the nucleus by

$$\boldsymbol{\mu_i} = \boldsymbol{\gamma I_i} \qquad \textbf{(2)}$$

g is the magnetogyric ratio, a constant for a given type of nucleus. So we can write the net magnetization of the sample as

$$\mathbf{M} = \boldsymbol{\gamma}\mathbf{J} \qquad \textbf{(3)}$$

where J is the net spin angular momentum of the sample giving rise to the magnetization M. If the nuclei are placed in a uniform magnetic field B as in the NMR experiment, a torque T is exerted on the magnetization vector:

$$\mathbf{T} = \frac{\mathbf{d}}{\mathbf{dt}}\mathbf{J} \qquad \textbf{(4)}$$

The torque in this situation is given by

$$\mathbf{T} = \mathbf{M} \times \mathbf{B} \qquad \textbf{(5)}$$

Combining equation 3 and 5 we derive:

$$\frac{\mathbf{dM}}{\mathbf{dt}} = \boldsymbol{\gamma}\, \mathbf{M} \times \mathbf{B} \qquad \textbf{(6)}$$

which describes the motion of the magnetization vector M in the static magnetic field B. It is shown that M precesses about a fixed B at a constant rate $\omega=\gamma B$. This is called in the NMR Larmor frequency and is characteristic of the nuclei involved, and proportional to the strength of the external magnetic field. Actually it is the frequency with which the magnetization precesses about the magnetic field B_0 and it is common as ω_0 [9, 10]

$$\boldsymbol{\omega_0} = \boldsymbol{\gamma}\, \mathbf{B_0} \qquad \textbf{(7)}$$

Where γ is a scalar called the gyromagnetic ratio. Each nucleus has a specific gyromagnetic ratio, proton or ^{1}H, for instance, has γ = 42.5774 MHz/T and ^{2}H has γ =6.53896MHz/T

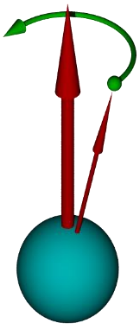

Figure 2. Precession under Larmor frequency in a static magnetic field. The large arrow indicates the external magnetic field, the small arrow the spin angular momentum of the particle

The above transition occurs at a constant angle to the axis of the constant magnetic field resulting in the magnetic moment to describe a circular path around B0. The fact this means that the magnetic moment is characterized by a given projection at axis of the field and the speed at which the magnetic moments precess around the external magnetic field is called precessional frequency.

1.1.3 Quantum mechanical description

As described before when a magnetic moment μ interacts with an applied magnetic field B_0 an interaction commonly called the Zeeman interaction in quantum mechanics. Classically, the energy of this system varies, with the cosine of the angle between μ and B_0, with the lowest energy when they are aligned. In quantum theory, the Zeeman appears in the Hamiltonian operator H as follows:

$$\boldsymbol{\hat{H} = -\hat{\mu}\, B_0} \qquad \textbf{(8)}$$

Where $\hat{\mu}$ is the nuclear magnetic moment operator and B_0 is the magnetic field applied. This Hamiltonian is often referred as Zeeman Hamiltonian and if we substitute the μ in terms of the nuclear spin operator I it will be [4-6]

$$\mathbf{\hat{H} = -\boldsymbol{\gamma}\, h\, \hat{I}\, B_0} \qquad \textbf{where } \mathbf{\hat{\mu} = \boldsymbol{\gamma}\, h\, \hat{I}} \qquad \textbf{(9)}$$

Considering that the magnetic field is applied in the z direction the eigenvalues of this Hamiltonian are simple multiples of ($\gamma h H_0$) of the eigenvalues of I_z.

The eigenfunctions $\hat{H}$ of are the wavefunctions describing the possible states of the spin system in the B_0 field. Since $\hat{H}$ is proportional to the operator I_z in this case, the eigenfunctions $\hat{H}$ of are the eigenfunctions of I_z, which are simply written as |I,m> in bra-ket notation, or alternatively as Ψ_m, where I is the nuclear spin quantum number. The quantum number m can take 2I + 1 values: I, I - 1, I - 2, . . . , -I. The eigenvalues of $\hat{H}$ are the energies associated with the different possible states of the spin. The eigenvalues are obtained by operating with $\hat{H}$ on the spin wavefunctions:

$$\mathbf{\hat{H}}\left|\boldsymbol{I,m}\right. > = \boldsymbol{E_{I,m}}\left|\boldsymbol{I,m}\right. > \qquad (10)$$

Where El,m is the energy of the eigenstate |I,m>.By substitution in equation 9

$$\hat{\mathrm{H}}\left|\boldsymbol{I},\boldsymbol{m}\right.>= -(\boldsymbol{\gamma h B_0 I_z}\left|\boldsymbol{I},\boldsymbol{m}\right. \geq -(\boldsymbol{\gamma h B_0})\boldsymbol{m}|\boldsymbol{I},\boldsymbol{m}> \qquad \textbf{(11)}$$

Since |I,m> is an eigenfunction of Îz, with an eigenvalue m,

$$\hat{\boldsymbol{I}}_z|\boldsymbol{I},\boldsymbol{m} = \boldsymbol{m}|\boldsymbol{I},\boldsymbol{m}> \qquad \textbf{(12)}$$

The allowed energies o the eigenstates are obtain and there are

$$\mathbf{E = -\boldsymbol{\gamma}\,h\,B_0 m \qquad where\;\; m = I, I-1, \ldots, -I} \qquad \textbf{(13)}$$

There are thus 2I+1 energy levels each of which may be thought of as arising from an orientation of μ with respect to B_0 such as its projection on B_0 is quantitized. Equation 9 shows that the energy separation between the states is linearly dependent on the magnetic field strength. For the particularly important case of I=1/2 like proton there are just two energy levels and two wave functions, m=1/2 and m=-1/2.

For a spin with I = 1/2 , m = ±1/2 so there are two possible eigenstates with energies E1/2, ±1/2=-+1/2 γhB_0. These states are frequently referred to as the Zeeman states. The transition energy ΔE between the spin states is γhB_0. In frequency units, this corresponds to ω_0 (= γB_0), the Larmor frequency in the vector model. The Larmor frequency in the vector model corresponds to a rotation of the net nuclear magnetization vector about B_0 and not to a transition. So in a sample of non-interacting spin 1/2 nuclei, each spin system can exist in one of two possible eigenstates. At equilibrium, there is a Boltzmann distribution of nuclear spins over these two states.

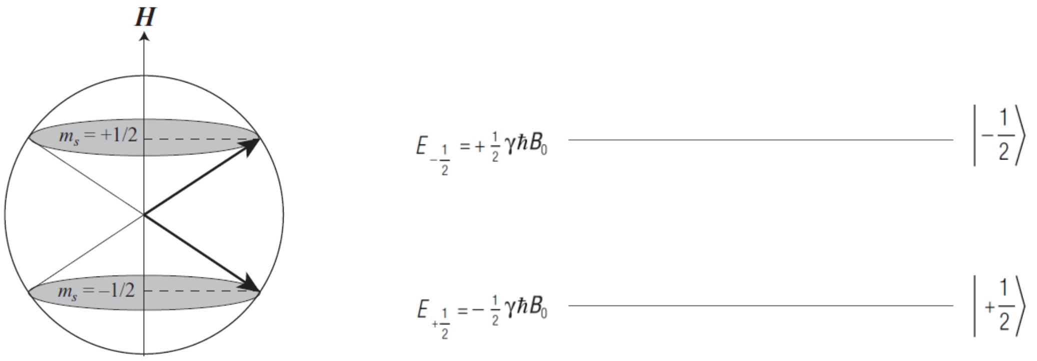
H
$m_s = +1/2$
$m_s = -1/2$
$E_{-\frac{1}{2}} = +\frac{1}{2}\gamma\hbar B_0$
$E_{+\frac{1}{2}} = -\frac{1}{2}\gamma\hbar B_0$
$\left|-\frac{1}{2}\right\rangle$
$\left|+\frac{1}{2}\right\rangle$

Figure 3. Component of angular momentum along the magnetic field direction for an s orbital (with spin quantum number s = 1/2). The radius of the circle is $\sqrt{3}/2h$ The energy levels for a spin- 1/2 nucleus in an applied magnetic field B_0. The levels are labelled according to their magnetic quantum number, *m*

Considering that for two energy levels, only one transition is possible. We will define the population numbers in thermal equilibrium N_+^0 and N_-^0 so that $n = N_+^0 - N_-^0$ will be the population difference between the levels. From Maxwell-Boltzmann-statistics we derive the population ratio

$$\frac{N_-^0}{N_+^0} = \exp\left(\frac{\Delta E}{k_B T}\right) = \exp\left[\frac{(E_- - E_+)}{k_B T}\right] \qquad \mathbf{14}$$

Where k_B is Boltzmann constant

1.1.4 Bloch equations

In case of independent spin -1/2 nuclei the motion of the ensemble of spins may be described in terms of the precession of the spin magnetization vector. In such a model the macroscopic angular momentum vector is simply M/γ where M is the magnetization and γ is the gyromagnetic ratio. Solving equation 6 to obtain the expression for the spin evolution we need to retain only the circularly polarized component of the oscillating transverse field which is rotating in the same sense as the spin precession as [11]

$$B_1(t) = B_1 cos\omega_0 t i - B_1 sin\omega_0 t j \qquad (15)$$

Where i,j,k are unit vectors along the x y and z axes respectively.

$$\frac{dM_x}{dt} = \gamma[M_y B_0 + M_z B_1 sin\omega_0 t] \tag{16}$$

$$\frac{dM_y}{dt} = \gamma[M_z B_1 cos\omega_0 t - M_x B_0] \tag{17}$$

$$\frac{dM_z}{dt} = \gamma[-M_x B_1 sin\omega_0 t - M_y B_1 cos\omega_0 t] \tag{18}$$

The solution under the initial condition M(t)=M_0k is

$$M_x = M_0 sin\omega_1 t\, sin\omega_0 t \tag{19}$$

$$M_y = M_0 sin\omega_1 t\, cos\omega_0 t \tag{20}$$

$$M_z = M_0\, cos\omega_1 t \tag{21}$$

Where $\omega_1=\gamma$ B_1. On the application of a rotating magnetic field of frequency ω_0 the magnetization simultaneously precesses about the longitudinal polarizing field B_0 at ω_0 and about the rf field B_1 at ω_1.A s can be seen in Figure 4 in the frame of reference rotating with B_1 about B_0.[6, 12]

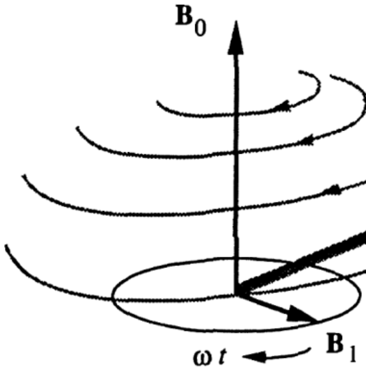

Figure 4. Evolution of the nuclear spin magnetization in the laboratory frame in a longitudinal field B_0 and a transverse rotating field B_1

After the nuclear magnetization vector is rotated by applying magnetic field B_1 for a short time, it starts to restore to its original position along the main magnetic field. M_z will grow towards M_0 with a characteristic time T_1. This process is called the longitudinal or spin-lattice relaxation. During this process energy of the spins is transferred to the environment. If B_1 is applied along the x-axis, the net magnetization in the rotating frame will rotate towards the y-axis. When B_1 is stopped when the flip angle is 90^o, we have a so called 90-pulse. After a 90-pulse the magnetization resides in the xy-plane. M_x and M_y will disappear with a characteristic time T_2. This is called the transverse or spin-spin relaxation time. This spin-spin relaxation is caused by interaction between spins and not between the spins and the environment [11].

$$\frac{dM_{x'}}{dt} = -\frac{M_{x'}}{T_2} + \gamma(M' \times B_1')_{x'} \tag{22}$$

$$\frac{dM_{y'}}{dt} = -\frac{M_{y'}}{T_2} + \gamma(M' \times B_1')_{y'} \tag{23}$$

$$\frac{dM_z}{dt} = -\frac{M_z - M_0}{T_1} + \gamma(M' \times B_1')_z \tag{24}$$

The solution of the Bloch equations for a system in which the magnetization has been placed in the x'y' plane by a 90 pulse along the x'-axis:

$$M_{x'} = 0 \tag{25}$$

$$M_{y'} = M_0 e^{-\frac{t}{T_2}} \tag{26}$$

$$M_z = M_0(1 - e^{-\frac{t}{T_1}}) \tag{27}$$

1.1.5 FID- Spin Echo

The precessing transverse magnetization is very small after an rf pulse. It is detectable, because it oscillates at a very well-defined frequency Larmor frequency. A rotating magnetic moment generates a rotating magnetic field. Through Maxwell's equations, a changing magnetic field is associated with an electric field. If a wire coil is near the sample, then the electric field sets the electrons in the wire in motion, i.e. an oscillating electric current flows in the wire.[8].

In Fourier transform nuclear magnetic resonance spectroscopy, free induction decay (FID) is the observable NMR signal generated by non-equilibrium nuclear spin magnetization precessing about the magnetic field (along z-axis). This non-equilibrium magnetization can be induced, generally by applying a pulse in the radio-frequency band close to the Larmor frequency of the nuclear spins as shown in Figure 5.

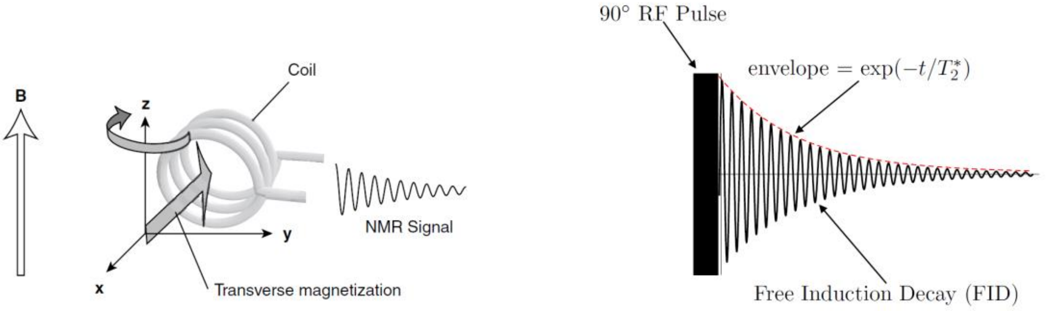

Figure 5. The induction of an NMR signal and the Free Induction Decay FID [13]

The oscillating electric current induced by the precessing nuclear transverse magnetization is called the NMR signal or free-induction decay (FID). With NMR spectroscopy we are capable to magnetize the nuclear spins with a large applied magnetic field and also to rotate the spin polarizations by using rf pulses to produce transverse nuclear magnetization and finally to detect the small oscillating electric currents induced by the precessing transverse spin magnetization [8].Because the magnetic field can never be perfectly homogeneous not all spins in the sample will be resonate in the same frequency but an extra dephasing mechanism will occur that will add up to the dephasing caused by the transverse relaxation. Fro an ensemble of spins considered this ends up to a loss of coherence and as time passes the individual spins will end up in largely different phases.This extra mechanism is called inhomogeneous broadening and we have to consider in Bloch equations a modified version of T_2 the T_2^* as [7]

$$\frac{1}{T_2^*} = \frac{1}{T_2} + \frac{\gamma}{2\pi}\Delta B \tag{28}$$

Apart from Bloch equations approach we will now discuss the pulse sequences which were used frequently in our experiments. At time $t < 0$, the sample is in its thermal equilibrium state. Then at when the 90-pulse is applied along the x'-axis, which causes the magnetization to rotate into the x'y'-plane. Because of the transverse relaxation, the magnetization in this plane will vanish with a characteristic time T_2. However, this is only true if the magnetic field B_0 is perfectly homogeneous. If some inhomogeneities are present not all spins will precess with the same frequency. There is a distribution of Larmor frequencies, which causes the spins to dephase in the x'y'-plane. This dephasing is often faster than the transverse relaxation and has a characteristic time constant T_2^*. When measuring

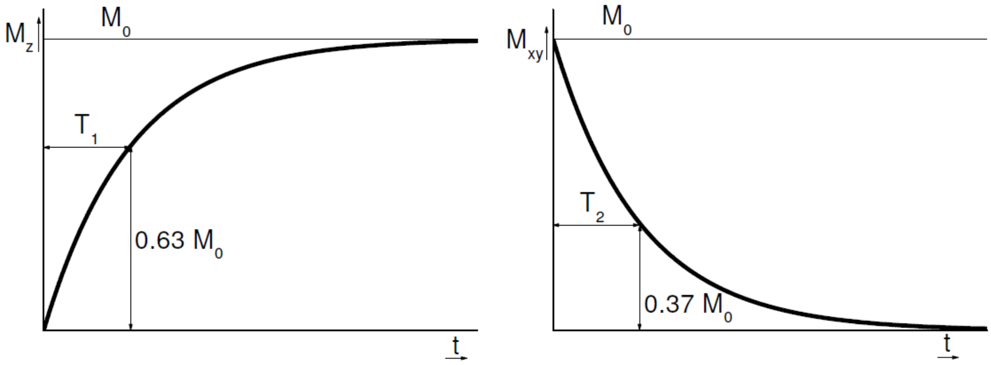

Figure 6. Longitudinal and transverse relaxation

Due to ringing of the RF coil and the recovery time of the receiver it is not often used FID. When at t=τ a 180 pulse along the x'-axis is given, the phase angle of all spins with respect to the x'-axis in the x'y'-plane is inverted. Spins that were ahead, because of a higher than average Larmor frequency, are now behind and the spins that were behind are now ahead. The faster moving spins are behind and the slower moving spins are ahead, resulting in a rephasing of the spins. At exactly t = 2τ all spins have rephased, but they immediately dephase again after t = 2τ . The signal obtained from this effect is called the spin echo, and has a maximum at t = 2τ , which is the echo time (TE) as seen in Figure 7 which is the most common pulse sequence Hahn spin-echo sequence (as seen in Figure 8 also). Due to T_2 relaxation the maximum magnetization that can be obtained by rephasing of the spins decreases exponentially in time.[4, 7]

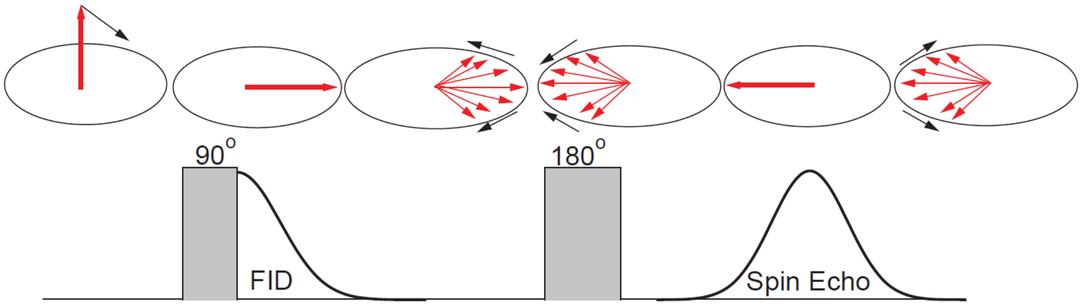

Figure 7. Spin-echo pulse sequence: the magnetization is tipped by a 90 pulse and the spins start to phase out on the xy plane forming a FID signal. A second pulse flipped the spins 180 and they regroup then dephase again forming the spin echo signal

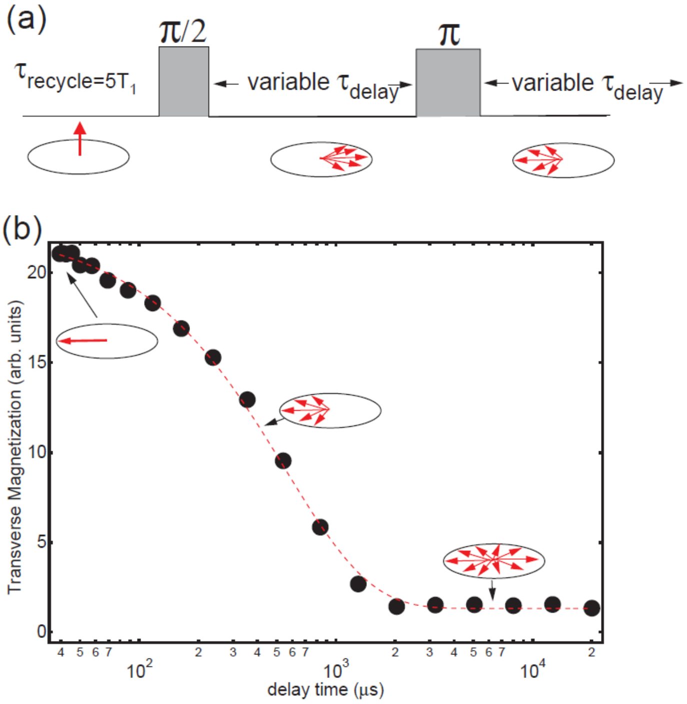

Figure 8. Hahn -echo pulse sequence

1.1.6 T_2 Relaxation and Carr-Purcell-Meiboom-Gill pulse sequence

The Carr-Purcell-Meiboom-Gill (CPMG) sequence starts identically to the Hahn spin echo pulse sequence and it is followed by a train of 180pulses. First, at t = 0 a 90pulse is applied to put the magnetization vector in the transverse plain and then at t =τ a 180 pulse is applied, causing a spin echo at t = 2τ . Instead of waiting for the longitudinal relaxation to return to equilibrium another 180pulse is given a t = 3τ. The accumulated phase of the spins that started to dephase since the first spin echo will be inverted. The spins will rephase, resulting in a spin echo at t = 4τ . The intensity of this echo will be smaller because of the T_2 relaxation as seen in Figure 9.[14]

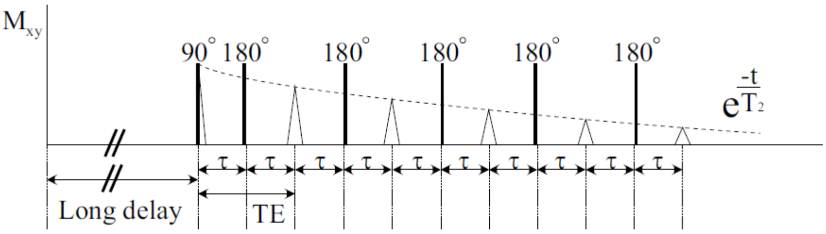

Figure 9. CPMG pulse sequence

For an ensemble of static spins, the spin-echo intensity is not influenced by magnetic field inhomogeneities, but only by the transverse relaxation mechanism. This sequence can be extended to an arbitrary number of 180 pulses, which will all give spin echoes. Most of the times numbers of 180 pulses and spin echoes are between 64 and 1024. This way of measuring T_2 is much faster than the repetitive Hahn spin echo with increasing interpulse time and as a result the duration of measuring T_2 is significantly reduced.

1.1.7 T_1 Relaxation and Saturation / Inversion Recovery pulse sequences

T_1 relaxation is the process by which the net magnetization M grows/returns to its initial maximum value M_o parallel to B_o. T_1 relaxation is referred also as longitudinal relaxation, thermal relaxation and spin-lattice relaxation. There are two popular sequences for measuring T_1. The π/2-π/2 also called 90-90 and the π-π/2 called 180-90 which are named saturation and inversion recovery pulse sequences respectively. In both sequences the first pulse prepares the spins and the second pulse measures the magnetization after the waiting period. In the inversion recovery pulse sequence the preparation pulse inverts the spin population and thus the magnetization and the recovery therefore goes from $-M_0$ to M_0 where M_0 is the thermal equilibrium magnetization attainable only after waiting for a time much longer than T_1. [7]

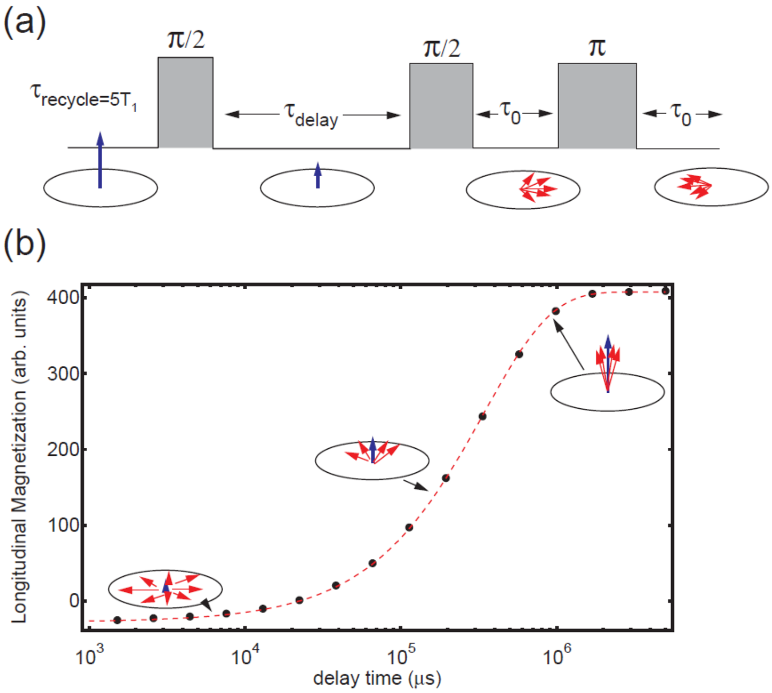

Figure 10. The spin-lattice relaxation time T_1 with a saturation recovery technique (a) a π/2 pulse is followed by a variable delay time which allows the growth of longitudinal magnetization M_z as it increases. The π/2−π spin-echo sequence "inspects" the recovery of this magnetization which is reflected in (b) where the constant of the exponential growth is T_1

For the inversion recovery pulse sequence the range of the magnetization is $2M_0$ as opposed to M_0 for the saturation recovery pulse sequence. The magnetization after a time τ is given by:

$$\frac{\mathbf{M(t)}}{\mathbf{M_0}} = \mathbf{1 - 2e^{-\frac{\tau}{T_1}}} \tag{29}$$

When for saturation recovery pulse sequence the magnetization after time τ is given by:

$$\frac{\mathbf{M(t)}}{\mathbf{M_0}} = \mathbf{1 - e^{-\frac{\tau}{T_1}}} \tag{30}$$

1.1.8 BPP Theory

Nicolas Bloembergen, Edward Mills Purcell, and Robert Pound in 1948 proposed the Bloembergen-Purcell-Pound theory known as BPP theory to explain the relaxation constant of a pure substance in correspondence with its state, taking into account the effect of tumbling motion of molecules on the local magnetic field disturbance [3]. In general liquids or gases the oscillating field can come from molecules that are in rapid, random motion, Brownian motion. Such motions are incoherent, they can be Fourier analyzed the range of frequencies , is continuous and broad and it can be described by the spectral density function Among these frequencies is the Larmor frequency which its relative contribution governs the strength of the oscillating field that can cause energy exchange and relaxation. The average length of time that a molecule remains in a position before a collision with another molecule causes it to change its state of motion in BPP theory is called correlation time τ_c [3, 15]. Y(t) is a function related to second-order spherical harmonics which describes the orientation of a molecule at time t and the after time τ is defined as Y(t+τ) . The correlation function is expressed by k(τ) which describes the extent of motion during the period τ: [3]

$$\mathbf{k(\tau) = \overline{Y(t)Y(t+\tau)}} \tag{31}$$

where the bar means that k(τ) is the average of the entire ensemble of molecules. The new position of the molecule is related to its initial position with an exponential form:

$$\mathbf{k(\tau) = k(0)e^{-\frac{\tau}{\tau_c}}} \tag{32}$$

the time constant sets the scale of time so that the spectral density J(ω) which is the fourrier transform of k(τ) is defined as:

$$J(\omega) = \int_{-\infty}^{\infty} k(\tau)e^{-i\omega t}\,dt = \int_{-\infty}^{\infty} k(0)e^{-\frac{\tau}{\tau_c}}e^{-i\omega t}dt = A\frac{\tau_c}{1+\omega^2\tau_c^2}$$

where A is the constant which we will evaluate separately for each relaxation mechanism. Different values of τ_c vs J(ω) are illustrated in … For very short or very long τ_c , J(ω) at ω_0 is relatively small and J(ω) reaches its maximum value when $\tau_c=1/\omega_0$ when the average molecular tumbling frequency is equal to the nuclear precession frequency.

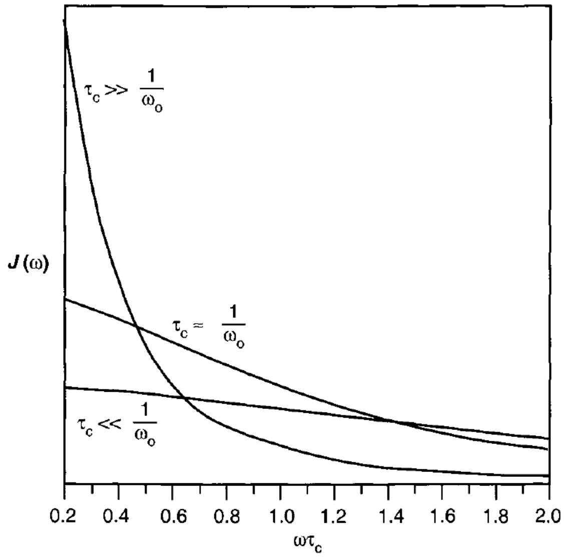

Figure 11. Spectral density function vs $\omega\tau_c$[15]

Energy transfer between the precessing nuclei and randomly tumbling molecules is most efficient when spin lattice relaxation time T_1 reaches a minimum. This description applies only for isotropic motion but in most complex systems where a number of translational and rotational times may be present. Applying the results of a single τ_c into a plot of T_1 versus τc, T_1 reaches a minimum at $\tau_c = 1/\omega_0 = 1/2\pi\nu_0$. For NMR frequencies between 1-1000MHz for various nuclei and different magnetic fields the minimum of T_1 fluctuates between $2x10^{-10}$ to $2x10^{-7}$ seconds.

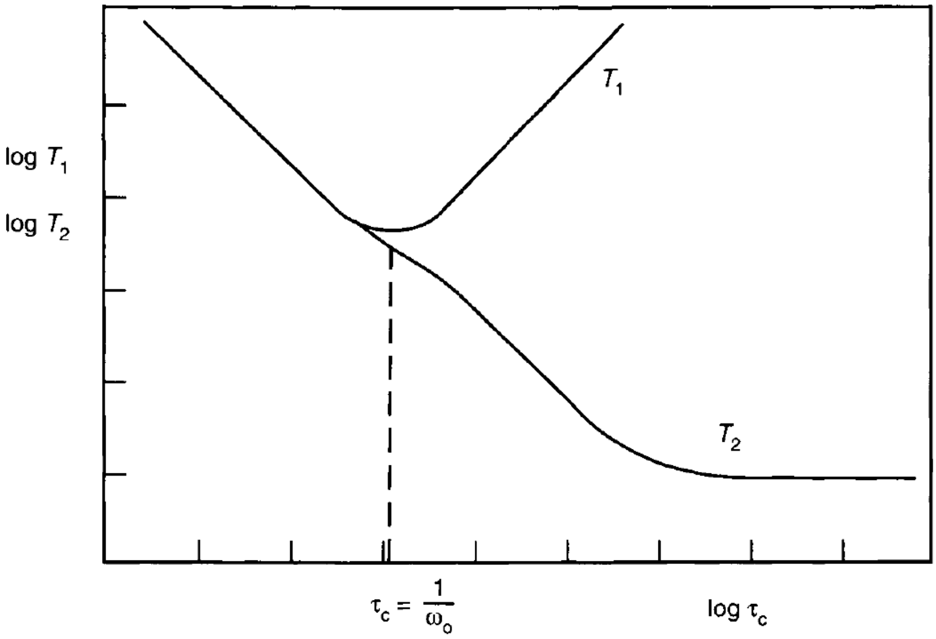

Figure 12. Dependence of Relaxation times T_1 and T_2 vs Correlation time τ_c according to the simplified theory in which all interactions are assumed to have the same correlation time [3]

T_2 as seen in Figure 12 behaves the same way as T_1 but considering that T_2 involves dephasing of precessing nuclear magnetizations rather than exchange of energy between the nuclei and the environment (spin-lattice) the dependence on the molecular motion is different from that of T_1. As a result spin-spin relaxation T_2 processes depend on high frequency (short correlation time) motions in the same way as T_1 processes, but low frequency motions and other low frequency processes, such as chemical exchange, significantly shorten T_2. So T_2 decreases monotonically as τ_c increases and it approaches a limiting value characteristic of a completely rigid solid lattice. Relaxation occurs only if there is some specific interaction between the nucleus and its environment that can result in energy exchange independent from the types of molecular motion.[3, 12, 15].

If we consider that the characteristic times of motion of the molecules can be described with the correlation time τ_c that can be considered analogue of the η/T as described above, then the T_1 and T_2 times where $T_1 > T_2$ are given for the isotropic rotational motions which interacts with bipolar interactions, from the following relationships

$$\frac{1}{T_1} = K\left(\frac{\tau_c}{1+\omega_0^2\tau_c^2} + \frac{4\tau_c}{1+4\omega_0^2\tau_c^2}\right)$$

$$\frac{1}{T_2} = \frac{K}{2}\left(3\tau_c + \frac{5\tau_c}{1+\omega_0^2\tau_c^2} + \frac{2\tau_c}{1+4\omega_0^2\tau_c^2}\right)$$

$$K = \frac{3\mu_0^2}{160\pi^2}\left(\frac{\gamma^2\boldsymbol{h}}{r^3}\right)^2 \ for\ spin - 1/2$$

where ω_0 is the Larmor frequency in correspondence with the strength of the main magnetic field , τ_c is the correlation time of the molecular tumbling motion. K is defined for spin-1/2 nuclei and is a constant with μ_0 being the magnetic permeability of free space of **h**=h/2π of the reduced Planck constant, γ the gyromagnetic ratio of nuclei and r the distance between the two nuclei carrying magnetic dipole moment.[3]

1.1.9 Liquid Fragility

In general liquids are relatively dense material phases characterized by their flow under shear forces. And in these phases there is high molecular mobility. Molecular mobility has two aspects: translation mobility and rotational mobility where translation molecular mobility is defined as the molecules or atoms who slide past each other rather freely and wander over small distances in a relatively short time. Rotational molecular mobility means that the molecules rotate around their own centers of gravity in a more or less random fashion. These types of mobility are very important for NMR, because they tend to average out many of the nuclear spin interactions, simplifying the behaviour of the nuclear spins.[8]

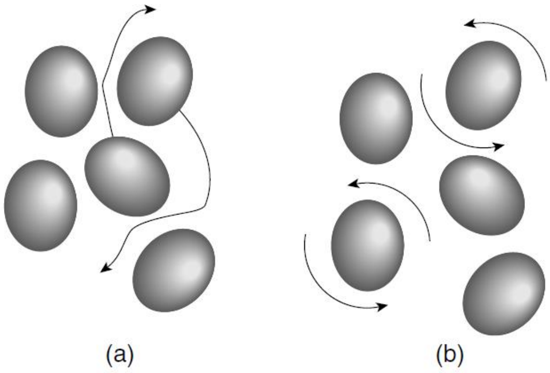

Figure 13. Molecules of a liquid (a) translation mobility and (b) rotational mobility [8]

In isotropic liquids, the mobilities are the same in all directions where in anisotropic liquids (called liquid crystals) the molecules adopt a non-isotropic special configuration. This motional anisotropy leads to incomplete averaging of the nuclear spin interactions and, hence, more complicated NMR spectra [8].

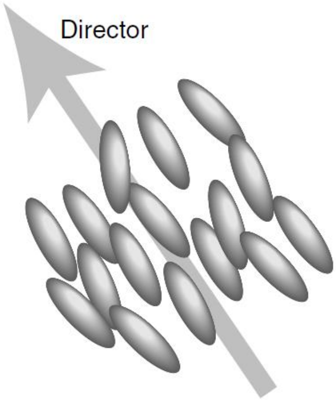

Figure 14. In an anisotropic liquid, the molecular mobilities depend on the direction in space [8]

In general the Arrhenius plot is obtained by plotting the logarithm of the rate constant, k, versus the inverse temperature, 1/T. The slope of the line is equal to the negative activation energy divided by the gas constant, R.

$$\boldsymbol{k(T) = Aexp\left(-\frac{E_a}{RT}\right)} \tag{33}$$

Where E_a, is the activation energy in the same units as RT,Type equation here. k is the rate constant, T is the absolute at temperature in Kelvins, A is the pre-exponential factor corresponding to the frequency of collisions in the correct orientation. The activation energy, E_a, is the minimum energy molecules must possess in order to react. The slope of the Arrhenius plot can be used to find the activation energy.[16]

$$\boldsymbol{lnk = lnA - \frac{E_a}{R}\frac{1}{T}} \qquad \text{or} \tag{34}$$

$$\boldsymbol{lnk = -\frac{E_a}{R}\left(\frac{1}{T}\right) + lnA} \tag{35}$$

The Arrhenius plot can also be used by extrapolating the line back to the y-intercept to obtain the pre-exponential factor, A. The pre-exponential, or frequency, factor is related to the amount of times molecules will hit in the orientation necessary to cause a reaction. The Arrhenius equation is based on the collision theory meaning that the particles must collide with proper orientation and with enough energy.[16]

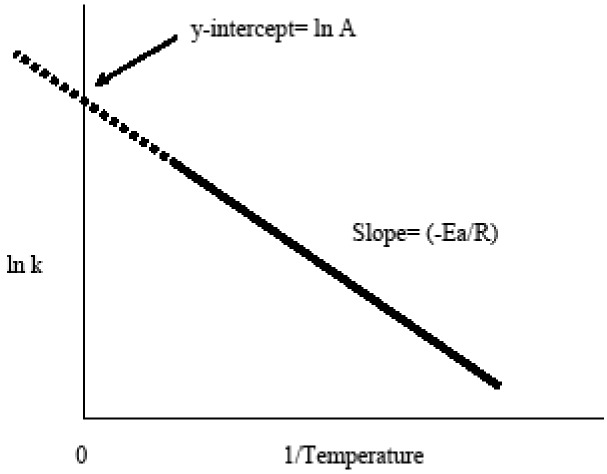

Figure 15. Arrhenius plot

Liquid fragility is a concept that has been widely used in the investigation on the glass community. The term ‘fragility’ was first coined in 1995 by Austen Angell known for his research on the physics of glasses and glass-forming liquids [17-19]. If crystallization can be avoided when a liquid is cooled, it will typically form a glass. In glass physics, fragility characterizes how rapidly the dynamics of a material slow down as it is cooled toward the glass transition. Materials with a higher fragility have a relatively narrow glass transition temperature range, while those with low fragility have a relatively broad glass transition temperature range. Physically, fragility may be related to the presence of dynamical heterogeneity in glasses, as well as to the breakdown of the usual Stokes–Einstein relationship between viscosity and diffusion.

The concept enables the comparison between the glass-forming liquids with different dynamic characters by using a general criterion, in which the temperature scale is reduced by the glass transition temperature. The classification of liquids as having different degrees of 'strong' and 'fragile' behavior has been advocated firstly by Angell at as a framework for describing relaxation in liquids. [20]

Liquid behavior during cooling is classified between strong and fragile. Strong liquids become fragile liquids on compression. In some cases, such conversions occur during cooling by a weak first-order transition. Near the glass transition temperature the viscosity increases continuously but rapidly with cooling. As the glass forms, the molecular relaxation time increases with an Arrhenius-like (simple activated) form in some liquids, but shows highly non-Arrhenius behaviour in others. The former are said to be strong liquids, and the latter fragile.

Angell’s concept of fragility, liquids with an approximately Arrhenius temperature dependence together with a physical (phonon-like) pre-exponent, are designated as strong as seen in Figure 16 [21]. As liquids show an increasing deviation from Arrhenius behaviour, they are considered to be more and more fragile. The viscosities of strong and fragile liquids are shown in Figure 16 as a function of the inverse temperature scaled to the glass transition temperature, T_g. All liquids will display some non-Arrhenius behaviour at temperatures near their glass transition, but for fragile liquids this is more dramatic [19, 21]. The representation of log viscosity vs reduced inverse temperature Tg/T is also known as the "Angell plot".

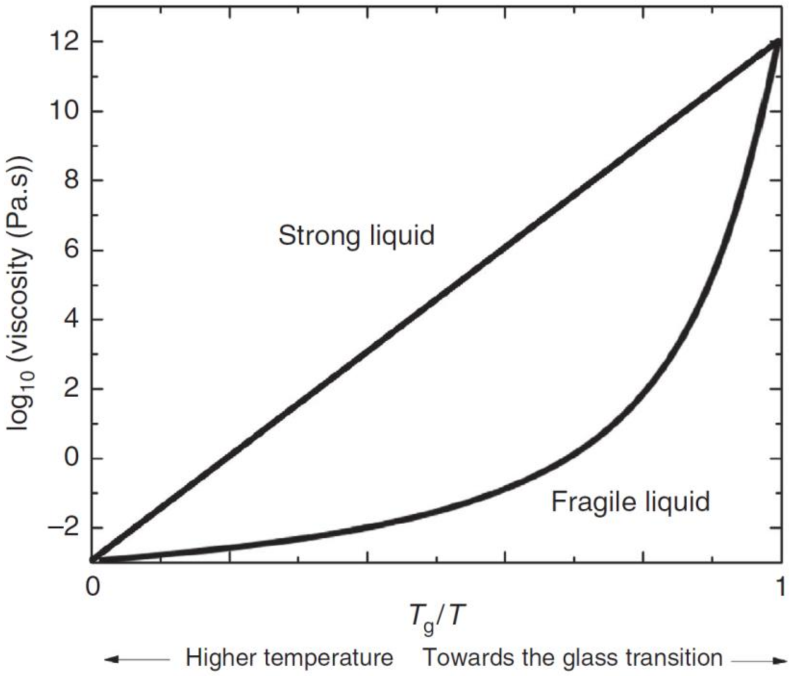

Figure 16. Liquid viscosity as a function of scaled temperature (T_g/T), illustrating Angell's strong fragile classification. The viscosities of strong liquids have a nearly temperature-independent activation energy, while the effective activation energy for fragile (less strong) liquids dramatically increases with temperature on approaching the glass transition temperature, T_g.

Liquids showing only small deviations from Arrhenius behaviour tend to exhibit only small changes of heat capacity as the liquid like degrees of freedom are lost or gained at the glass transition [18]. The degree to which the viscosity displays non-Arrhenius behavior is often parameterized by fits to the Vogel–Fulcher– Tammann (VFT) equation,

$$\boldsymbol{\eta = \eta_0 \exp(\frac{D^* T_0}{T - T_0})} \tag{36}$$

where η_0 is the viscosity in the infinite temperature limit and T_0 is the temperature at which the viscosity becomes infinite. The quantity D* is a measure of the fragility of the liquid, called the kinetic strength to differentiate it from the fragility index, which is defined near Tg. As D* increases, the behaviour of the VFT equation becomes more Arrhenius-like, consistent with a stronger (less fragile) liquid [17, 18].

1.1.10 Introduction to MAS NMR

Magic-angle spinning (MAS) is used in the vast majority of solid-state NMR experiments, and it is able to remove the effects of chemical shift anisotropy and assist in the removal of heteronuclear dipolar-coupling effects. It is also used to narrow lines from quadrupolar nuclei and is increasingly the method of choice for removing the effects of homonuclear dipolar coupling from NMR spectra. (in very high spinning speeds). [9]

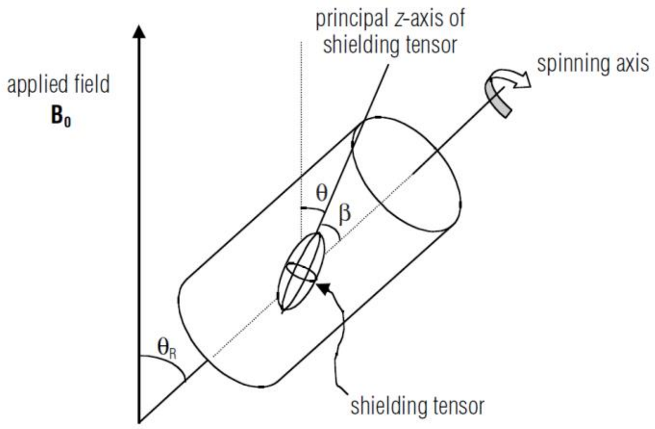

Figure 17. Representation of a magic-angle spinning experiment. The sample is spun rapidly in a cylindrical rotor about a spinning axis oriented at the magic angle (b = 54.74°) with respect to the applied magnetic field B_0. [9]

Magic-angle spinning removes the effects of chemical shielding anisotropy and heteronuclear dipolar coupling. The chemical shielding tensor is represented by an ellipsoid as seen in Figure 17, and it is fixed in the molecule to which it applies and so rotates with the sample. The angle q is the angle between B_0 and the principal z-axis of the shielding tensor; c is the angle between the z-axis of the shielding tensor principal axis frame and the spinning axis. In solution NMR spectra, effects of chemical shift anisotropy, dipolar coupling, etc., are rarely observed because the rapid tumbling of the molecules in a solution means that the angle q (or in general, q and f) describing the orientation of the shielding/dipolar tensor with respect to the applied field B_0 is rapidly averaged over all possible values. This averages the $(3\cos^2\theta-1)$ dependence of the transition frequencies to zero on the NMR timescale, i.e. rate of change of molecular orientation is fast relative to the chemical shift anisotropy, dipole–dipole coupling, etc. Magic-angle spinning achieves the same result for solids. If we spin the sample about an axis inclined at an angle θ_R to the applied field, then θ, the angle describing the orientation of the interaction tensor fixed in a molecule within the sample, varies with time as the molecule rotates with the sample. The average of (3 $\cos^2\theta$-1) in shown to be

$$< \mathbf{3cos^2\theta - 1} \geq \frac{\mathbf{1}}{\mathbf{2}}(\mathbf{3cos^2\theta_R - 1})(\mathbf{3cos^2\beta - 1}) \qquad \textbf{(37)}$$

Where the angle β is between the principal z-axis of the shielding tensor and the spinning axis θ_R is the angle between the applied field and the spinning axis θ is the angle between the principal z-axis of the interaction tensor and the applied field B_0 [9]

The angle b is obviously fixed for a given nucleus in a rigid solid, but like θ it takes on all possible values in a powder sample. If θ_R is set to 54.74°, then (3 $\cos^2\theta$-1)=0, and so the average, <3 $\cos^2\theta$-1> is zero also. The interaction anisotropy averages to zero if the spinning rate is fast so that θ is averaged rapidly compared with the anisotropy of the interaction,

This technique averages the anisotropy associated with any interaction which causes a shift in the energies of the Zeeman spin functions, such as chemical shift anisotropy, heteronuclear dipolar coupling, but no mixing between Zeeman functions (to first order). However, it also has an effect on secular interactions which mix Zeeman functions, i.e. homonuclear dipolar coupling. [9]

1.2 Diffusion

1.2.1 Random walk and Brownian motion

Diffusion is the translational motion of particles, which occurs in all liquids and gases and is driven by thermal energy. The induced random motion of the particles is called Brownian motion, and is caused by constant inter-particle collisions. This motion is named after the botanist Robert Brown, who in 1827 while looking through a microscope at pollen of the plant Clarkia pulchella immersed in water, the triangular shaped pollen burst at the corners, emitting particles which he noted jiggled around in the water in random fashion. He was not able to determine the specific motion till Albert Einstein in 1905 published a paper that explained how the motion that Brown had observed was a result of the pollen being moved by individual water molecules [22]. This explanation of Brownian motion served as convincing evidence that atoms and molecules exist. The direction of the force of atomic bombardment is constantly changing, and at different times the particle is hit more on one side than another, leading to the seemingly random nature of the motion.

Under equilibrium conditions as seen in Figure 18 , molecules of a system move only under Brownian motion (thermal conditions) which means that their position is changed even with the absence of a concentration gradient. This procedure is commonly known as self-diffusion a processes which can be described by a diffusion equation as:

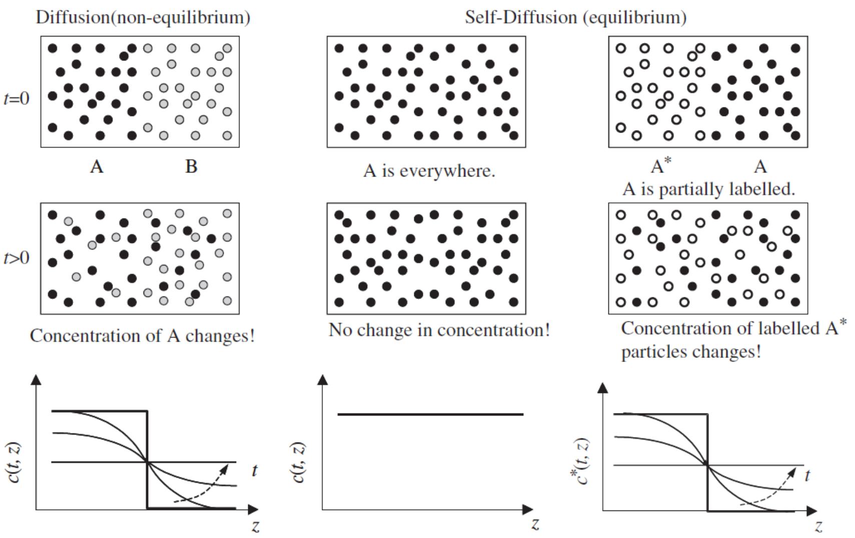
Diffusion(non-equilibrium)
Self-Diffusion (equilibrium)
t=0
A
B
A is everywhere.
A*
A
A is partially labelled.
t>0
Concentration of A changes!
No change in concentration!
Concentration of labelled A* particles changes!
c(t, z)
t
z
c(t, z)
z
c*(t, z)
t
z

Figure 18. Self-Diffusion coefficient Vs Diffusion coefficient under equilibrium and non-equilibrium conditions respectively [23]

Diffusion equations describes theoretically these two changes by transport diffusion and self-diffusion respectively. In order to be able to measure self-diffusion coefficient values we have to labelize the particle to observe their movement. As so the self-diffusion process is described as:

$$\frac{\partial c^*(r,t)}{\partial t} = D\nabla^2 c^*(r,t) \tag{38}$$

where c* is the concentration of the labeled particles. [23]

By solving the above diffusion equation (proposed in the book [24]) we derive the diffusion propagator P(r_1,r_2,t) quantity which describes the probability density to find a particle in the position r_2 at time t in the volume element dr with initial position r_1 at time t=0. For any other initial condition we can write:

$$\mathbf{P(r,t)} = \int_{\mathbf{V}} \mathbf{P(r_1 + r, r_1, t) p_0(r_1) dr_1} \tag{39}$$

Where we can replace r_2 position by the particle displacement r=r_2-r_1 so that P(r,t) will be the averaged propagator which describes the probability density that a particle will be places in the distance r at time t. If we consider a 3-dimensional homogeneous space where the molecules are normally distributed ,the average propagator will be described by a 3-dimensional Gaussian function:

$$P(r,t) = \frac{1}{\sqrt{(4\pi Dt)^3}} \exp\left(-\frac{(r(t)^2}{4Dt}\right) \tag{40}$$

Where $r(t)^2$ is the mean square displacement of a particle which can be described as

$$\langle \boldsymbol{r^2(t)} \rangle = \int_V \boldsymbol{P(r,t) r^2 dr} \tag{41}$$

The calculation of the second moment using the average propagator as described before result on an alternative definition of the self-diffusion coefficient also known as Einstein relation:

$$\langle \boldsymbol{r^2(t)} \rangle = \boldsymbol{6Dt} \tag{42}$$

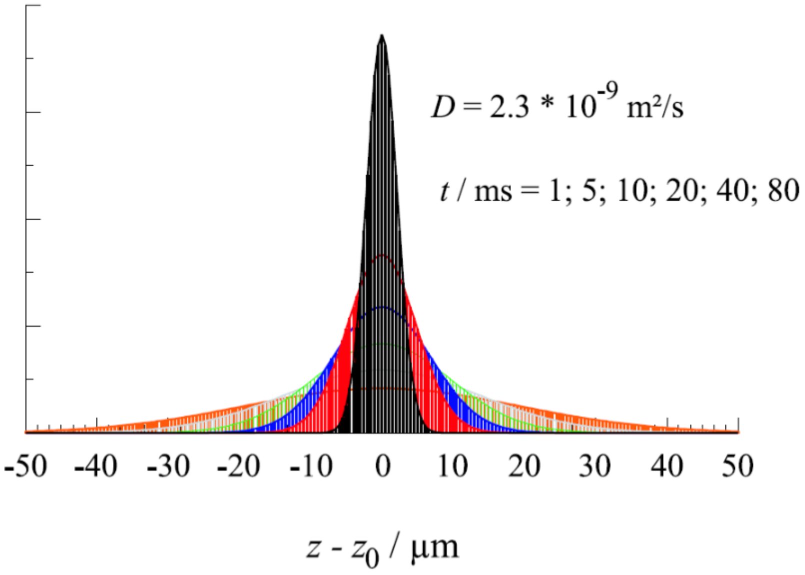

Figure 19. Spatial distribution of particles due to self-diffusion. The initial position is z-z_0=0 and for self-diffusion coefficient of water at 298K. [23]

1.2.2 NMR and Diffusion in a Field Gradient

When a static magnetic field gradient (G_Z) is applied then the magnetic field becomes a function of position:

$$\boldsymbol{B_Z = B_0 + G_z\, z} \qquad (43)$$

Because of the gradient, the Larmor frequency now depends on position:

$$\mathbf{f_l = \gamma B_0 + \gamma G_z\, z} \qquad (44)$$

This has two effects. Firstly dephasing of spins occurs and the also only a slice selection is observable due to a limited band width of the rf pulse. The thickness (δz) of the slice is described as :

$$\boldsymbol{\delta_z = \frac{1}{\gamma t_p G_z}} \qquad (45)$$

where t_p is the duration of the rf pulse. If the RF-pulse becomes longer, the band width becomes smaller and the slice thinner. A larger gradient also decreases the slice thickness as illustrated also in Figure 20.

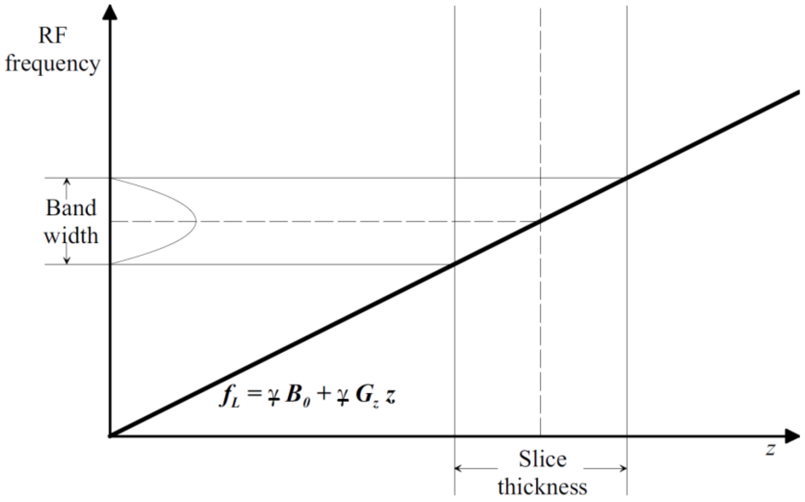

Figure 20. RF Frequency vs z axis and slice selection

The advantage of using a constant magnetic field gradient instead of a pulsed one is that:

(i) G in the stray field of a superconductive magnet is very strong, allowing the measurement of very slow diffusion processes

(ii) the time between pulses can be set to very short values, due to the absence of pulsed gradient stabilization effects, allowing measurements of very short T_2 values

(iii) the very high G value allows reliable measurement of diffusion in D-T_2 experiments with very low T_2 values, which fulfill the experimental constraints

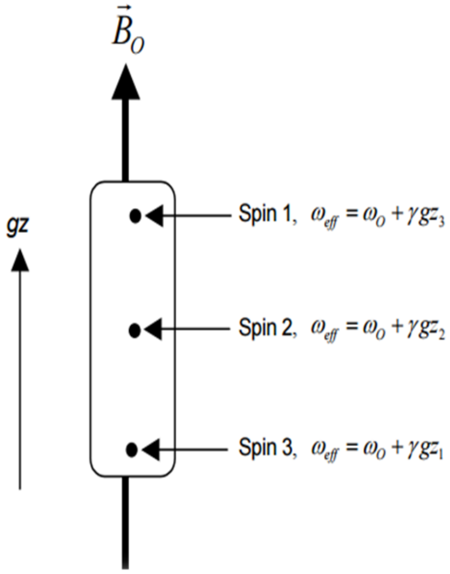
$\vec{B}_0$
gz
Spin 1, $\omega_{eff} = \omega_0 + \gamma g z_3$
Spin 2, $\omega_{eff} = \omega_0 + \gamma g z_2$
Spin 3, $\omega_{eff} = \omega_0 + \gamma g z_1$

Figure 21. Larmor frequency in magnetic field gradient

1.2.3 NMR and Diffusion in Porous Media

Molecules in the porous material will move randomly, they will probe the pore structure and this will influence the transverse relaxation times. Therefore, NMR can provide information on the pore-size distribution of a porous material. NMR experiments are able to provide information on pore-molecule interactions and the dynamics of the examined molecule through the characteristic relaxation times T_1 spin-lattice relaxation time and T_2 the spin-spin relaxation time.T_1 is associated with the dissipation processes from the spin system through all the other degrees of freedom the lattice and T_2 controls the dephasing within the spin system. These times are strongly influenced by the diffusion of the molecules through large internal magnetic field gradients arising from discontinuities in magnetic susceptibilities at pore wall interfaces.

Considering a spherical pore with a volume V and a surface S, which is completely filled with a liquid. The molecules in this pore will move randomly due to Brownian motion and this random motion is characterized by the self-diffusion coefficient D_0 and relaxation times T_1, T_2. Brownstein and Tarr in 1979 calculated the resulting relaxation times which are largely decreased for molecules near the pore wall as:

$$\frac{1}{T_{1,2}(\omega)} = \frac{1}{T_{1,2\ \mathrm{bulk}}} + \frac{\varepsilon S}{V}\frac{1}{T_{1,2\ \mathrm{surface}}(\omega)} \tag{46}$$

where ε is the thickness of the surface layer, ω/2π is the NMR frequency and S/V surface to volume ratio. Because the bulk relaxation time is much larger than the surface relaxation time which means that the principal contribution on the overall rate derives from the surface term which means that the first term can be neglected [25, 26].

1.3 2D D-T_2 and T_1-T_2 Correlation NMR techniques

Multi-dimensional NMR experiments became very popular recently because they can provide many useful information that one dimensional NMR experiments fail to provide. They are able to provide information about correlations between the variables of the experiment and be able to distinguish between the chemical or the physical environment. [8, 10]

Diffusion-editing CPMG experiment in which two-dimensional (2D) experiments are performed with a leading diffusion experiment and followed by a T_2 sensitive CPMG pulse train.

The acquired 2D dataset is processed with a 2D inverse transform (2D-Tikhonov) resulting in 2D maps, which correlates diffusion coefficients and transverse relaxation times (D-T_2)

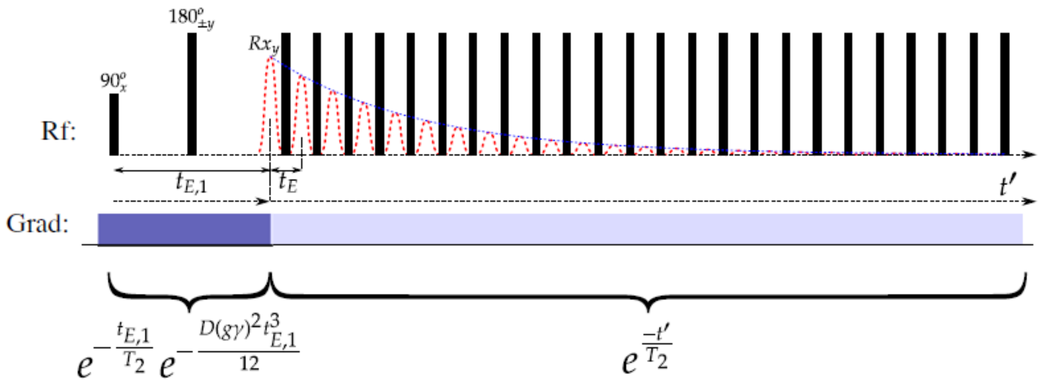

Figure 22. D-T2 Pulse Sequence

1.4 Tikhonov Regularization algorithm

Tikhonov Regularization is a popular way to deal with linear discrete ill-posed problems. Ill-posed problems violate one of the terms of a well-posed problem which means that they do not have a solution that is unique and they have a solution that changes as the initial condition changes. Regularization stabilizes ill--posed problems, giving accurate approximate solutions — often by including prior information (Vogel). The numerical solution of linear discrete ill-posed problems typically requires regularization, i.e., replacement of the available ill-conditioned problem by a nearby better conditioned one. One of the most popular regularization methods which allows the evaluation of the singular value decomposition of the matrix defining the problem is Tikhonov regularization Algorithm. When using this method all the NMR data (eg. relaxation and diffusion) can be modelled by a Fredholm integral equation of the first kind :[27-31]

$$\frac{h(t)}{h(0)} = \int_0^\infty k_0(x,t)p(x)\mathrm{d}x \tag{47}$$

Where h(t) h(0) is the normalized signal without the noise at time t and p is the density distribution governed by the time constants x and k_0 is the model function which describes the signal. In the $\log_{10}$ scale we have

$$\frac{h(t)}{h(0)} = \int_0^\infty k_0(x,t)f(x)\mathrm{d}(\log_{10}x) \tag{48}$$

As a result the inversion method provides f(x) and not the actual density distribution The determination of f(x) from h(t) is the difficult inverse problem that we have to solve. In NMR experiments the data that we acquire from the experiments will form an equation of the form g(t)=h(t)+e(t)where e(t) is the noise which forms a Gaussian distribution. The model kernel will be of the form

$$k_0(x,t) = \exp\left(-\frac{t}{x}\right) \tag{49}$$

Our goal is to invert the one dimension al 1D Fredholm integral of the previous equation to determine the optimal distribution of f(x). In 2D NMR experiments data are acquired through 2 dimensions the direct and the indirect. Direct dimension is usually the experiments are acquired through single shot techniques as T_2 through Carr Purcell Meiboom Gill CPMG echo experiments and the indirect dimension is measured through multiple experiments by varying some precondition parameter like T_1 relaxation experiments via the inversion recovery method. When we are working with two dimensions we need to extended the Fredholm equation of the first kind into two dimensions as[29, 32, 33]

$$\frac{h(t_1,t_2)}{h(0,0)} = \int_0^{\infty}\int_0^{\infty} k_0(x_1,t_1,x_2,t_2) f(x_1,x_2)\, \mathrm{d}(\log_{10}x_1)\, \mathrm{d}(\log_{10}x_2) \tag{50}$$

Where the index 1,2 denotes the direct and indirect dimension respectively. The analysis of the data is described as 1D vector which comes from the 2D matrix of the experimental data

A general overview of the key stages of the inversion process that follows and the structure of this procedure is shown in Figure 23

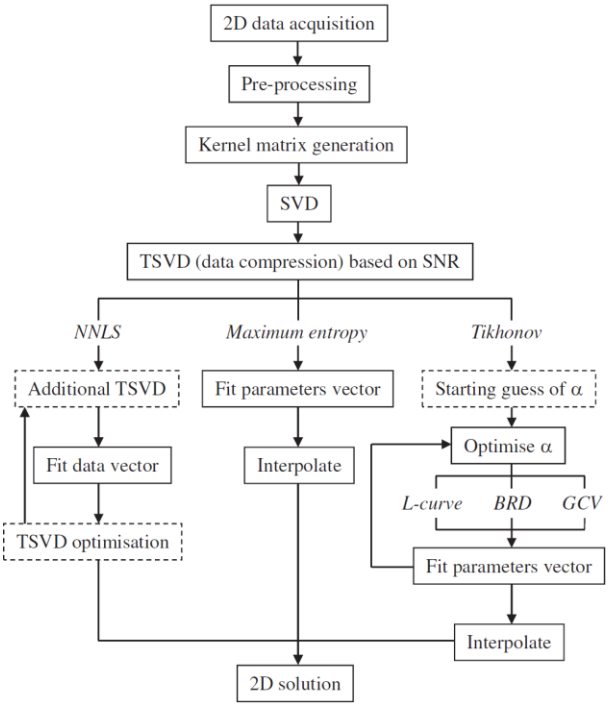
2D data acquisition
Pre-processing
Kernel matrix generation
SVD
TSVD (data compression) based on SNR
NNLS
Maximum entropy
Tikhonov
Additional TSVD
Fit parameters vector
Starting guess of α
Fit data vector
Interpolate
Optimise α
L-curve
BRD
GCV
TSVD optimisation
Fit parameters vector
Interpolate
2D solution

Figure 23. The key stages in the inversion of 2D relaxation or diffusion data [29]

In the final stage of this process we unwrap the 2D data matrix G into a 1D vector g by stacking the individual columns of G as shown in

Figure 24. The kernel matrix now will be transformed in order to encompass all the values of $t_{1,2}$ and $x_{1,2}$ on the $\log_{10}$ scale, and satisfy the expression $\mathbf{g=K_0f+e}$. This optimization problem in this vector–matrix notation is shown in the following Figure where K_0 is real. Considering the size of all the vector and matrices determining and storing K_0 is computationally extremely expensive so the following step is to compress G in order to reduce the size of K_0.

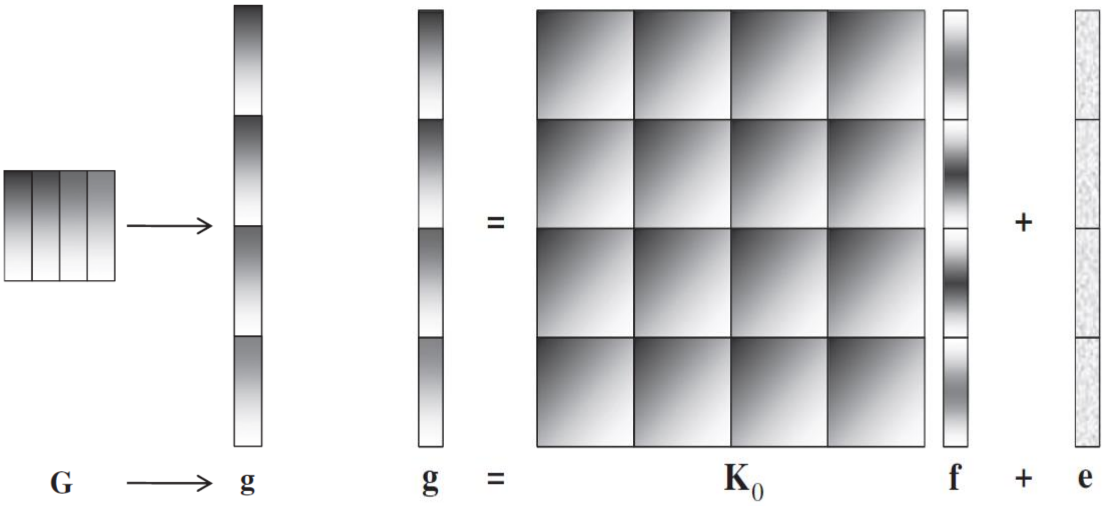

Figure 24. Graphical Representation of the transformation of data matrix G into vector g and then the optimization problem expressed in vector matrix notation (gray scale denotes black-maximum signal, white-zero signal) [29]

The degree of smoothing on the solution will be determined by the size of F as shown in Figure 25 which implies there are more unknowns than equations to be solved. In the case of Tikhonov regularization, f is substituted with a vector of fitting parameters containing as many parameters as there are elements in g.

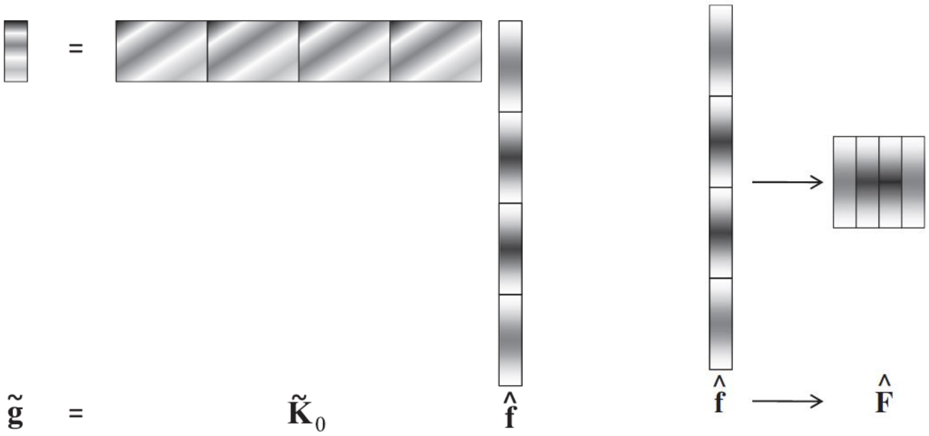

Figure 25. The compressed optimization problem and the reshape of the solution f into a matrix [29]

The last step in this procedure is to reverse the initial process G→g in order to get the final 2D distribution F by reshaping the vector f as illustrated in Figure 25. Further details on the mathematical approach and on the algorithm can be found in Ref [27-29] [31-36]

2. Experiments

2.1 Experimental Apparatus

In this chapter we are going to present the basic instrumentation used to conduct the NMR experiments. All the measurements were conducted in Superconductive magnets of Nuclear Magnetic Resonance Laboratory of Institute of Nanoscience and Nanotechnology at NCSR Demokritos.

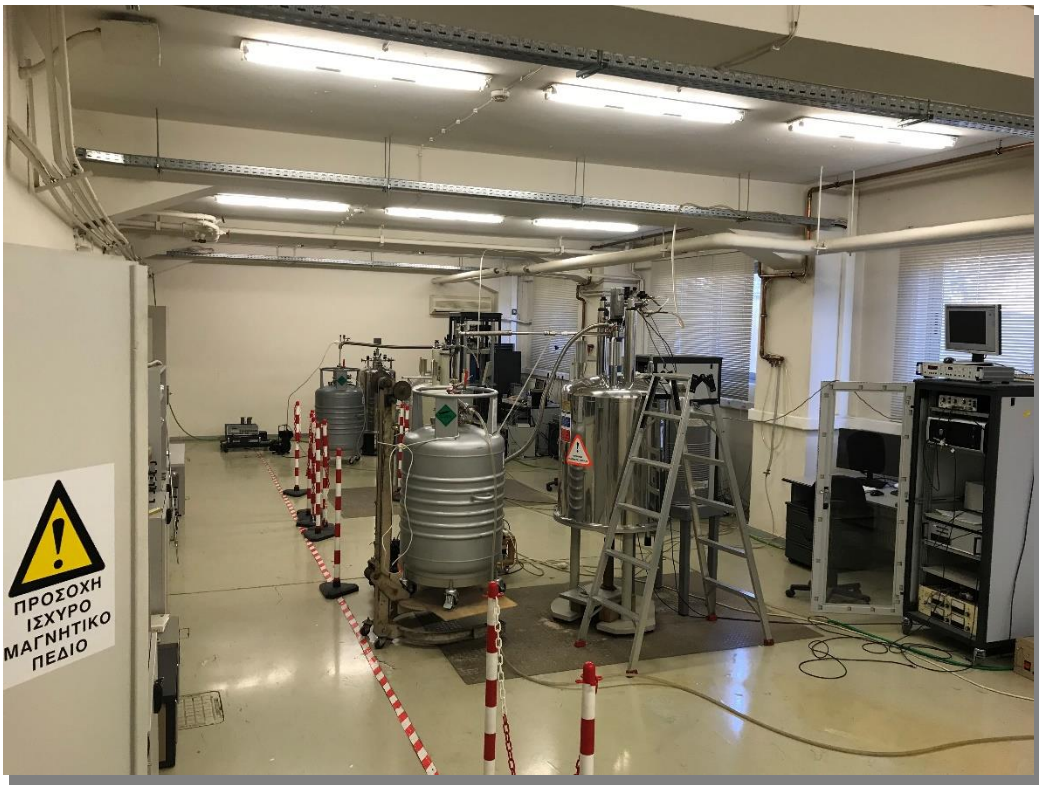

Figure 26. NMR Laboratory of INN at NCSR Demokritos

➢ 4.7T, 9.4T Bruker Superconducting magnet

Superconducting magnet of 4.7 T and proton ^{1}H Larmor frequency of 200MHz. It provides 34.7 T/m constant magnetic field gradient. Additionally experiments were performed in the superconducting magnet of 9.4T and proton ^{1}H Larmor frequency of 400MHz

➢ Temperature Controller

ITC5 Temperature Controller by National Instruments

➢ NMR home build spectrometer

Broadband home-built NMR spectrometer was used operating in the frequency range 5 MHz - 1 GHz.

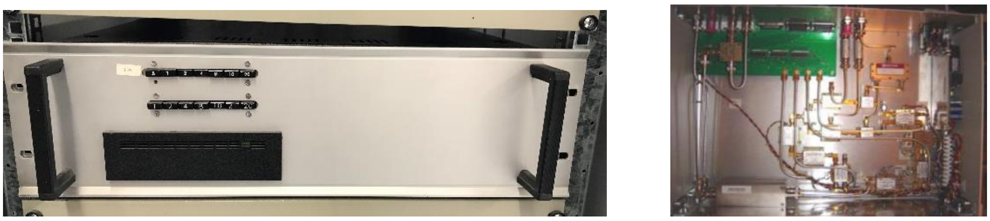

Figure 27 NMR Spectrometer at INN

➢ Frequency Generator

The frequency generator creates the frequency signal for the spectrometer. The radio frequency (RF) to be set is the sum of the spectrometer's internal working frequency and the chosen frequency for the experiment. It also produces the reference frequency of 10MHz for the spectrometer. We used the National Instruments digital card NI in the PXI system

➢ Pulse Amplifier

The pulse package is strongly amplified, and is given forward through the duplexer to the probe head. Because of the amplifier's slow response the gate/delay is set before the amplifier

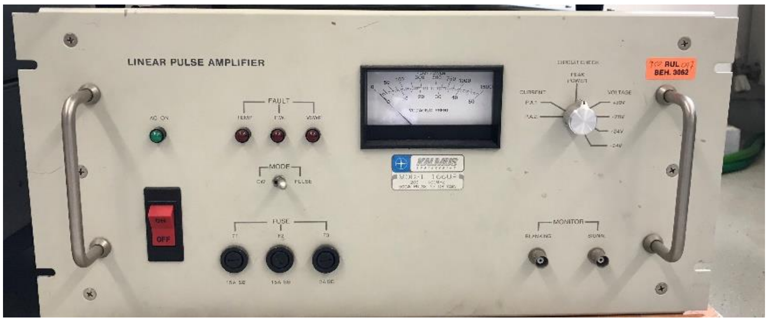

Figure 28. RF Generator

➢ Preamplifier

Amplifies the weak spin signal and sends it to the spectrometer. The amplification is of 53:5 dB according to the constructors data sheet. Antiparallel diodes are set to the ground before the preamplifier to prevent damage on it through extruding remnants of the pulse. This way voltages over 0.6V are absorbed.

➢ National Instrument PXI Chassis

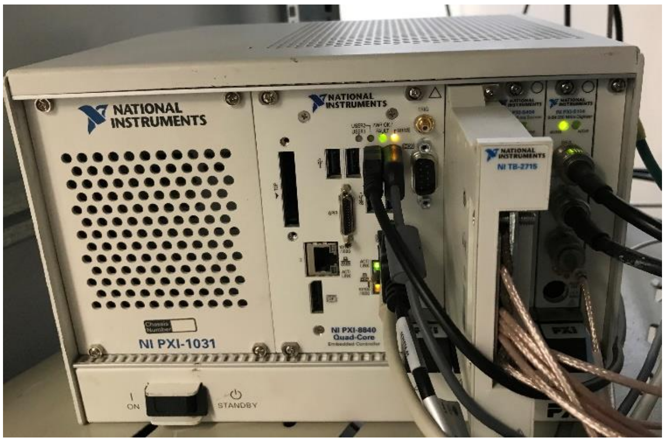

Figure 29. NI PXI-1031

The National Instruments PXI-1031 chassis contains the following:

NI 6534 card

NI 5114 card

PXI-8840Controller

➢ National Instrument PXI Controller

NI-784341-04 2.6 GHz quad-core Intel i7-5700EQ PXI-8840Controller

- **Oscilloscope**

The received complex signal is shown on the screen, temporarily saved in the memory, and its average is calculated. Up to one million entries can be summed. Over digital port the complex data is passed to the computer through National Instruments NI 5114 card

- **Digital I/O**

  National Instruments NI 6534 card

- **Software**

  The software runs on LabVIEW on a Windows 10 64bit operating system3. Build in Software in Labview able to conduct 1D 2D and PFG NMR experiments.

- **NMR Probe**

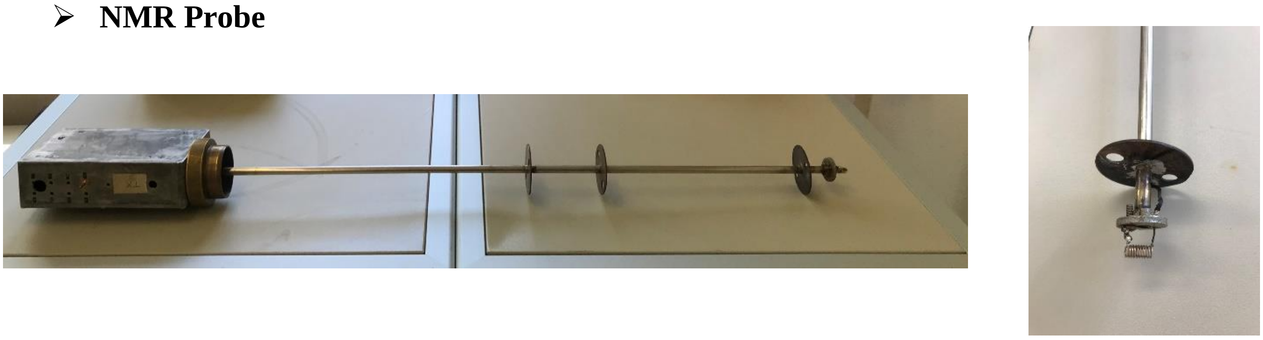

Figure 30. Home build NMR probe head able to conduct measurements in 100MHz

The main purpose of the electrical system of the probe head is to deposit the major part of electrical energy as an oscillating magnetic field in the coil where the sample is placed. Moreover it is supposed to pick up the voltage, which is the response of the spinning nuclear magnetic moments. In order to avoid reactions the electric impedance of the resonance circuit has to match the impedance of the amplifiers, which have internal impedances of 50Ω. As a result on the top of the probe head there is the stainless steel die cast aluminum box which contains the resonance circuit (2 capacitors etc) specifically build-in in order to be able to conduct experiments on 100MHz and on the lower part there is the build-in coil.

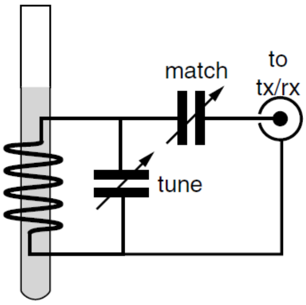
match
to
tx/rx
tune

Figure 31 NMR Probe

Schematic representation of the key parts of the probe. The coil is shown on the left with the sample tube and a tuned circuit is formed by a capacitor "tuning". The power transfer to the transmitter and receiver (tx. and rx.) is optimized by adjusting the "matching" capacitor. A schematic block diagram of the basic parts of the NMR experiment is shown in the following figure.

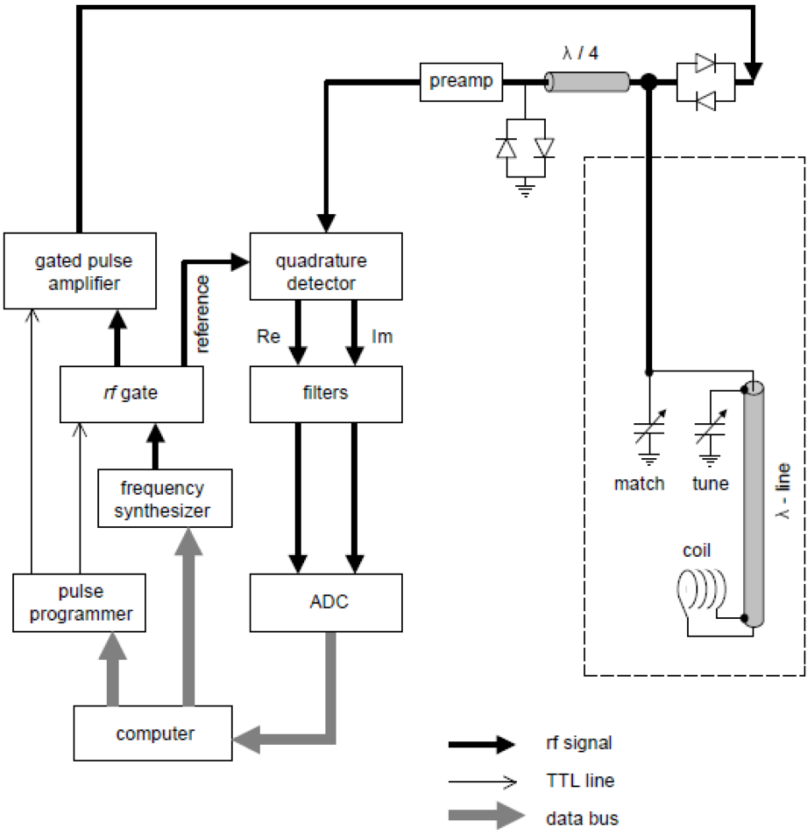
preamp
λ / 4
gated pulse amplifier
quadrature detector
reference
Re
Im
rf gate
filters
frequency synthesizer
match
tune
λ - line
coil
pulse programmer
ADC
computer
rf signal
TTL line
data bus

Picture 1. A schematic block diagram of the basic NMR apparatus

2.2 Setting up a solid-state NMR experiment

Measurements were performed on a broadband home-built NMR spectrometer operating in the frequency range 5 MHz - 1 GHz. The probe was placed in the stray field of a 4:7 T Bruker magnet with a magnetic field gradient G=34:7 T/m at ^{1}H NMR frequency of 101:324 MHz.

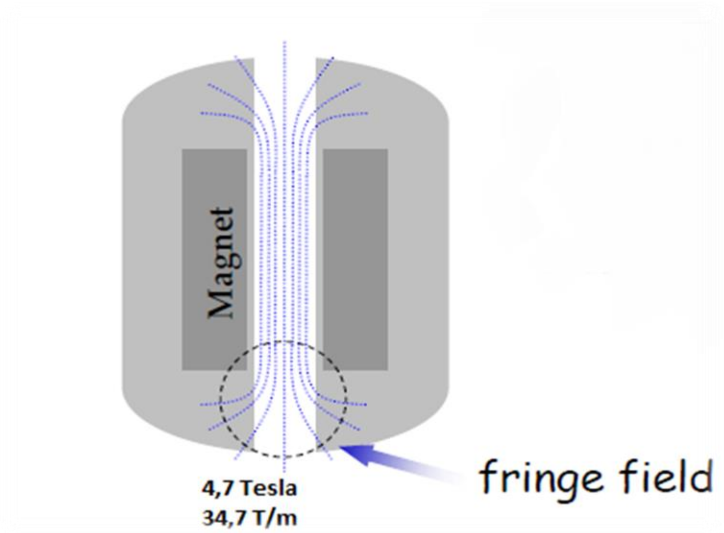

Figure 32. Schematic presentation of the fringe field of a Superconducting magnet

This was achieved by lifting the cryostat at that position of the fringe field of the superconductive magnet, where the NMR frequency was varying linearly with the position the magnetic field gradient in the z-direction is constant.

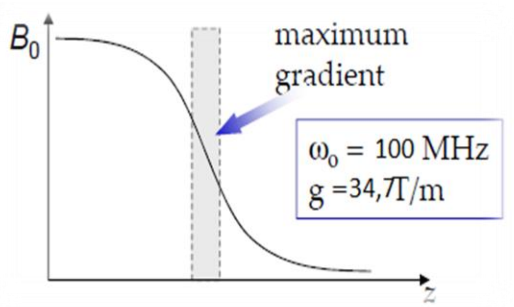

Figure 33. Diagram of B vs z of the magnetic field. The field gradient is constant and linear for a certain area of z

3. Carbon Nanotubes CNTs

Carbon nanotubes (CNTs) are allotropes of carbon with a cylindrical nanostructure. They are large molecules consisting of a hexagonal arrangement of sp2 hybridized carbon atoms The distance between any two adjacent carbon atoms is about 0.14 nm. The form of a Carbon Nanotube can be visualized by rolling one graphene sheet seamlessly into a carbon tube. They are rolled-up sheets of single-layer carbon atoms (graphene) as seen in Figure 34.

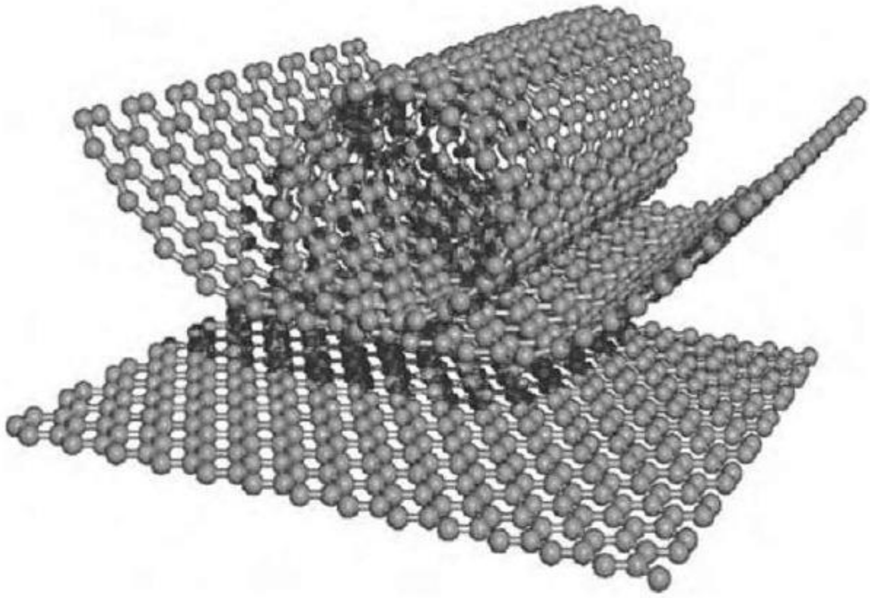

Figure 34. Rolling up a carbon nanotube

There are 2 big groups of CNTs depending on the number of graphene layers. The wall of the CNTs consists of a single (SWCNT) layer or multiple (MWCNT) layers of graphene sheets.

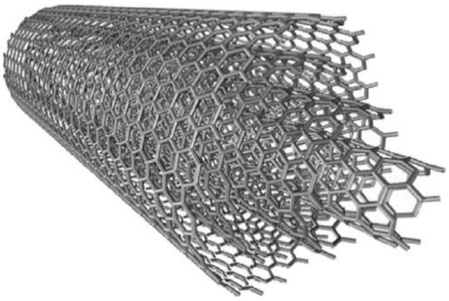

Figure 35. Multiple layers of CNTs

The properties of a CNT depend on how they are rolled up. The structures can be specified completely by their chiral vectors, which are defined by the chiral indices (n, m) giving three different types of CNTs; armchair, zigzag, and chiral.

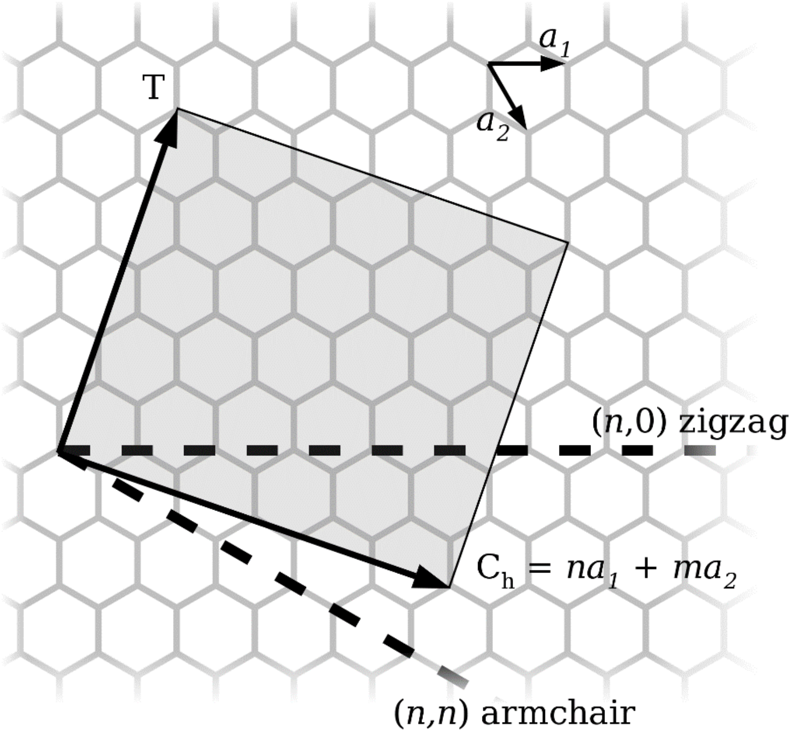

Figure 36. Chiral Vector of CNTs

The interlayer separation of the graphene layers of MWCNTs is approximately 0.34 nm in average, each one forming an individual tube, with all the tubes having a larger outer diameter (2.5 to 100 nm) compared to that of SWCNTs (0.6 to 2.4 nm). The latter has a better defined wall, whereas MWCNTs are more likely to have structural defects. The quasione-dimensional character of SWCNTs has attracted more and more research attention on the water adsorption on their surface, partly due to the fact that SWCNTs can be used as a model system for understanding water transport in biological cells and possibly for drug delivery applications Many cancer drugs are hydrophobic in nature and CNT is one of the potential materials as drug carrier

3.1 Single Wall Carbon Nanotubes (SWCNTs) Double Wall Carbon Nanotubes (DWCNTs) and Multi Wall Carbon Nanotubes (MWCNTs)

3.1.1 Materials

Purified and open-ended SWCNTs and DWCNTs were purchased from SES research, USA.

Picture 2. SES Research samples of CNTs

The inner and the outer diameter of the CNTs used in this work are represented in the following tables.

Carbon Nanotubes	Inner/Outer diameter
Single Wall	1.2nm / 2.0nm
Double Wall	3.5nm / 5.0nm
Average length ~1µm	

Table 1 SWCNTS and DWCNTs inner and outer diameters

The outer/inner diameters of the CNTs used in the first part of this work were 2/1.2 nm for SWCNT and 5/3.5 nm for DWCNT. Both types of CNTs had average length 1μm. Morphological analysis of the CNTs was performed with Transmission Electron Microscopy (TEM) using an FEI Tecnai G20 microscope with a 0.11 nm point to point resolution, operated at 200 kV in the infrastructure at INN on NCSR Demokritos. For this analysis, approximately 1 mg of each sample was dispersed in 20 ml of high purity cyclohexane (Merck, 99.9 %) via sonication (15 s) a drop of each suspension was deposited on copper grids (400 mesh) covered with a thin amorphous carbon film (lacey carbon). To avoid contamination, CNT samples were inserted into the TEM machine immediately following preparation. Bright field images were collected at several magnifications in order to observe structure and size homogeneity. Figure 37 shows representative TEM images of SWCNT and DWCNT samples.

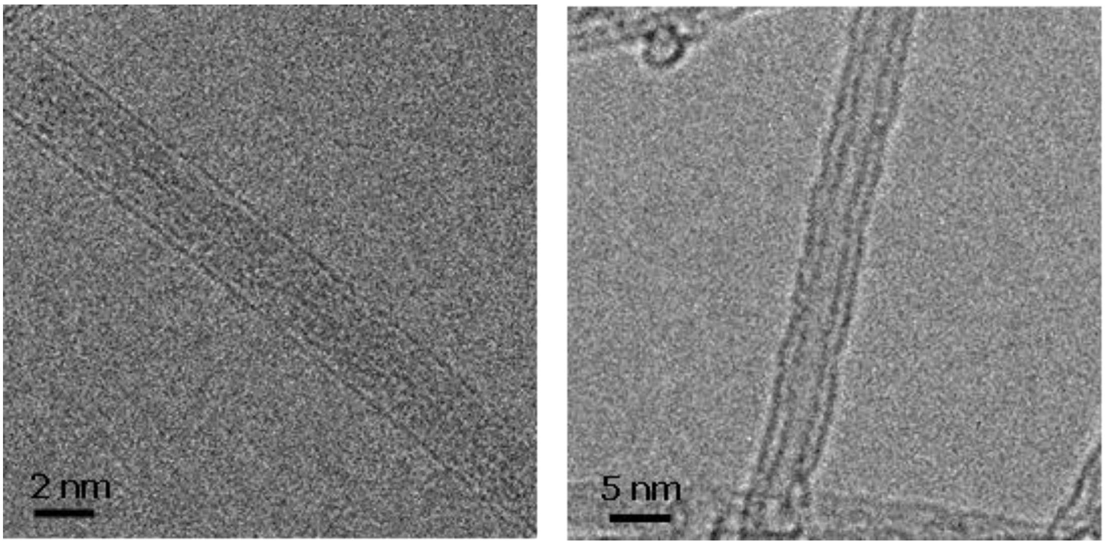

Figure 37. TEM images for the SWCNT (left) of outer/inner diameter of ~ 2/1.2 nm and DWCNT (right) of diameter of ~5/3.5 nm

Further MWCNT samples were purchased from Nanocs, USA with inner diameters of 3.0 nm, 5.0 nm, 5.5 nm, and 6.0 nm and outer diameters <8nm, 10-15nm, 20-30nm and 30-40nm respectively. The length of the CNT channels were about 20μm and all the CNTs were open ended as provided by the manufacturer.

Carbon Nanotubes	Inner/Outer diameter
Multi Wall	3.0nm / <8.0nm
Multi Wall	5.0nm / 10-15nm
Multi Wall	5.5nm / 20-30nm
Multi Wall	6.0nm / 30-40nm
Average length ~15-20µm	

Table 2 MWCNTS inner and outer diameters

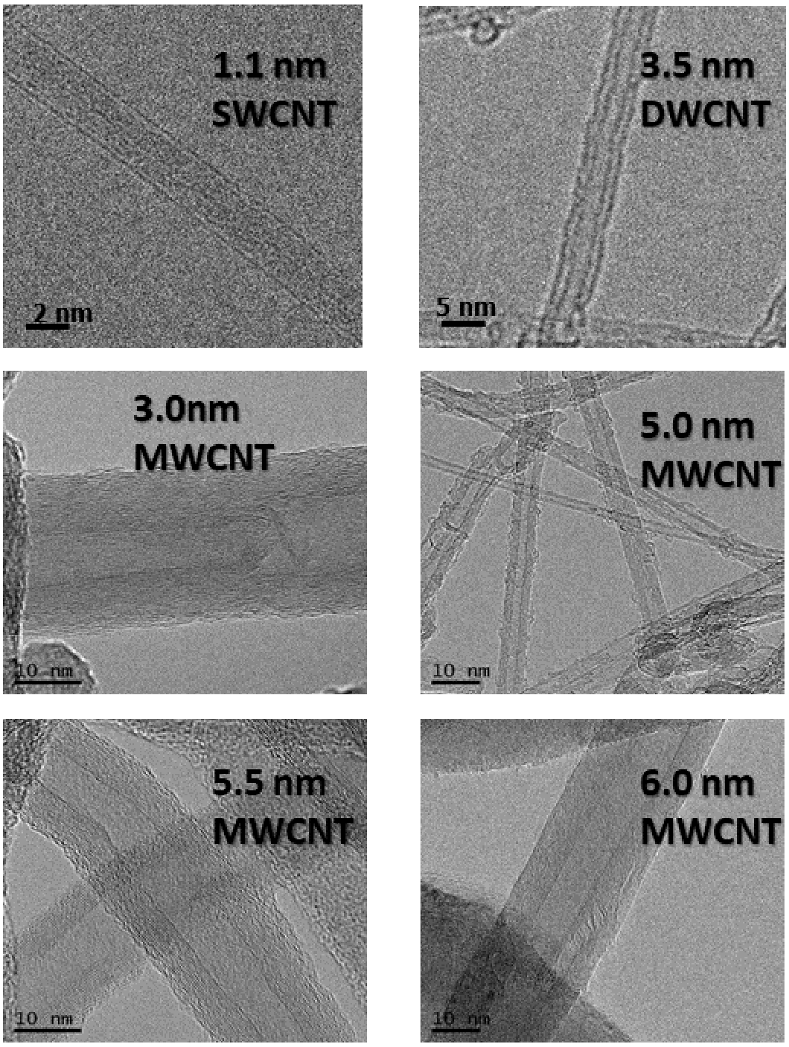
1.1 nm
SWCNT
2 nm
3.5 nm
DWCNT
5 nm
3.0nm
MWCNT
10 nm
5.0 nm
MWCNT
10 nm
5.5 nm
MWCNT
10 nm
6.0 nm
MWCNT
10 nm

Figure 38. Representative TEM images of the MWCNT samples. The inner diameter of CNTs is indicated within each image

3.2 Unveiling the ultrafast stratified diffusion of water inside carbon nanotubes; direct experimental evidence with 2D D-T_2 NMR spectroscopy

3.2.1 Preparation of the samples for NMR measurements

For the NMR experiments, CNT powders were used with no further treatment and double-distilled water was used in all measurements. Samples with different water-content were prepared by immersing CNT powders in deionized water, inside NMR quartz tubes (inner diameter 3 mm, length 25 mm) as seen in Figure 39

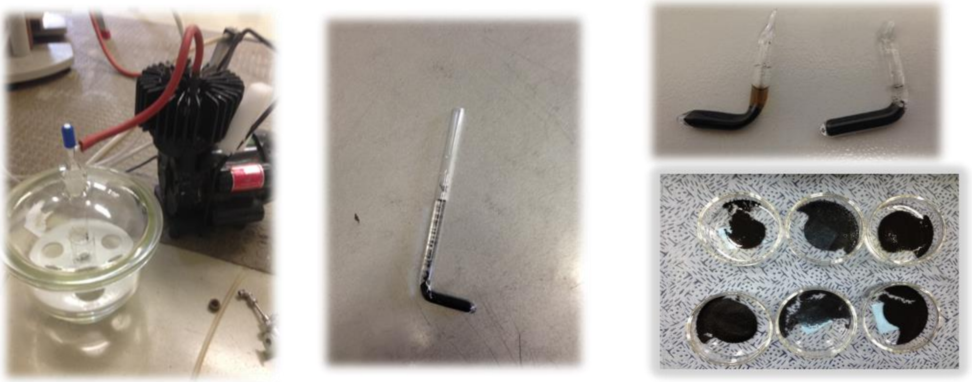

Figure 39. Preparation of the samples for NMR measurements

Specifically, 30 mg of SWCNTs and 40 mg of DWCNTs were mixed in the tubes with 260μl and 270μl of deionized water, respectively. Samples were let to come to equilibrium at room temperature for a couple of hours. The NMR tubes were then connected to a vacuum system as seen in Figure 39 and air was carefully pumped out to ensure water entering into the CNT nanotubes. A water loss of 5 -10 μl was observed at the end of the process. Subsequently, the NMR tubes were left at ambient conditions for different time intervals, ranging from 8 hours to 96 hours, to prepare samples with different water-content. Each sample was then flame sealed under low vacuum. With this procedure, the overall water content in the DWCNT samples as seen in Figure 40 was measured to be 260 μl (fully saturated), 90 μl (medium saturated) and 50μl (low saturated). ratios of the total area of the relevant ^{1}H NMR T_2 distributions (obtained after inverting the ^{1}H NMR CPMG spin echo decay train, as explained later).

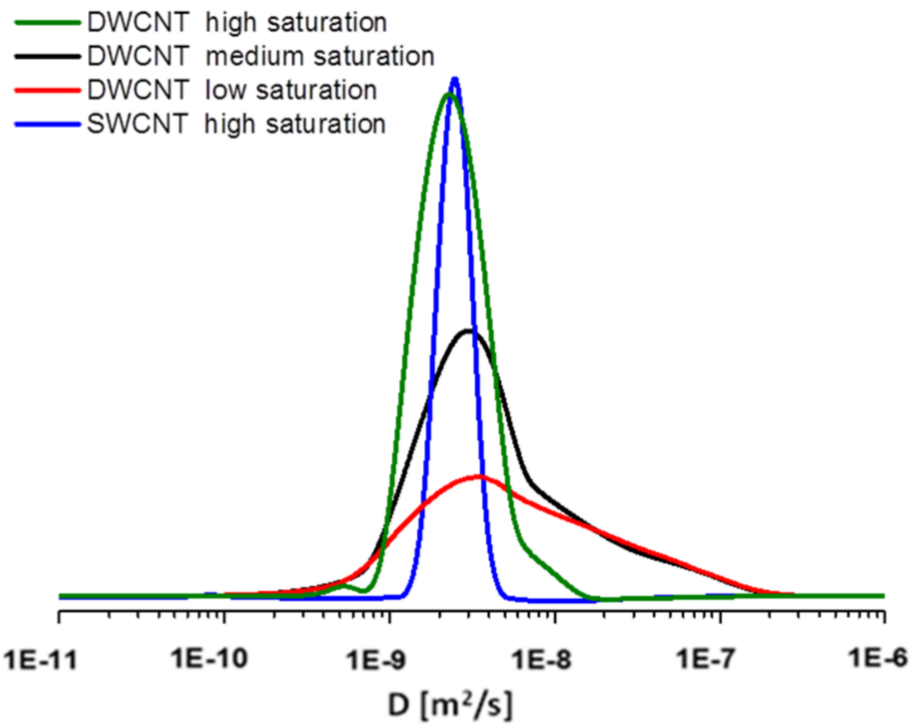

Figure 40. Diffusion profile of water in SWCNTs and DWCNTs at room temperatures at different water content. For better visualization the spectra are rescaled accordingly. Upon the lowering water content, the profile moves toward higher values of D, in agreement with MD simulation results [37]

A good match between the two sets of measurements was obtained. Subsequently, the nanotube water saturation level was estimated by comparing the areas corresponding to the low T_2 signal component of the nanotube water, considering that the nanotube water saturation of the first sample is 100%. In this way the nanotube water saturation level of the three samples in Figure 40 was estimated to be 100% (fully saturated), 60-70% (medium saturated), and 30-35% (low saturated). It should be stressed that

(i) only a thin sample-slice is observed with ^{1}H NMR in the strong magnetic field gradient in the stray field of the superconducting magnet, as shown in Figure 20 on the theory part on page 66, so exact volumetric analysis from the NMR water signal is not possible

(ii) most water in the fully hydrated sample is coming from bulk water, as only 12 - 15% of the signal intensity remains after freezing to 275 K

3.2.2 ^{1}H NMR T_1, T_2 and T_1 -T_2 relaxation analysis of water in CNTs

1D ^{1}H NMR spin-lattice relaxation T_1 and spin-spin relaxation T_2 measurements, as well as 2D T_1-T_2 correlation spectroscopy were performed

- in magnetic field 9:4 T at Larmor frequency 400 MHz
- in the stray field of a 4.7 T superconductive magnet at Larmor frequency 101.324MHz
-

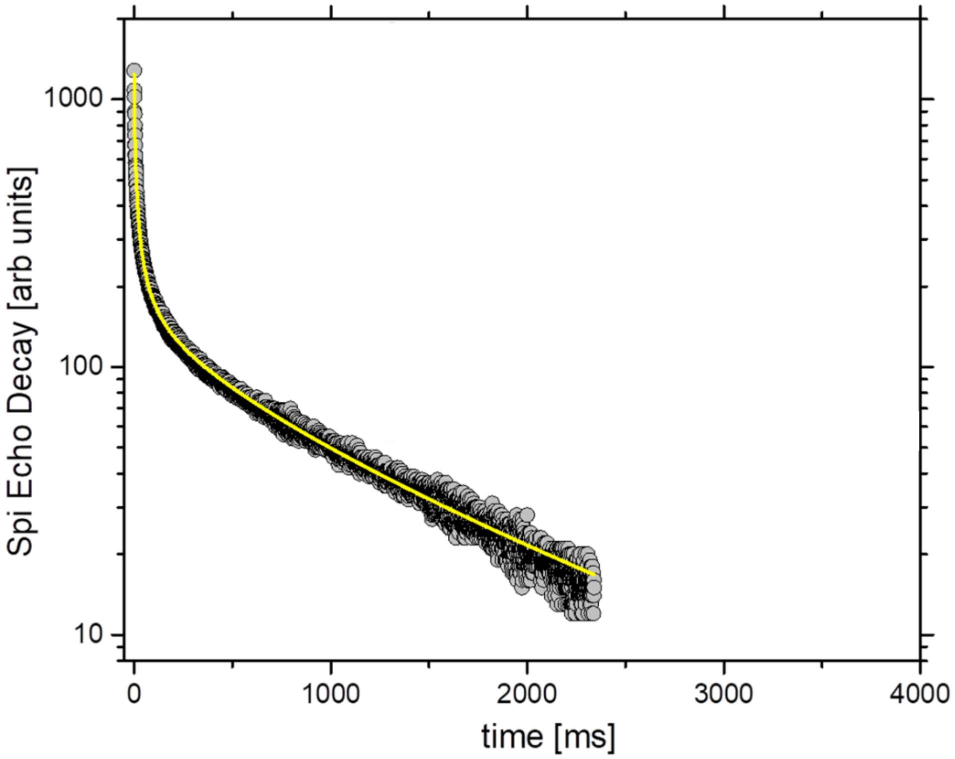

Figure 41. ^{1}H NMR CPMG spin echo decay of water in DWCNT, at room temperature, in a magnetic field 9.4 T (400 MHz). The yellow line is the theoretical fit by applying the 1D Tikhonov regularization inversion

Figure 41 shows the spin echo decay obtained with a CPMG pulse sequence in 9:4 T, of water in DWCNT sample, at room temperature. The yellow line is the theoretical fit by implementing 1D-nonnegative Tikhonov regularization algorithm.

In Figure 42 we applied 1D-nonnegative Tikhonov regularization algorithm for the T_2 distribution in 9.4T (gray circles). Water is shown to be grouped in two main T_2 peaks; a low-intensity narrow peak with T_2 = 1:2s (bulk water), and a second broad line with a peak at 10 ms, corresponds to interstitial water as well as nanotube water. These assignments are confirmed with T_1 measurements (cyan circles), obtained with the inversion recovery pulse sequence ($\pi - t - \pi/2$). T_1 shows a peak with T_1 value coinciding with the long T_2 component (as expected for bulk water), and the second one with T_1 value significantly higher than the short T_2 component, as expected for interstitial and nanotube water molecules. Important observation is that the T_2 projection of the D-T_2 contour plot at 295K (green circles), coincides with the T_2 distribution of nanotube and interstitial water at 9.4 T (grey circles). This is a direct evidence of the correct assignments of the water signals in the 2D D-T_2 measurement, which are presented in the next chapter. However, in the fringe field of the magnet effective T_2 values are influenced by the diffusion in the strong magnetic field gradient.[38] To minimize the contribution of bulk water into the NMR signal, the repetition time of the D - T_2 NMR experiments was set to 1 sec. At lower repetition times sample heating was observed, due to the extremely high number of π pulses in the CPMG pulse-train.

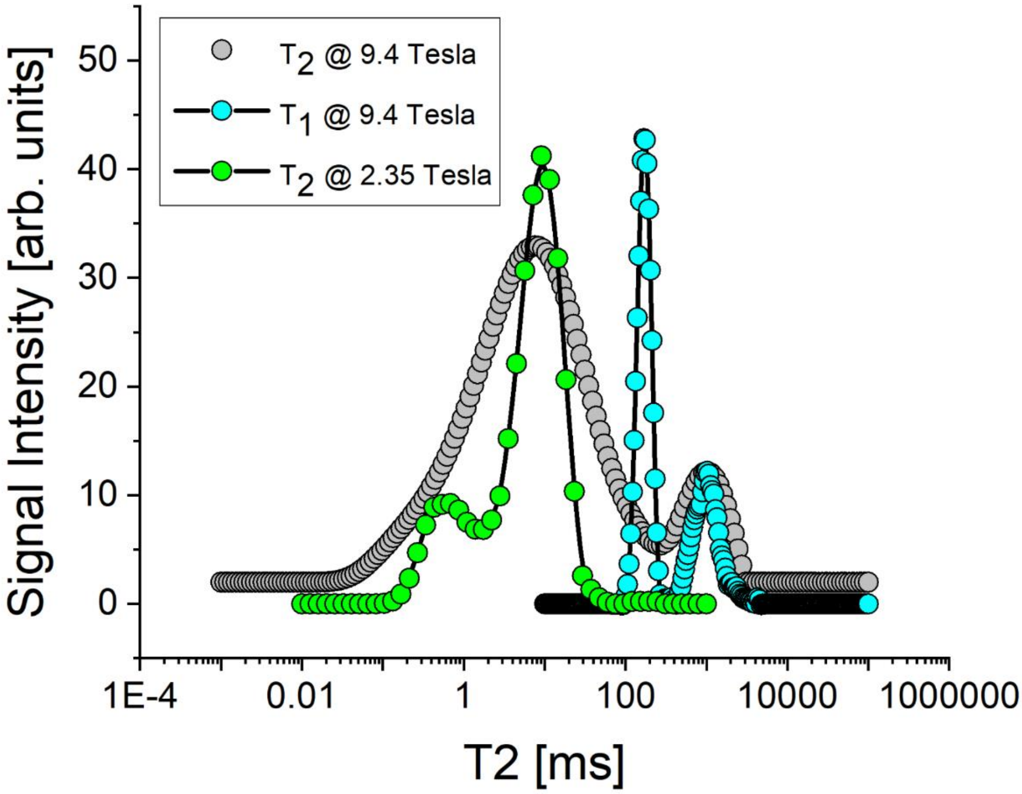

Figure 42. The graph shows the relevant ^{1}H T_2 distribution (gray circles), ^{1}H T_1 distribution (cyan circles) as well as T_2 distribution obtained from 2D D-T_2 (green circles)

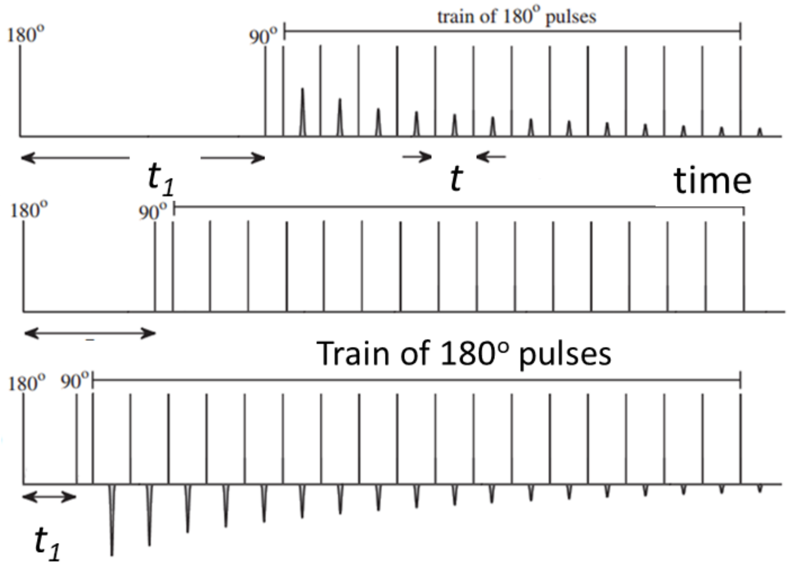
180°
90°
train of 180° pulses
t1
t
time
180°
90°
Train of 180° pulses
180°
90°
t1

Figure 43. The T$_1$-T$_2$ NMR pulse sequence used in the experiments

The 2D ^{1}H NMR T$_1$-T$_2$ pulse sequence is shown in Figure 43. It consists of a π - t_1 – $\pi/2$ Inversion Recovery pulse sequence, followed by a CPMG spin-echo decay train [39, 40].

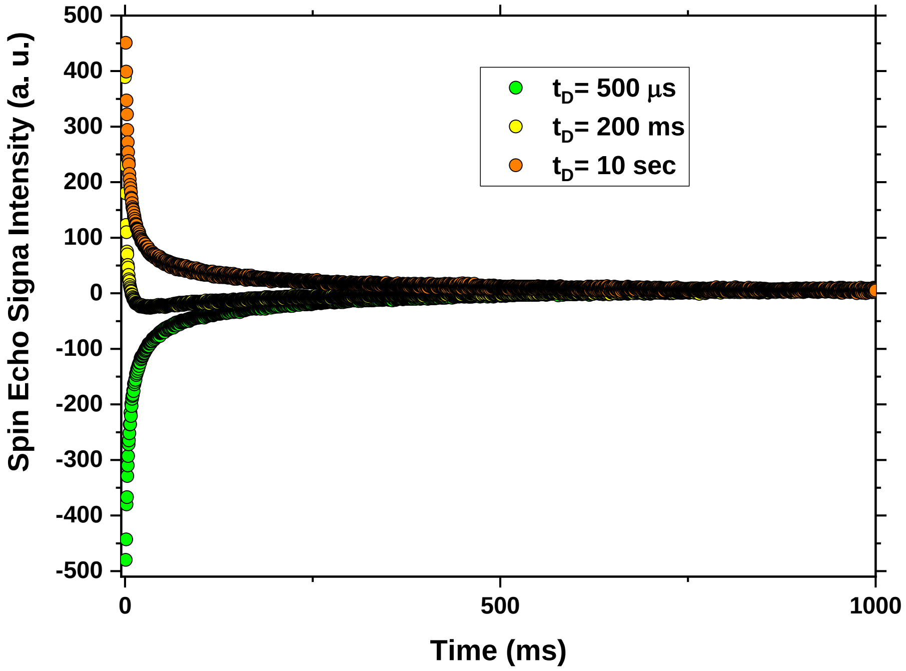

Figure 44. The CPMG spin-echo decay for three different t_D time

Figure 44 demonstrates the SEDs at three different t_D values. The intensity of the SEDs as a function of t_D look to vary from negative values for short t_D values to positive values for long t_D values, following the relation:

$$\boldsymbol{M = M_0\left(1 - 2e^{\frac{t_1}{T_1}}\right)} \qquad \textbf{(51)}$$

However, in the presence of a broad T_1 and T_2 distribution, the ^1H NMR T_1-T_2 spectrum, i.e. the distribution function $f(T_1,T_2)$ [29] is obtained by applying a non-negative 2D Tikhonov inversion algorithm on the time domain data, according to the equation:

$$\boldsymbol{\frac{g(t_1,t)}{g(0,0)} = \iint_{-\infty}^{+\infty} \left(1 - 2e^{-\frac{t_1}{T2}}\right)\left(e^{-\frac{t}{T_2}}\right) f(T_1,T_2)\, dT_1\, dT_2} \qquad \textbf{(52)}$$

The ^1H NMR T_1-T_2 spectrum of DWCNTs at room temperature is presented in Figure 45. To further examine different water groups in CNTs, ^1H NMR T_1–T_2 correlation spectroscopy was performed under static conditions (no MAS), as shown in Figure 45. 2D T_1–T_2 provides information about the “liquidity” of the local molecular environment: in general, molecules in unconstraint liquid environment are characterized by $T_2 \approx T_1$, whereas molecules in a rigid (solid) environment show $T_2 \ll T_1$. In this context, bulk water with $T_2 \approx T_1$, semi-free interstitial water with $T_2 < T_1$, and solid-like nanotube water with $T_2 \ll T_1$ can be distinguished in Figure 45.

It is stressed that according to MD the interaction of water with the CNT walls depends on the wall curvature; in the outer space, water molecules are shown to interact moderately with the external CNT surfaces, whereas inside the CNTs, water molecules do not interact with the CNT walls [41, 42]. Evidently, the very short $T_2/T_1 \ll 1$ ratio of water inside the CNTs indicates that nanotubular water molecules are in a rigid molecular environment. This fact corroborates with the predictions from MD simulations, which show that water molecules in CNTs are organized in hydrogen-bonded nanotubular clusters

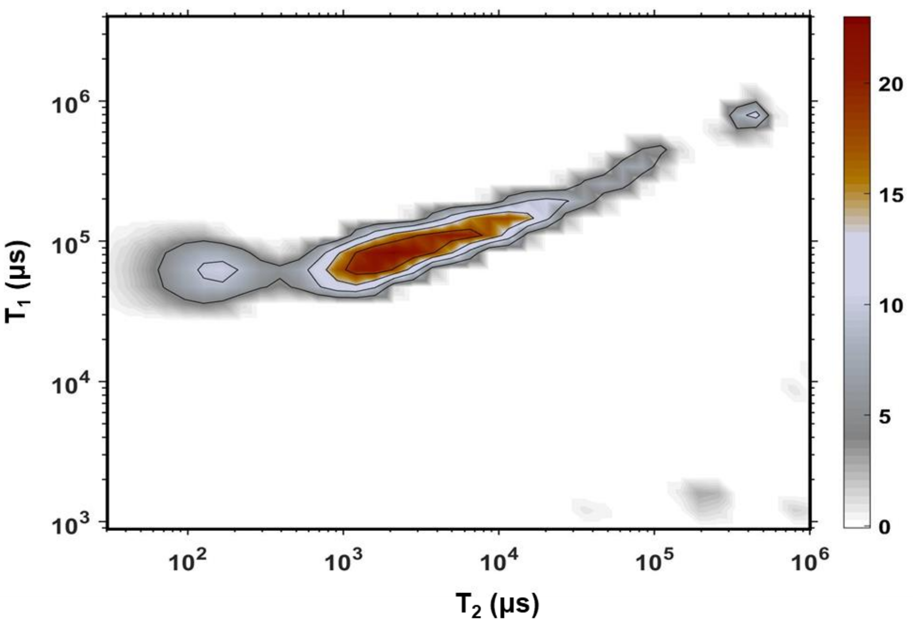

Figure 45. Contour plot of the static (no MAS) ^{1}H NMR T_1–T_2 spectrum of water in DWCNTs obtained with the help of a 2D Tikhonov inversion algorithm in 3.5 nm DWCNTs sample, at room temperature. On the basis of the T_2/T_1 ratios, three different water groups; bulk, interstitial and nanotube are resolved

Figure 46 shows the experimental data of an 1D inversion recovery experiment on DWCNTs in magnetic field 9:4 T, under static conditions (no MAS spinning). Using Tikhonov inversion we derive the relevant T_1 distribution which is shown in Figure 47. A weak peak at T_1~1:2s is observed, which corresponds to bulk water, and a second one at ~150ms, corresponding to nanotubular and interstitial water.

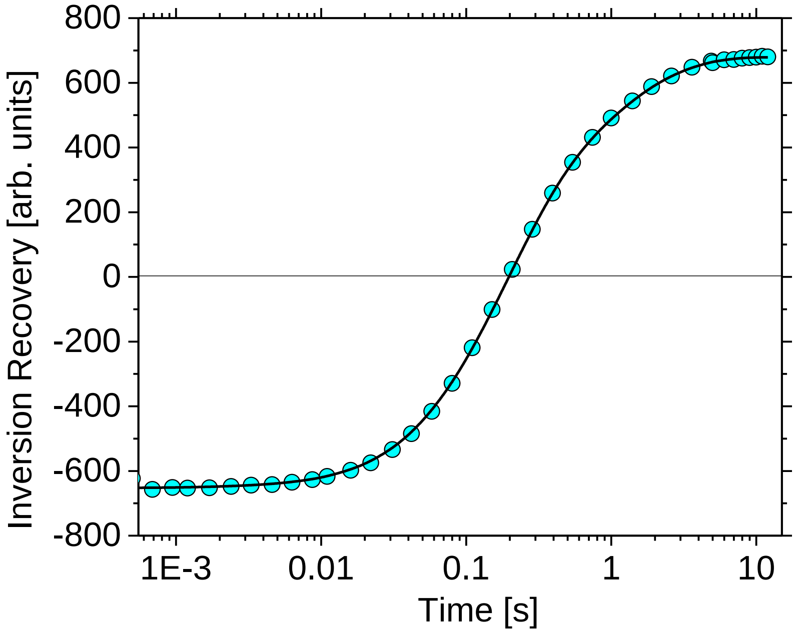

Figure 46. The Inversion Recovery curve as obtained by recording the signal intensity of the first spin-echo

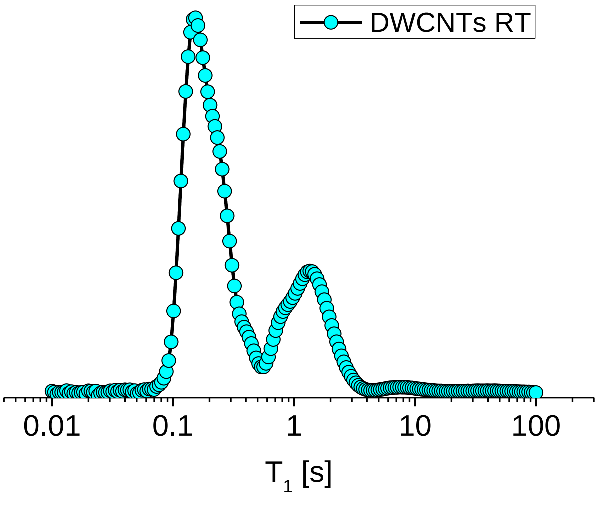

Figure 47. T_1 distribution by implementing 1D Tikhonov inversion algorithm on the relaxation data presented in Figure 46

Results are in full agreement with the high resolution ^1H MAS NMR T_1 measurements, shown in the following chapter.

3.2.3 MAS NMR T_1 relaxation analysis of water in CNTs

The ^{1}H magic angle spinning (MAS) NMR experiments were performed at room temperature on a Bruker (AVANCE 400) NMR spectrometer in Khalifa University in Abu Dhabi in 4 mm rotors and at spinning frequency of 12 kHz. Figure 48 shows the ^{1}H NMR T_1 distribution analysis of water in DWCNTs.

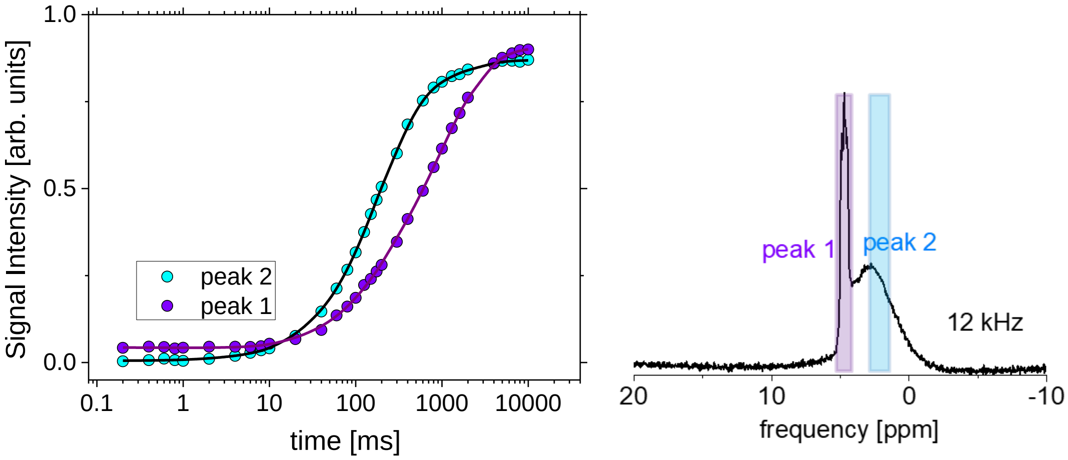

Figure 48. ^{1}H MAS NMR T_1 analysis of water in DWCNTs, at room temperature. The right panel shows the relevant ^{1}H MAS NMR spectrum at spinning frequency of 12 kHz. Peak 1 corresponds to bulk water and the broad peak 2 to nanotube/interstitial water. The main panel shows ^{1}H MAS NMR relaxation data from the shaded areas of the spectrum (saturation recovery curves). The solid lines are theoretical fits by using an 1D inversion algorithm.

The right panel of Figure 48 shows the relevant ^{1}H MAS NMR spectrum, obtained at a spinning rate of 12 kHz. Two peaks are observed, in agreement with the literature [43] a broad one at 2.73 ppm, which is attributed to water inside the CNTs (nanotubular water) and possibly to water in the space between the CNT bundles (interstitial water) and a relatively narrow peak at 4.9 ppm, very close to the frequency of bulk water, 4.8 ppm. The frequency shift of the first peak from the frequency of the bulk water may be assigned either to less number of hydrogen bonds per water molecules inside CNTs or to shielding from ring currents induced on the CNT walls.[43]

The main panel of Figure 48 shows the experimental relaxation data acquired separately on each of the two peaks, by using a saturation recovery technique.[44]. The T_1 analysis was then performed by implementing an 1D inversion algorithm on the relaxation data which is shown in the following Figure 49 [29].

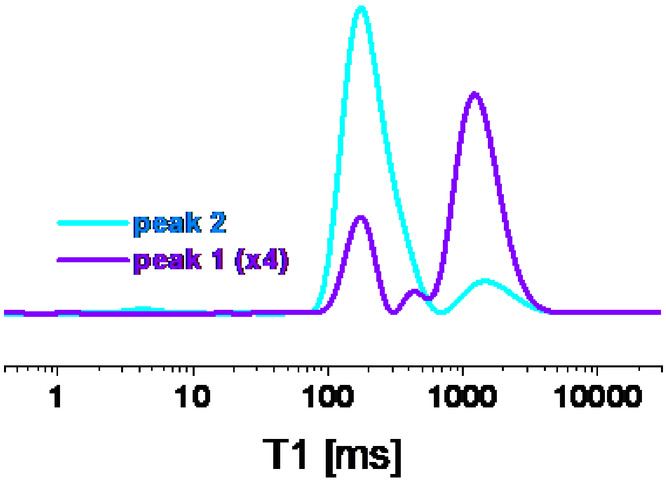

Figure 49. T_1 distributions of bulk and confined water, respectively, obtained by the inversion

It is observed that bulk water acquires T_1 distribution with peak at ≈1.2 s (violet line corresponding to the shaded area around 4.9 ppm), whereas the nanotube/interstitial water holds T_1 distribution with a peak at ≈0.15 s (cyan line corresponding to the shaded area around 2.73 ppm). Both values are sufficiently shorter than that of distilled bulk water $T_1 \approx 2$ s because of the unavoidable presence of paramagnetic impurities on the CNT walls. The weak violet T_1 peak at ≈0.15 s belongs to the tail of the nanotubular water NMR signal, which overlaps with the NMR signal of the bulk water. In addition, a second weak T_1 peak at ≈1 s is observed in the cyan line, which shows that a small component of the confined water acquires bulk water dynamics.

3.2.4 2D ^{1}H D - T_2 relaxation analysis of water in CNTs

^{1}H NMR 2D diffusion−relaxation 2D D−T_2 measurements were performed in the stray field of a 4.7 T Bruker superconductive magnet providing a 34.7 T/m constant magnetic field gradient at ^{1}H NMR frequency of 101.324MHz. The experiments were carried out by using a pulse sequence with more than 5000 pulses. The temperature was controlled by the ITC-5 temperature controller in a flow type Oxford cryostat as described above. The accuracy of the temperature was 0.1 K. A 30 min time window was allowed at each temperature before collecting data. NMR data were analyzed using a modified version of 2D non-negative Tikhonov regularization inversion algorithm code.

We applied two-dimensional ^{1}H NMR Diffusion Spin-Spin Relaxation Time D-T_2 in order to study water diffusion in CNTs. The D-T_2 pulse sequence is shown in Figure 50.

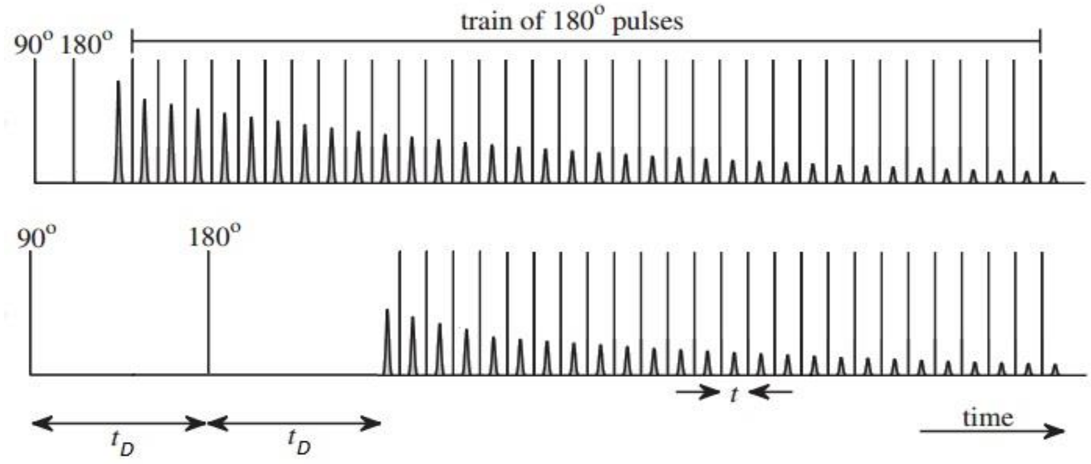

Figure 50. Upper panel: 2D D - T2 NMR pulse sequence used for the measurements .

It consists of a π/2 - t_D - π (Hahn echo) pulse sequence, followed by a train of 5000 pulses, generating a Carr- Purcell-Meiboom-Gill (CPMG) spin-echo decay (SED) train.[39, 40]. The π/2 pulse duration was set to 4μs and the CPMG interpulse time distance ‘’t’’ to 30μs. D-T_2 data were acquired with a series of 1D experiments. Data in the “direct” (T_2) dimension, were collected in a single shot, by recording simultaneously the intensity of all CPMG echoes. Data in the “indirect” dimension (D) were accumulated in successive experiments by incrementing t_D [29, 39] Overall, 30-40 experiments were performed with t_D values between 30μs to 1000μs in logarithmic scale, but practically the NMR signal for most experiments disappears after 300-350μs, due to the extremely strong magnetic field gradient. Figure 51 demonstrates the decrease of the intensity of CPMG echo trains at three different t_D values 50 μs 133 μs 236μs.

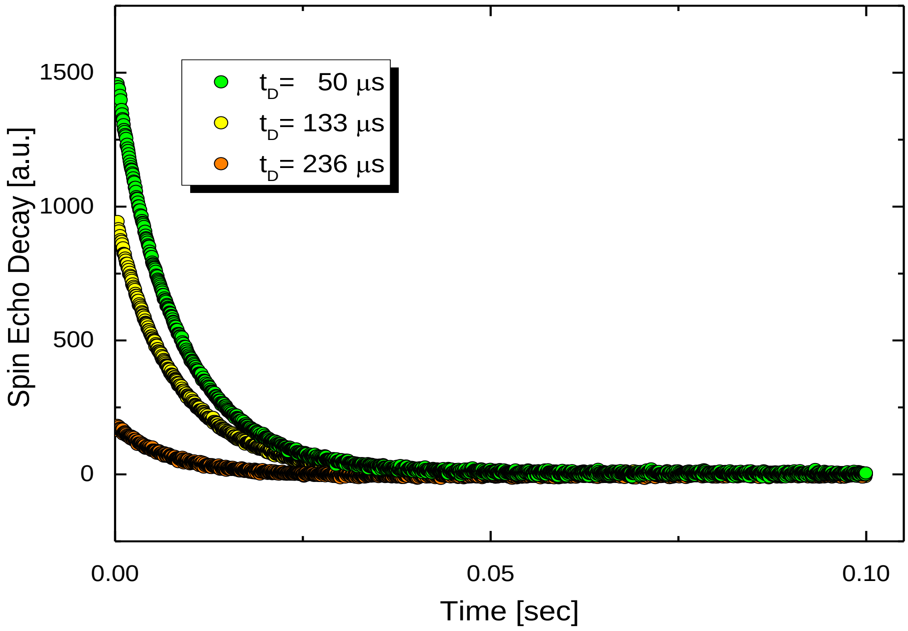

Figure 51. CPMG spin-echo decay of water in saturated SWCNTs, at room temperature, acquired at three different t_D values

Figure 52 shows the decrease of the signal intensity of the first spin-echo as a function of t_D. The solid line is the theoretical fit according to the relation [39, 40, 45, 46]

$$\mathbf{M = M_0 e^{\left(-\frac{2tD}{T_2}-\frac{2}{3}D\gamma^2 G^2 tD^3\right)}} \qquad \mathbf{(53)}$$

Where γ, D and G are ^{1}H gyromagnetic ratio, diffusion coefficient and magnetic field gradient strength, respectively.

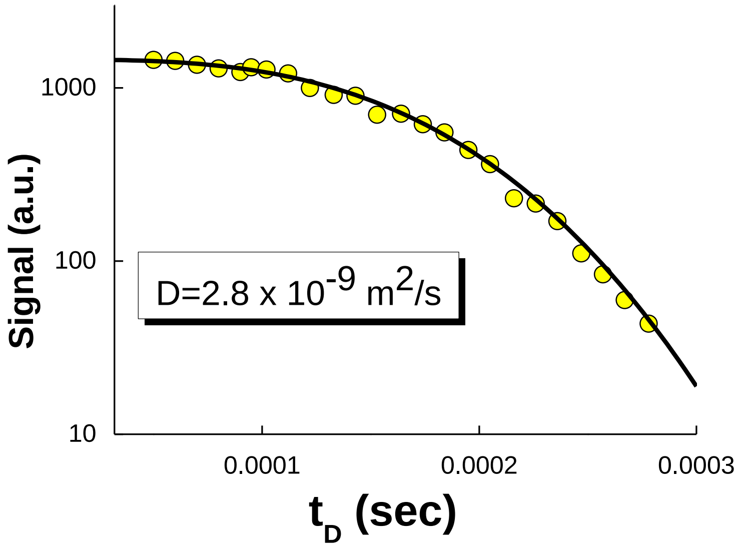

Figure 52. The signal intensity of the first spin-echo versus t_D and the solid line is the fit-line using Eq.1

In the presence of a broad distribution of diffusion processes and relaxation times, the D-T_2 signal intensity decays according to the relation [39, 40]

$$\frac{g(t_D{}',t)}{g(0,0)} = \iint_{-\infty}^{+\infty} \left(e^{-\frac{Dg^2\gamma^2(t_D{}')^3}{12}} e^{-\frac{t_D{}'}{T_2}} \right) \left(e^{-\frac{t}{T_2}} \right) f(D,T_2)\, dD\, dT_2$$

$$\frac{g(t_D,t)}{g(0,0)} = \iint_{-\infty}^{+\infty} \left(e^{-\frac{DG^2\gamma^2(t_D)^3}{12}} e^{-\frac{t_D}{T_2}} \right) \left(e^{-\frac{t}{T_2}} \right) f(D,T_2) dD dT_2 \qquad \textbf{(54)}$$

where D is the diffusion coefficient, T_2 is the transverse relaxation time, γ the proton gyromagnetic ratio and $t_D' = 2t_D$ where t_D is the variable delay between the pulses as shown in Figure 50 and f(D; T_2) is the distribution function of D and T_2. The first two exponential terms describe the signal decay of the first echo, in the diffusion part of the pulse sequence, due to both diffusion and transverse relaxation and the third exponential term describes the echo attenuation during the CPMG pulses due to the transverse relaxation. To determine $f(D,T_2)$ a change of variables $t_t = t + t_D{}'$ was applied. This allows separation of the D and T_2 axis, resulting in the following expression:

$$\frac{\mathbf{g(t_D,t)}}{\mathbf{g(0,0)}} = \iint_{-\infty}^{+\infty} \left(\mathbf{e}^{-\frac{\mathbf{DG^2\gamma^2(t_D)^3}}{\mathbf{12}}} \right) \left(\mathbf{e}^{-\frac{\mathbf{t_t}}{\mathbf{T_2}}} \right) \mathbf{f(D,T_2)\ dD\ dT_2} \tag{55}$$

Because of this transformation a few number of echoes at the beginning of the data array is not taken into consideration in the 2D inversion. In these experiments, the first 5 echoes out of 5000 echoes were excluded, which accounts for NMR signals with T_2 component shorter than ~0:2 ms to be invisible. D-T_2 (i.e. the f(D;T_2) distribution function) were obtained using a 2D non-negative Tikhonov regularization algorithm [27, 29] developed in Matlab as described in the theoretical part in Chapter 1.4

In case of diffusion in a bundle of randomly oriented one-dimensional (1D) nanochannels, Eq. 1, which describes unrestricted 3D diffusion, should be modified in order to take into account

(i) the 1D properties of the diffusion

(ii) the random orientation of the CNTs in respect to the external magnetic field gradient G.

This issue was addressed by Callaghan [47] who demonstrated that water diffusion in endosperm tissue of wheat grains, when simulated with diffusion in 1D randomly oriented array of capillaries, and averaged over all solid angles, gives spin-echo attenuation R_{1D} according to relation:

$$\boldsymbol{R_{1D}} = \int_0^1 \mathbf{exp}(-\boldsymbol{kDx^2})\,\boldsymbol{dx} \tag{56}$$

For diffusion in the stray field gradient G of the magnet k is given by

$$\boldsymbol{k} = \frac{2}{3}\boldsymbol{\gamma^2 G^2}\mathbf{t_D}^3 \tag{57}$$

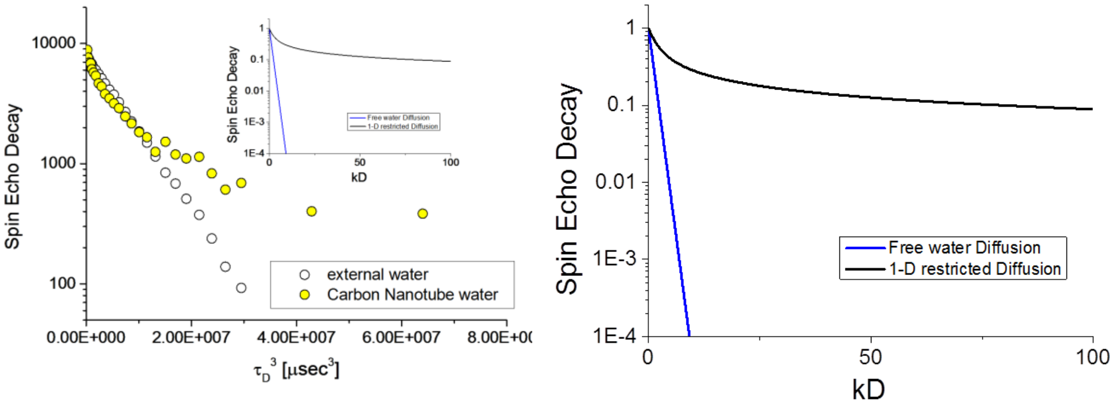

Figure 53. Decay of the first spin echo in the CPMG echo train of the external water (white circles) and the nanotube water (yellow circles) in DWCNTs as a function of t_D at RT. The blue and black lines in the inset are the theoretical curves acquired using Eq.53 for isotropic 3D and Eq.56 for restricted 1D diffusion, respectively

The difference in the spin-echo decay between unrestricted 3D diffusion and restricted 1D diffusion is excellently demonstrated in Figure 53, which shows the decay of the first CPMG echo as a function of t^3_D for external water (white circles) and nanotube water (yellow circles) in the case of partially water-saturated DWCNTs at room temperature. For reasons of comparison, the theoretical SED curves acquired by Equation 53 for bulk water diffusion (blue line) and Equation 56 for 1D restricted diffusion (black line), are shown in the inset of Figure 53.

The difference in the spin-echo decay between unrestricted 3D diffusion and restricted 1D diffusion is excellently demonstrated in Figure 53, which shows the decay of the first CPMG echo as a function of t3D for external water (white circles) and nanotube water (yellow circles) in the case of partially water-saturated DWCNTs at room temperature. For reasons of comparison, the theoretical SED curves acquired by Equation 53 for bulk water diffusion (blue line) and Equation 56. While the spin-echo attenuation for unrestricted 3D diffusion decreases linearly in the semi-log plot, the spin-echo intensity of 1D diffusion decreases with a successively declining slope. It is noticed that the inversion of the theoretical 1D spin-echo decay curve gives rise to an asymmetric distribution of D with a long tail towards the low D values Figure 54.

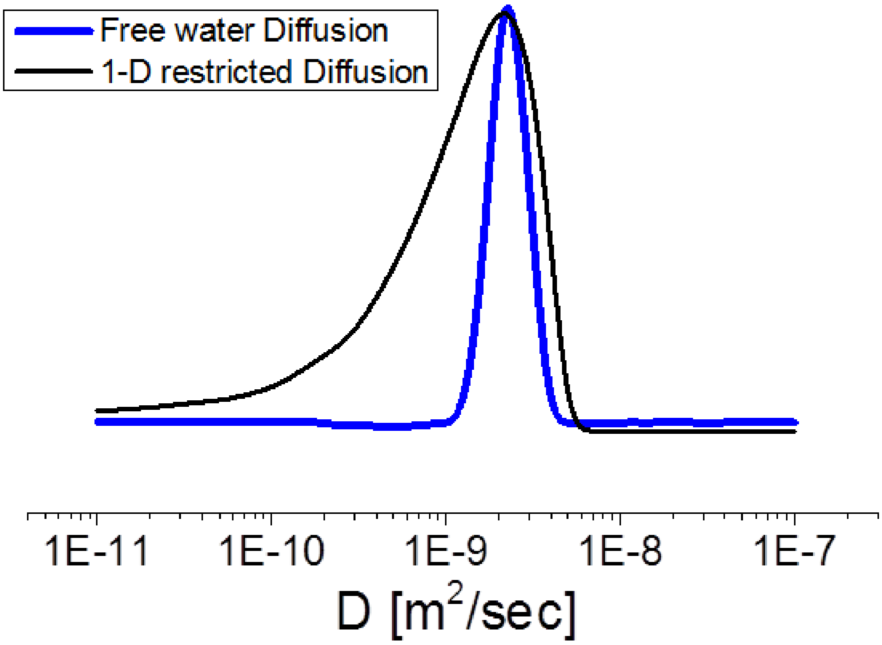

Figure 54. Self-diffusion coefficient D distribution simulations acquired by implementing a 1D Tikhonov regularization algorithm on the theoretical ^{1}H NMR Spin Echo decays of

This is the fingerprint of uniform 1D restricted diffusion in a set of randomly oriented nanochannels. SEDs of nanotube water in DWCNTs reveal unambiguously the profile of 1D restricted diffusion. Notably, at short times a very fast diffusing water component is observed as demonstrated by the very steep initial slope.

We applied static 2D (D−T$_2$) NMR experiments were performed in the stray field of a superconductive magnet of 4.7T with a constant magnetic field gradient G = 34.7 T/m. The conventional 1D NMR method for measuring water diffusion in a constant magnetic field gradient is to monitor the ^{1}H NMR spin-echo decay and then fitting the obtained decay curve to Eq. 1 where γ =26.7522 (10^7 rad/sT) is the gyromagnetic ratio for ^{1}H, and D the water self-diffusion coefficient ($D = 2.3 \times 10^{-9}$ m^2/s for bulk water at room temperature). The linearly exponential part of the decay corresponds to the ^{1}H NMR spin−spin T$_2$ relaxation, whereas the cubic exponential decay corresponds to ^{1}H NMR spin-echo dephasing in the magnetic field gradient G, in the presence of diffusional motion. In the case of nonuniform diffusion processes with multiple D values, diffusion is expressed with a distribution function f(D), which is obtained by implementing an appropriate 2D inversion algorithm [29] as explained previously. In this method 2D data are lexicographically transformed in a single column and subsequently inverted by applying a 1D Tikhonov inversion. The inverted data are presented as 1D vector, where the 2D spectrum is encrypted. Unwrapping this again in 2D provides the 2D D -T_2 contour plots.

It is extremely difficult with conventional 1D NMR diffusion experiments to disentangle water components with overlapping D coefficients. Consequently,^{1}H NMR studies of water diffusion inside CNTs have been reported in the literature but only presented weighted D values [48-50]. To overcome this obstacle, we take benefit of the fact that nanotube water, interstitial water, and bulk water acquire different T_2 values. Diffusion differences can be thus acquired by analyzing signals in different T_2 windows. This intricate assignment of diffusion differences in T_2-resolved water groups was excellently demonstrated in the past, through the ^{1}H NMR study of water mobility in hydrated collagen II. [51]

In Figure 55 we present the 2D D−T_2 contour plots of water in SWCNTs and DWCNTs at selected temperatures. Signals at different temperatures have been scaled accordingly to improve visualization. We observe two main peaks representing water inside the CNT channels (nanotube water) with very short T_2 at ≈0.5 ms and external water with long T_2 at ≈10−12 ms. The latter comprises interstitial water and bulk water because the effective T_2 of bulk water in the very strong magnetic field gradient in the stray field of the magnet is sufficiently shorter than that in a homogeneous magnetic field. [38]

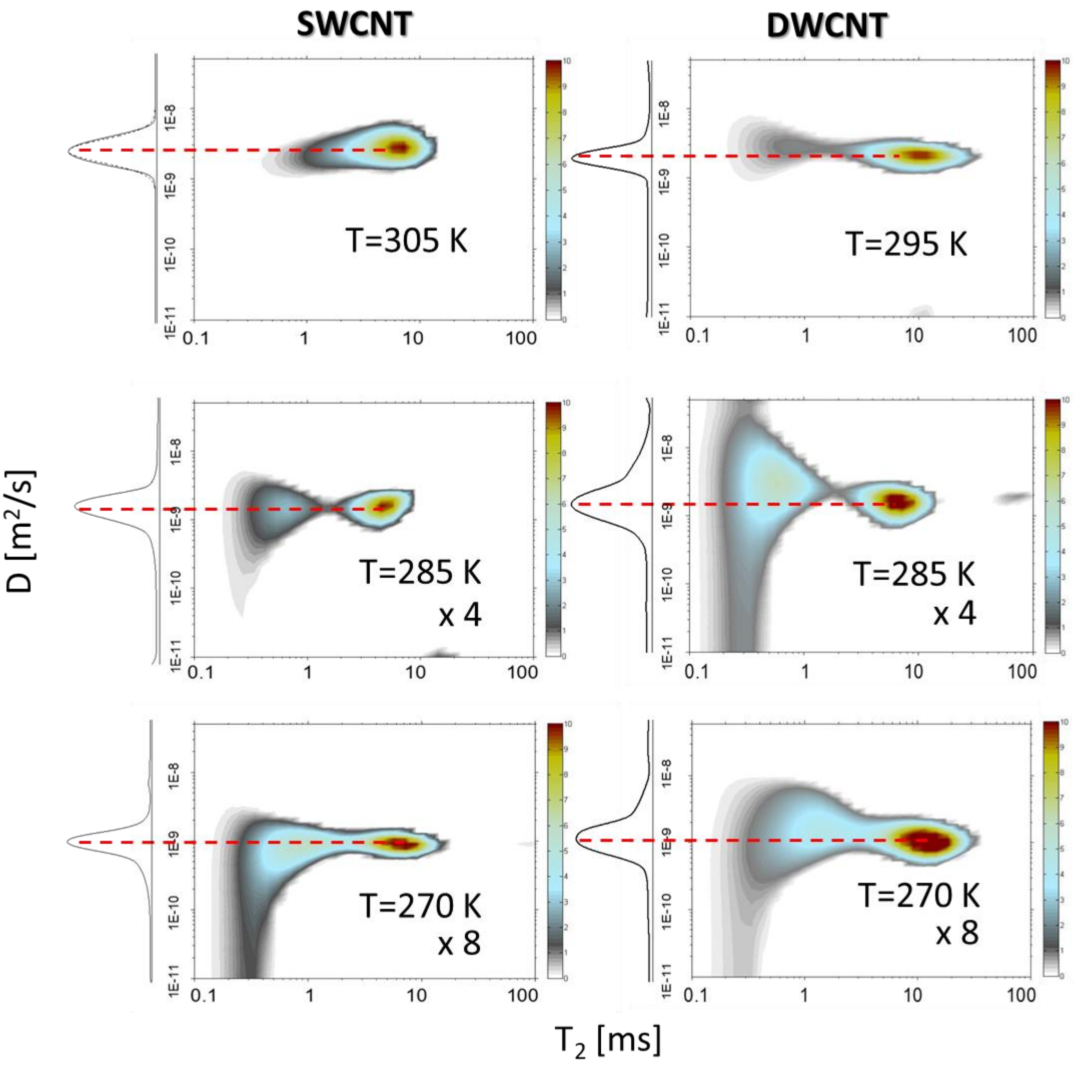

Figure 55. Contour plots of 1H NMR D−T$_2$ spectra of water in SWCNT (left panel) and DWCNT (right panel) at selected temperatures. Two main components are seen at each temperature, corresponding to nanotube water confined in the CNTs (low T$_2$ values) and interlayer and bulk water external to the CNTs (high T$_2$ values). Plots at the left side of the contour plots are the relevant D projections.

In both CNTs, external water attains D value ≈2.5 × 10^{-9}m^2/s at room temperature, which is close to that of bulk water. Upon lowering the temperature, water mobility decreases and the signal shifts to lower D values, as expected. At the same time, the intensity of the NMR signal from the external water decreases rapidly. It is noticed that part of the signal persists even at temperatures lower than the typical freezing point of bulk water (≈273 K), in agreement with previous ^{1}H MAS NMR measurements [43]. Therefore, the signal of the long T$_2$ water component, which remains at temperatures below the water freezing temperature, cannot be assigned to “bulk” water but rather to interstitial water confined in the space between the CNT bundles (confined water is known to freeze at T ≤273 K) [52].

3.2.5 T_2 Projection of D-T_2 contour plots

Figure 56 presents the T_2 projections of 2D D - T_2 spectra at selected temperatures for both SWCNT and DWCNT. Each projection mainly has two peaks; a short T_2 peak corresponding to the nanotube water (water in the interior of the CNTs) and a long T_2 component assigned to the external water. A rapid decrease of the signal intensity of the external water is observed by decreasing temperature, unveiling the presence of the nanotube water.

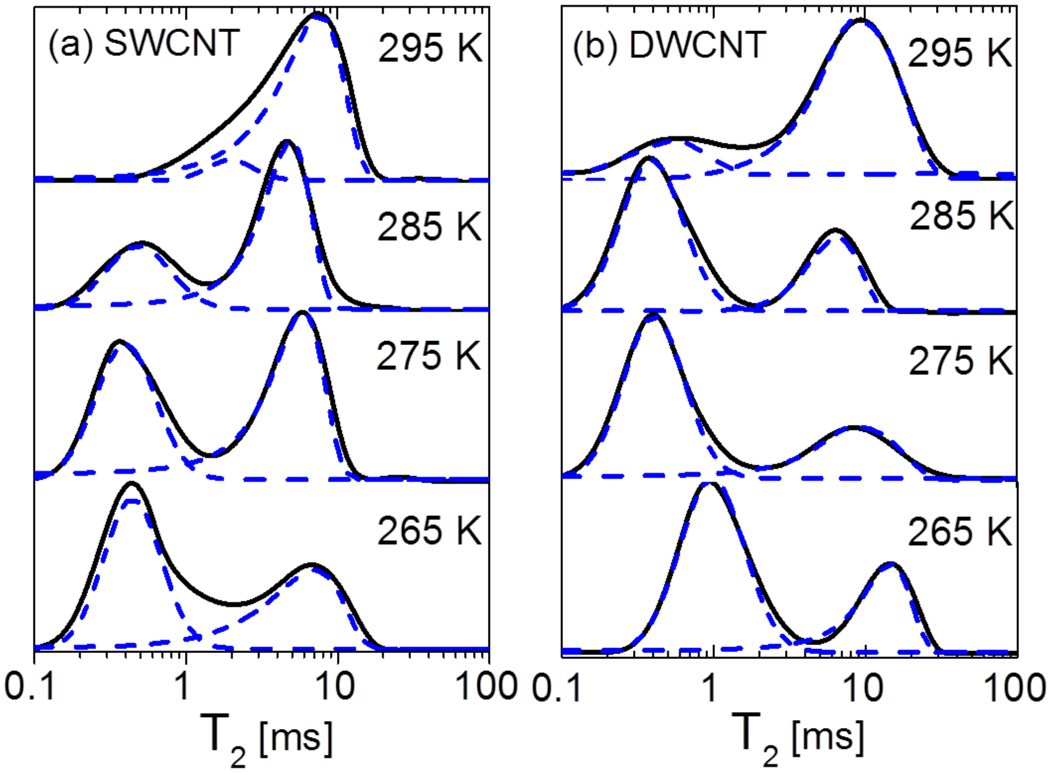

Figure 56. Water T_2 projections obtained from 2D D-T_2 contour plots in (a) SWCNTs and (b) DWCNTs. For clarity, the projections have been normalized. Fits (dashed lines) were performed with inversion of a stretched exponential spin echo decay and a log-norm distribution of T_2. The short and long T_2 components correspond to the nanotube and the interstitial water

As previously discussed, in the D - T_2 experiment the bulk water signal is included into the external water signal. It is very difficult to estimate the total amount of the bulk water in the sample, because only a sample-slice is observed in the strong permanent magnetic field gradient (as discussed in Figure 20 of Chapter 1.2.2). An estimate of the bulk water percentage in the "observed sample slice" from the NMR signal loss above and below the bulk water freezing temperature 273 K [53] is 0.7 of the total water content (ice-water is not observed because of the extremely short T_2).

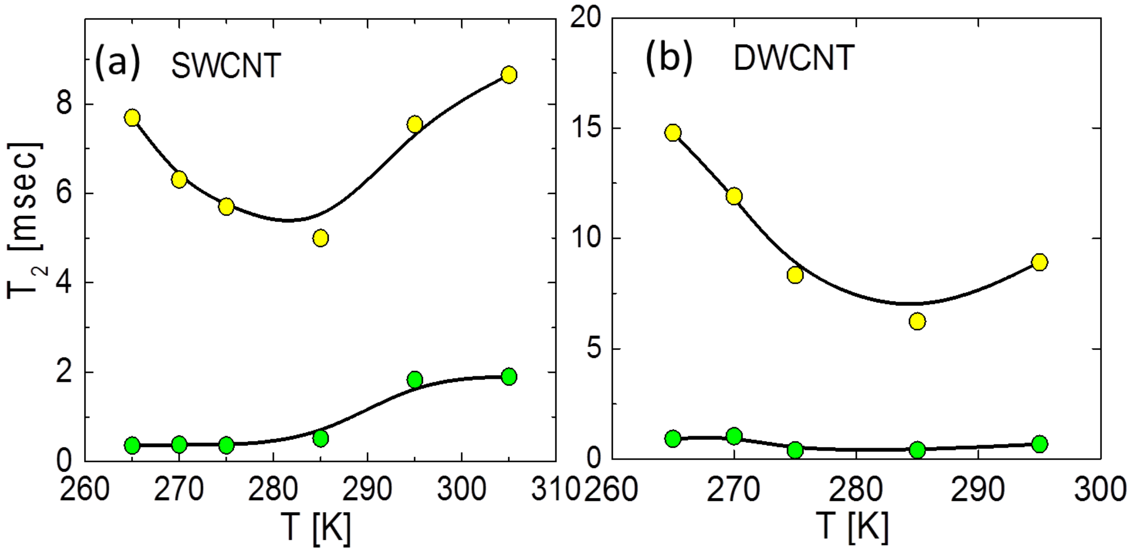

Figure 57. Temperature dependence of water-T_2 inside a) SWCNT and b) DWCNT samples. The green and cyan data-points are nanotube and interstitial water T_2 components, respectively.

Figure 57 shows the temperature dependence of the T_2 peak positions. Upon lowering temperature, the short T_2 component in SWCNT shifts to lower values, from ~2 ms at room temperature to ~0.2 ms at 265 K while remaining almost constant at ~0.5 ms in DWCNT. On the other hand, the long T_2 component shows an apparent local minimum at about 285 K for both samples. This might be related to the change of hydrophobicity, as discussed in a recent NMR publication,[54] but more work is required to examine this point.

3.2.6 D Projections of D-T_2 contour plots

The D projections shown at the left side of the contour plots in Figure 55 have a contribution from both interstitial and nanotube water signals; the diffusion peak from water inside the CNTs is distorted or even masked by the signal from the external water.

In order to uncover the water dynamics inside the CNT channels, the D projections of nanotube water from both SWCNTs and DWCNTs were separately calculated, as presented in Figure 58.

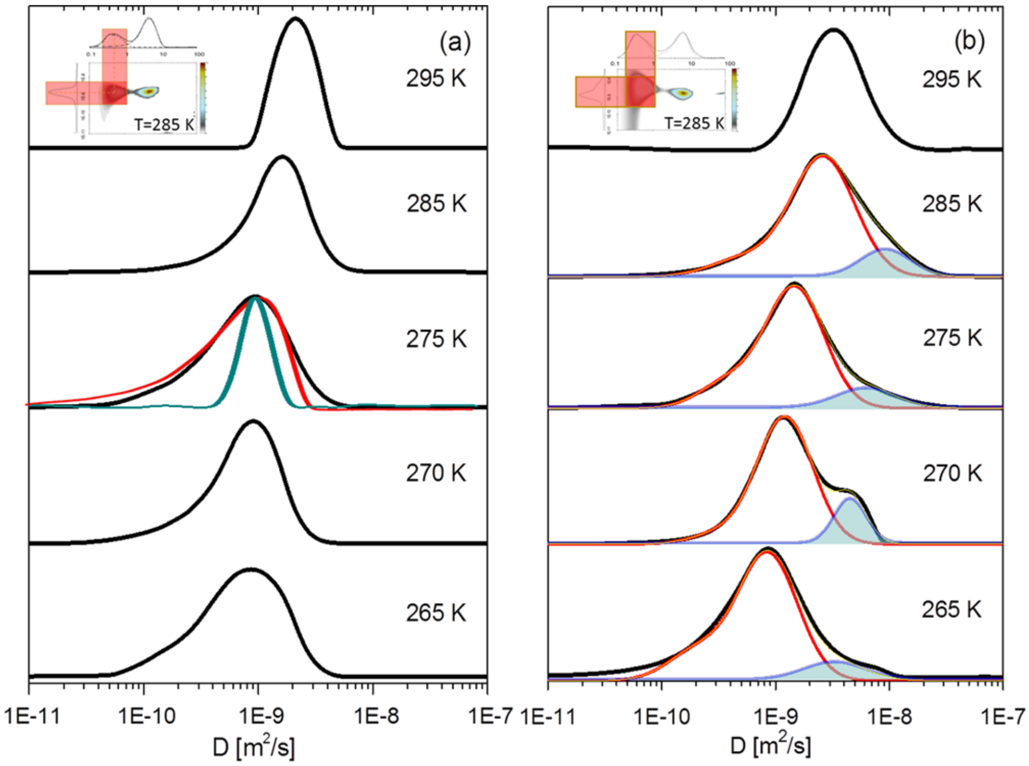

Figure 58. D projections of nanotube water in (a) SWCNTs and (b) DWCNTs. The insets show the selected areas of projection. For better visualization spectra are normalized to one. The red line at 275 K in SWCNT is the simulation curve of water diffusion in a bundle of randomly oriented CNTs. The dark cyan line is the relevant simulation curve of unrestricted bulk water diffusion. In DWCNTs, nanotube water shows stratified fast diffusion. The red line corresponds to shell water as in SWCNTs, whereas the cyan line represents the axial fast nanotube water component.

In the case of SWCNTs (left panel of the Figure 58a, at temperatures below 285 K, the D projection exhibits the characteristic low-D tail, encountered with 1D diffusion in randomly oriented CNTs [47]. This is manifested with the theoretical red line details are provided as follows, which simulates accurately the experimental spectrum at 275 K.

Short T_2 values might distort the self-diffusion coefficient D-distribution [55] This is so as short T_2 might enhance the spin echo decay at long interpulse time delays, giving rise to illusively high D-values (tails in the direction of the high D-values). In order to examine the reliability of the inversion algorithm used in this work at very short T_2 values, we have compared the D-profiles of experimental and simulated D - T_2 data, by using simulated data with T_2 values similar to the experimental ones, but only a single diffusion coefficient D value. All other used inversion parameters were kept exactly the same for both simulated and experimental data. Figure 59 presents the results of this comparison for the cases of (i) fully hydrated DWCNTs at 285 K and (ii) partially hydrated DWCNTs at 293K.

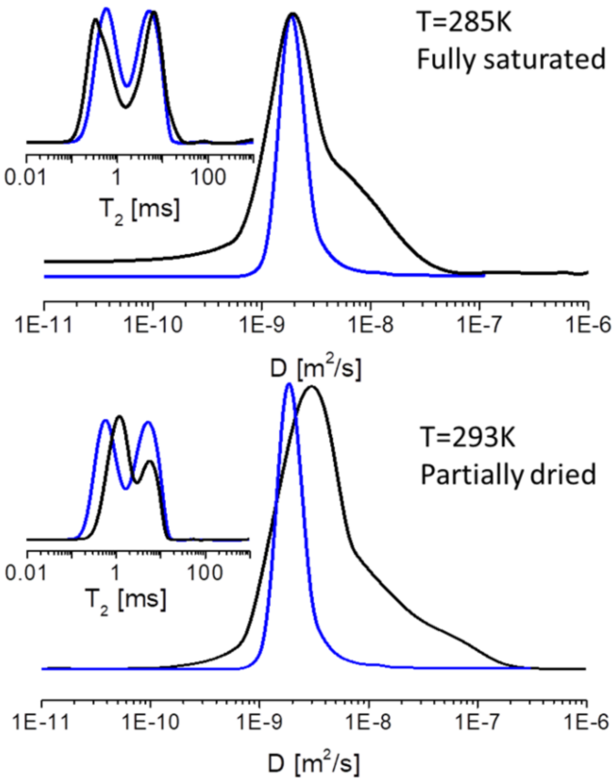

Figure 59. Comparison of the self-diffusion coefficient D distribution of water in (i) fully hydrated DWCNTs at 285K (black line in the upper panel) and (ii) partially hydrated DWCNTs at 293K (black line in the lower panel), as obtained from D-T_2 experiments with simulated data (blue lines). It is noticed that simulated data acquire similar T_2 distribution with the experimental data but only one D-value, D = 1:8 x 10^{-9} m^2/sec.

Despite the very short T_2 value, the simulated data are shown to acquire only a slight broadening of the D- distribution, which is an order of magnitude narrower than that of the experimental spectra. This provides straightforward evidence that the short T_2 values in the very strong permanent magnetic field gradient G = 34:7 T/m used in this work do not create any significant artifact in the D-T_2 spectra. In addition the proposed method acquires reliable information even in the case where the external water masks almost completely the D-projection of the nanotube water, as shown in Figure 60.

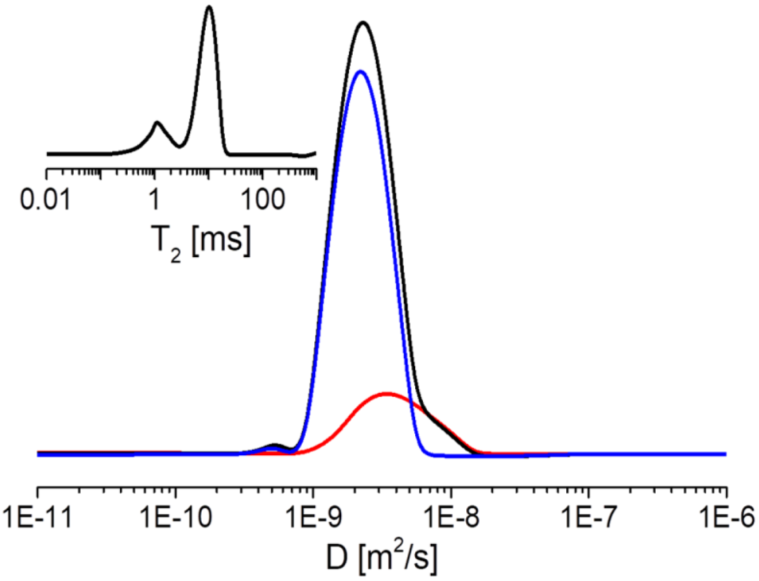

Figure 60. The D-projection of water in fully water hydrated DWCNTs at room temperature, as obtained from the relevant D-T_2 spectrum. The blue/red lines correspond to the individual D-projections of the external/nanotube water with the high (short) T_2 values

Furthermore, it is noticed that the validity of our experimental analysis is in agreement with recent results by Kausik et al.,[55] on the sensitivity of D-T_2 measurements. They introduced two parameters α and C (equations (3) and (5) in their article), which measure the relative strength of diffusion/relaxation and what they call diffusion contrast. According to their analysis the inversion of the D-T_2 data is reliable if $\alpha \geq 1$ and C has values between 0-1, with the 1 being the ideal value. In our study, for the short D-T_2 component α= 1:3 and C has intermediate values reaching a maximum value of 0:7.

Back in the D-projections the fitting of the curve to the 1D model with a unique D value is consistent with the confinement of water molecules in a randomly oriented array of CNT tubes with short (nanometer scale) inner radial dimension but long (micrometer scale) axial dimension. Most importantly, the restricted diffusion in SWCNTs acquires D values close to that of free water, in agreement with MD in the literature [56]. In DWCNTs Figure 58b, the D distribution of water inside the CNTs attains a more intriguing picture. At T = 285 K, the diffusion profile of the nanotube water can be resolved in two components having different dynamics with D peaks centered at $\approx 2.58\times10^{-9}$ and 9.60×10^{-9} m^2/s. This corroborates with neutron scattering experiments, which show the presence of two different water groups, that is, a shell of water close to the CNT walls and a chain-water at the center of the CNTs [57]. The stratified arrangement of water in the DWCNTs can be explained by considering

(i) the larger inner size of 3.5 nm in comparison to the SWCNT

(ii) the repulsive Coulomb forces [58] between next neighboring oxygen atoms, which become important when water is squeezed into the hydrophobic CNTs

According to MD, depending on the CNTs diameter, the free energy of the nanotube water molecules shows a number of minima in the radial direction. In this energy configuration, water molecules reside at the local minima, giving rise to a stratified water arrangement [56, 59-61]. At low temperatures, the radial exchange of water molecules among different water shells is prohibited by the energy barrier, and water molecules diffuse preferentially in the axial than in the radial direction [56]. In this picture, water inside DWCNTs is organized into shell and chain-water, the latter showing astonishing diffusion enhancement, ≈8−9 times higher than that of bulk water. This behavior was not observed in SWCNTs because of the small confinement size of ≈1 nm. It is noticed that at elevated temperatures liquefaction and fast exchange of water molecules between the two shells becomes possible. This explains the merging of the two diffusion peaks into a single one at 295 K in the DWCNTs, which is observed in Figure 58b. Evidently, at this temperature water molecules in the two different tubular shells overcome the energy barrier and fast exchange takes place in the radial direction. This effect is similar to the high-temperature ice-water shell melting, observed in SWCNTs with neutron scattering experiments [57]. We notice that the diffusion of water molecules is further enhanced upon decreasing the water content in the CNT samples, in agreement with the theoretical predictions [37].

In the materials section we showed (Figure 40) the D-distribution profile of water, at room temperature, in SWCNT as well as in three DWCNTs samples with different water contents as shown here in Figure 61 on the left panel. Results show that by reducing water, a very broad distribution of D unveils, which decomposes into a very broad fast diffusing component belonging to the nanotube water and a second one belonging to the external water.

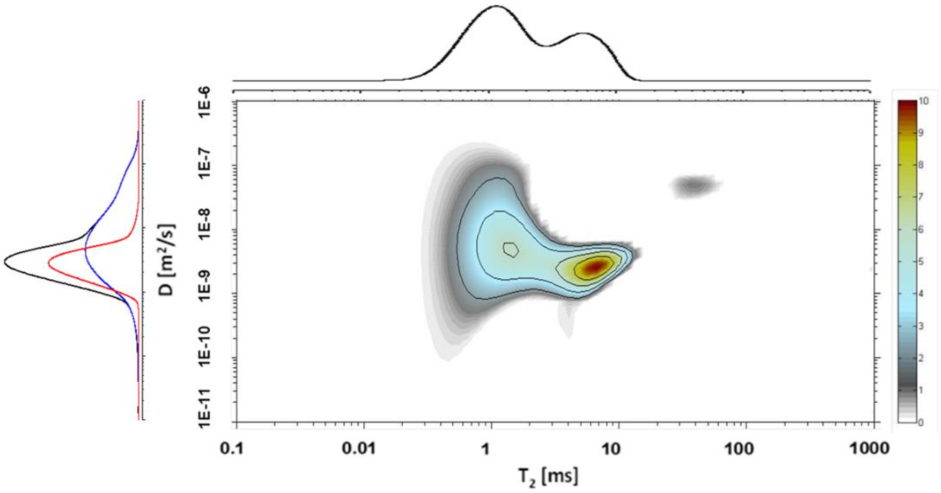

Figure 61. **^{1}H NMR D–T$_2$ spectrum of DWCNTs with intermediate water content corresponding to the black line in panel. Left panel D-profile of water in SWCNTs and DWCNTs, at room temperature at different water content (Figure 40). Upper panel: T$_2$ projection obtained from 2D D-T$_2$ contour plot of DWCNTs**

To summarize the results, a schematic representation of the water groups in SWCNTs and DWCNTs is shown in Figure 62. According to the NMR experiments, in SWCNT with an inner diameter of ≈1.2 nm, only a single shell nanotube water component was detected (represented by the red spheres in the figure), in agreement with the MD [59, 60]. Water molecules of this group have self-diffusion coefficients (red squares in the figure) comparable to that of bulk water. Remarkably, in DWCNTs with an inner diameter of ≈3.5 nm, in addition to the shell water, a second water component is observed (cyan spheres in the figure), with sufficiently higher D values in comparison to those of bulk water. The green lines in Figure 62 represent water profiles according to MD [59, 62] These findings confirm theoretical calculations, which depending on the CNT-size, predict that water inside CNTs diffuses in the shape of hollowed nanotubular clusters with an ultrafast mechanism [37, 63] The lower D values of the outermost axial water component in both SWCNTs and DWCNTs may be attributed to “friction” from the interaction of water molecules with defects and oxygen moieties, which are unavoidably present on the CNT walls.

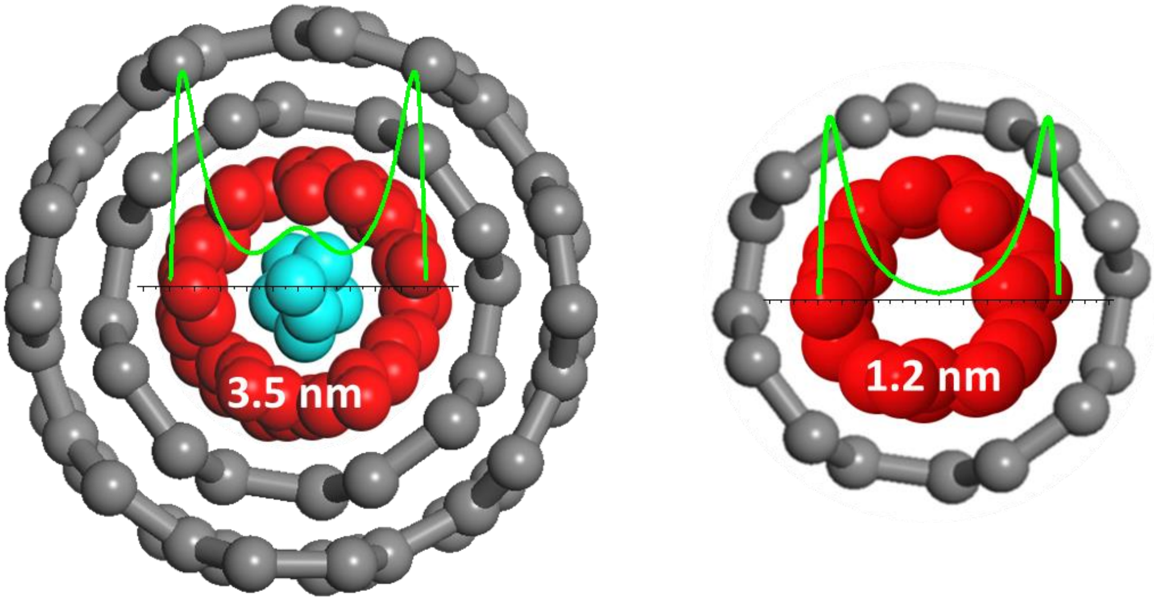

Figure 62. Schematic presentation of water diffusion in SWCNTs (left panel) and DWCNTs (right panel). Water structure has been sketched by combining D−T$_2$ NMR experimental data with recent MD[59, 62] The green peaks in panels are sketches of the relevant water density.

To further enlighten the dynamics of the nanotube water in both CNTs, the inverse of the self-diffusion coefficient, 1/D versus 1000/T is presented in Figure 63. For comparison, 1/D of bulk water (black circles) is shown in the same figure. The blue line is the theoretical simulation of an ideal “strong” liquid with 1/D exhibiting Arrhenius temperature dependence

$$\frac{1}{D} \propto \exp\left(\frac{U}{K_B T}\right) \quad (58)$$

Bulk water is observed to deviate significantly from the Arrhenius behavior; within Angell’s concept of fragility [20], bulk water is considered to be fragile [64, 65], that is, it slows down gradually upon cooling and freezes rapidly near the water glass transition temperature at $T_g \approx 140$ K. The black line is the theoretical fit to the empirical formula

$$\frac{1}{D} = \frac{1}{D}\left(\frac{T-T_s}{T_s}\right)^{\gamma} \quad (59)$$

which is widely used in the literature to fit the non-Arrhenius temperature dependence of the water transport properties [20]. T_s in this formula is the thermodynamic limit where transport properties become zero, and the exponent γ provides a measure of the growth of the hydrogen bonding by cooling.

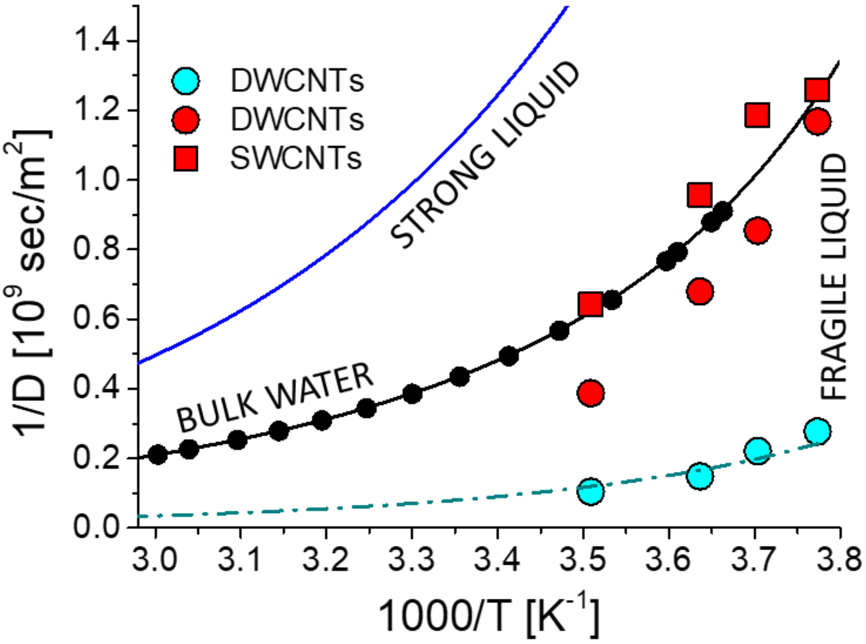

Figure 63. Inverse of the experimental self-diffusion coefficient 1/D as a function of 1000/T. The blue line shows the temperature dependence of an ideal "strong" liquid following Arrhenius law. The solid black and the dashed cyan lines are theoretical fits as described in the text

Experimental data are nicely fitted with γ ≈ 2 and T_S ≈ 215 K, in agreement with previous reported values [66]. In the case of SWCNTs, the 1/D values of nanotube water matches well with those of bulk water. However, the 1/D values of the central water component in the DWCNTs (cyan circles in Figure 63) deviate strongly from those of bulk water, acquiring low values which vary slowly by decreasing temperature. This indicates that the central nanotubular water component is more fragile, and "resists" the formation of hydrogen bonds upon cooling [21, 59]. It is possible that at room temperature, liquid islands in this fragile water component are responsible for the weak "liquid-like" T_1 component at ≈1.2 s, which is observed in Figure 49. These findings provide a different viewpoint to the way that water is organized inside the CNTs. It is generally accepted that water mobility in CNTs depends strongly on the number of hydrogen bonds per water molecule and the inner diameter of the CNTs [61, 62]. Specifically, MD have shown that the number of hydrogen bonds per water molecule is ≈3.7 at the center of the nanotubes (the same as bulk water) and ≈2 close to the CNT walls, which gives rise to enhanced water mobility close to the hydrophobic CNT walls [61, 62, 67]. This is in contrast to the results presented here, which show that water diffusion at the center of DWCNTs is sufficiently faster than diffusion near the walls. The observed reduced mobility close to the walls might be related to “friction” caused by the interaction of the water molecules with defects and oxygen moieties, which are unavoidably present on the CNT walls. Furthermore, our experimental results are in agreement with viscosity measurements [68], which show that shear viscosity of water confined in CNTs is about an order of magnitude lower than that in bulk water and increases nonlinearly with the CNT diameter, while enhanced diffusion of water inside CNTs appears only for diameters higher than 4 nm.

3.2.7 Conclusions

In conclusion, herein, we report the first experimental measurement of fast water diffusion in SWCNTs and DWCNTs with the help of 2D ^{1}H NMR ($D-T_2$) and 2D ^{1}H NMR (T_1-T_2) methods. Unlike previous works where diffusion of water in CNTs at the molecular level has been monitored almost solely with MDS, here we demonstrate a fast and scalable method to acquire experimentally the diffusion of water and other fluids in nanotubular channels at nanoscale resolution. With this method, water in DWCNTs is shown to have a stratified diffusion profile, revealing an axial component with extraordinary high D values, a phenomenon not present in SWCNTs. However, at room temperature, fast exchange of water molecules in fully saturated DWCNTs appears to establish a uniform diffusion mechanism. Interestingly, in partially saturated DWCNTs, an anomalously high water diffusion mechanism unveils, which shows the complexity of water diffusion into hydrophobic nanochannels. The discovery of stratified fast diffusion in CNTs is new experimental evidence, which confirms MDS predictions, with important impacts on our current understanding of water flow through hydrophobic nanochannels and nanostructured membranes [69, 70]. It is also expected to be very helpful in the efforts to understand fluidic properties through extremely narrow pores, with the aim to develop high-readout single-molecule detectors [71, 72] and regulate the cellular traffic of important biological solutes[73].

3.3 The Peculiar Size Dependent Ultrafast Water Diffusion in Carbon Nanotubes: A Combined 2D NMR Diffusion-Relaxation (D-T_2) and Molecular Dynamics Simulations Study

The study of water confinement in Carbon Nanotubes (CNTs) attracted great interdisciplinary interest as conduit for understanding nanofluidic properties in a variety of nanoporous systems aiming to novel applications, such as water treatment technologies [74], drug delivery [75, 76], intracellular solute transport control[77], and energy applications [78, 79]. Several experimental and theoretical methods – mostly Molecular Dynamics (MD) simulations [75, 80, 81] have been utilized to investigate the way water molecules are confined inside CNTs. A major outcome of the MD studies is that water molecules in the nanotubular CNT space tend to stratify in coaxial tubular sheets [56, 59, 80]. Furthermore, water confined in the CNTs is predicted to diffuse faster than bulk water, in a certain range of CNT diameters[61, 80, 82]. This fast water motion has been explained by several authors as due to H-bond modifications in the hydrophobic nanochannels, or due to geometrical effects and curvature induced incommensurability between the water and the CNT walls [80].

From the experimental point of view, a great number of methods, such as infrared spectroscopy [83], Raman spectroscopy [84, 85], Thermogravimetric analysis [84, 86], Transmission Electron Microscopy (TEM) [67, 87-90], X-ray Compton scattering [91, 92] [22, 23], and Nuclear Magnetic Resonance (NMR) [24-27] have been widely used in the study of molecular confinement and transport through the CNT channels [50]. However, until now there is scarce experimental evidence at molecular scale, regarding the way that water organizes and diffuses inside the CNTs.

NMR is considered an important noninvasive tool with atomic scale resolution for studying water-surface and nano-confined water systems. Standard NMR experiments typically include longitudinal T_1, transverse T_2 relaxation times, self-diffusion coefficient D, and line-shape measurements. In a recent survey [50] of NMR studies on the water dynamics in CNTs, it is revealed that the majority of the published work [43, 93-96] is focused on ^{1}H-water NMR-lineshape versus temperature in order to establish the freezing point of the confined water. However, any change in the water structure and dynamics induced by the nano-confinement is expected to be also reflected in the ^{1}H NMR T_1, T_2 and D values of the water molecules. Such measurements for water-in CNTs have been rarely published [49, 54].

In this work, we utilize two-dimensional ^{1}H NMR diffusion-relaxation correlation spectroscopy (D-T_2) to study water confinement in CNTs of various diameters as a function of temperature. In a previous work [97] we reported the diffusion enhancement of water inside 3.5 nm double walled CNTs. Herein we present a new NMR study of CNT samples of different diameters (1.1 nm-6.0 nm) and temperatures (265K-305K) to investigate the influence of the nanoconfinement size on water dynamics. In addition, we have carried out MD simulations on the same systems in order to compare the theoretical with the experimental results. Notably, in the CNTs diameter range 3.0 nm -4.5 nm, water is shown to split into coaxial tubular sheets (WTS), with the central one acquiring an order of magnitude higher self-diffusion coefficient D compared to the outer WTS close to the CNT wall. This result is not foreseen by any MD calculations performed until now. Even more, water molecules along the CNTs axis show remarkable deviation from the Arrhenius temperature dependence; a very fragile, almost liquid-like axial water component even at very low temperatures is formed, with fragility sufficiently higher than that of the bulk water, which depends strongly on the CNTs size.

Purified carbon nanotubes (SWCNT, DWCNT, and MWCNT) were purchased from SES research, USA. The inner diameter of the CNTs used in this work was ~1.1 nm for the SWCNT, ~3.5 nm for the DWCNT and 4.5 nm for the MWCNT. Additionally, further MWCNT samples were purchased from Nanocs, USA with inner diameters 3.0, 5.0, 5.5, and 6.0 nm. The length of the tubes in all the CNTs used in this work was from 15μm to 20 μm and all the CNTs were open ended as provided by the manufacturer. The samples were characterized using TEM-FEI Tecnai G20 with a 0.11 nm point to point resolution and found consistent with manufacturer's specifications as shown in the Materials section in the TEM images (Figure 38). The CNT powder was used with no further treatment and doubly distilled water was used in all the measurements.

For the two dimensional ^{1}H NMR diffusion-relaxation 2D D-T_2 measurement, the fringe field of a 4.7 T Bruker magnet which provides a 34.7 T/m constant field gradient with ^{1}H NMR frequency of 101.324MHz was used and for the 2D T_1-T_2 experiment a 9.4T Oxford Magnet with ^{1}H NMR frequency of 398.822 MHz was used as described in previous Chapters.

3.3.1 Molecular Dynamics Simulations

Molecular dynamics simulations were used to investigate the diffusion of water inside single walled carbon nanotubes. Different systems were simulated for CNT's with different diameters. Each system consists of a nanotube of length 20nm immersed in a water bath. The nanotubes studied are the armchairs (4, 4), (8, 8), (15, 15), (18, 18), (22, 22), (26, 26), (37, 37), and (73, 73) of diameters 0.55 nm, 1.10 nm, 2.06 nm, 2.47 nm, 3.02 nm, 3.57 nm, 5.08 nm, and 10.02 nm correspondingly. The molecular dynamics simulations were implemented using NAMD [98]. Water molecules was represented using the Simple Point Charge/Extended (SPC/E) model [99]. The non-bonded interactions between carbon atoms were modeled using Lennard-Jones (LJ) potential with the parameters (ε=0.069kcal/mol, r_{min}=3.805 Å) given by Werder et al [100]. The positions of the carbon atoms were held fixed throughout the simulations. The systems were kept at the same temperature of 300 K using Langevin Thermostat. In addition, the pressure was maintained at 1.0 atm using Nosé-Hoover Langevin piston with a period of 100 fs and a damping time scale of 50 fs. The simulations were performed using periodic boundary conditions in which electrostatic interactions were calculated using Particle Mesh Ewald (PME). The simulation integration time step was 2.0 fs. Bonded interactions were calculated every time step while non-bonded interaction was calculated every two steps with a cut-off of 12 Å and switching function of 10 Å.

All simulated systems were minimized for 10,000 steps and then gradually heated to the target temperature of 300K. Each system was then equilibrated at 300K for 50,000 steps (100 ps) before the production runs. The production simulations were run for a total time of 50 ns. The system configuration was saved every 500 steps (1.0 ps) for analysis. The water density profile was calculated for each simulated system inside the CNTs in order to elucidate the structure. The self-diffusion coefficient was determined using the mean squared displacement function (MSD) in the axial direction. MSD was calculated over a time interval of 1.0 ns at a sampling rate of 1 ps. MSD was then averaged over 50 such time intervals. The interval length, 1.0 ns, was chosen carefully to give water molecule enough time inside the carbon nanotube before exiting. The long time MSD was then fit to the formula, $\mathrm{MSD}\ t_{\rightarrow\infty 0}=2Dt$, to obtain the value of the diffusion coefficient, D. The diffusion coefficients were calculated for all of the water inside the CNT and for all the components obtained from the density profile.

The water structure inside CNTs varies upon increasing the CNTs diameter; it forms a 1D chain of water molecules in ultranarrow single walled CNTs (d<1nm), and it is organized into coaxial WTS as the CNTs diameter increases. Figure 64, shows three MD simulation snapshots of the water configuration at room temperature inside CNTs with diameters 1.1nm, 3.0nm, and 5.0nm.

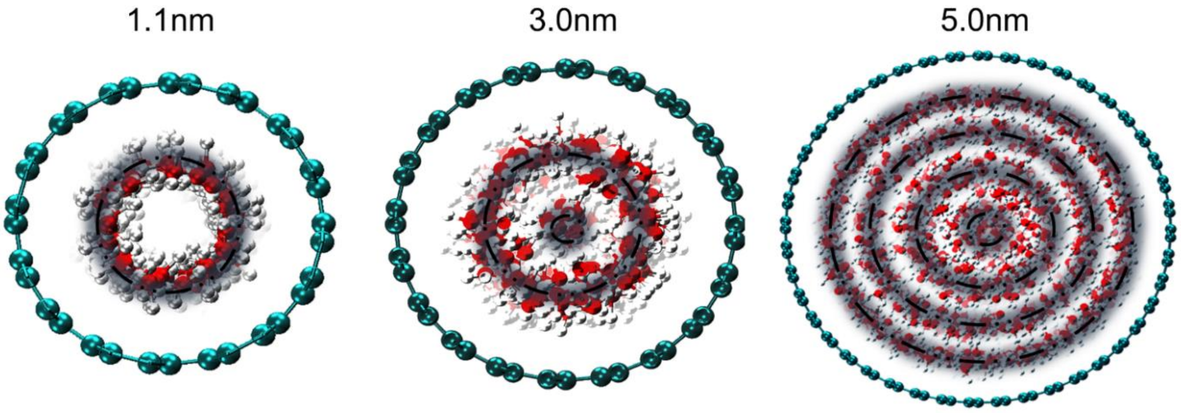

Figure 64. Snapshots from MD simulations of water molecules arrangements inside CNT nanotubes of different sizes (green: carbon atoms of the CNT wall, red: Oxygen atoms white: Hydrogen atoms and black shaded-circles represent different water layers).

In all three cases, water molecules inside the CNT channels are shown to arrange in concentric WTS (black circles in the snapshot), in agreement with previous publications (for example Alexiadis et al.[56] and references therein).

The number of WTS that can be accommodated inside the CNT channels depends on the size and on the Oxygen-Oxygen as well as Oxygen-Carbon interactions [56]. It is furthermore observed that the stratified water arrangement into WTS becomes denser by increasing the CNT size and gradually the dynamics of water molecules approach that of bulk water [56].

3.3.2 NMR Experiments

In order to verify experimentally the role of the CNTs diameter on the water structure and dynamics, we conducted 2D ^{1}H NMR D-T_2 measurements of water in various CNT sizes, ranging from 1.1 nm to 6.0 nm, and in the temperature range 265K to 305K. Here, T_2 acts as filter in resolving the nanotube water from the external water in saturated CNT samples. The way that T_2 filters out the external water component is clearly demonstrated in the 2D ^{1}H NMR T_1-T_2 correlation spectrum of Figure 45 from the previous experiments for DWCNTs. [101]

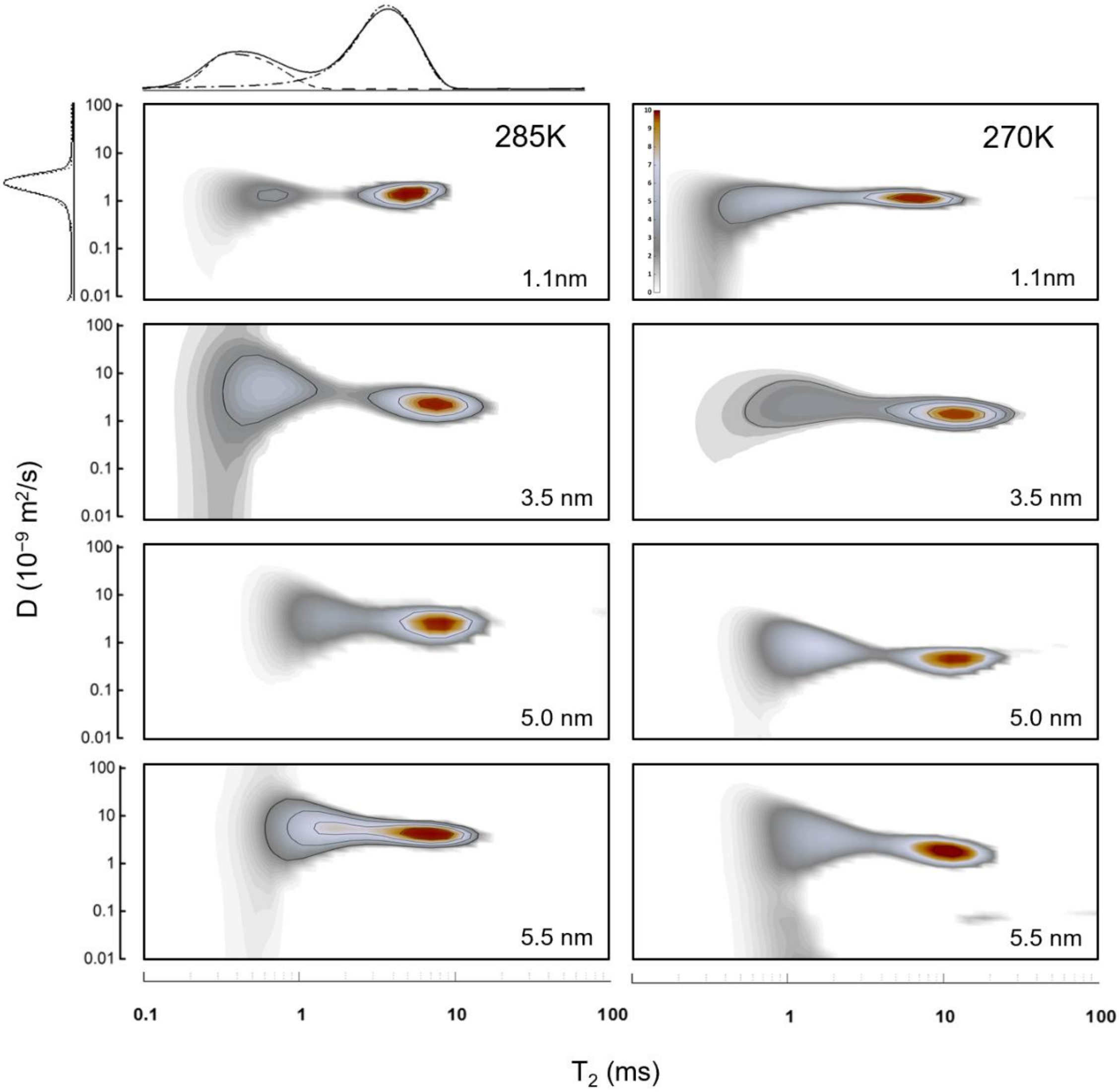

Figure 65. 2D ^{1}H NMR D- T_2 contour-plots of water inside CNT of sizes 1.1nm, 3.5nm, 5.0nm and 5.5nm, at selected temperatures (270 K and 285 K). Two main T_2 peaks are observed, corresponding to two

different water reservoirs (interstitial and nanotube water) – as seen in the T_2 projection for a 1.1nm sample at 285 K. Plots are rescaled accordingly to improve visualization

In the conventional 1D NMR diffusion experiments in a constant magnetic field gradient, the self-diffusion coefficient is obtained by appropriate fitting the ^{1}H NMR spin-echo decay data [45]. However, in the case of nonuniform diffusion processes with multiple D values, diffusion is given by a distribution function f(D), which can be obtained by implementing an appropriate 2D inversion algorithm, as explained before. The advantage of the D-T_2 spectroscopy is that the self-diffusion coefficient of the nanotube water can be resolved by analyzing the spin-echo decay signals in different T_2 windows.

Figure 65 shows the 2D NMR D-T_2 spectra of four characteristic samples measured in this study, at 270K and 285K. The NMR contour plots are rescaled accordingly to improve visualization. Two main signals are visible acquiring different T_2 values, i.e. 0.5 ms and 10 ms, respectively. The short T_2 signal is assigned to the water inside the CNTs [97], while the long T_2 signal is assigned to interstitial water, i.e. external water confined in the space between CNTs, which are assembled in CNT-bundles, as explained in detail in ref.[101]. It is noticed that at room temperature, the long T_2 signal component includes interstitial as well as bulk water; the latter in the very strong constant magnetic field gradient acquires an effective T_2 value $\approx$ 10 ms, which is sufficiently shorter than $T_2 \approx 2$ s in a homogeneous magnetic field [102]. Upon lowering the temperature, bulk water freezes and the intensity of the NMR signal from the external water is observed to decrease rapidly. According to Figure 65 and the following Figure 66, the high T_2 value signal, persisting below the freezing temperature of water, is assigned to the interstitial water.

Figure 66, the signal with the high T_2 value persists even below the freezing temperature of water, confirming the assignment of this signal to the interstitial water. It is stressed that normal liquids confined in hydrophilic porous structures acquire short T_2 values and $T_1 \approx T_2$ due to the fast exchange between the slow relaxing bulk liquid and the fast relaxing adsorbed liquid on the porous surface.

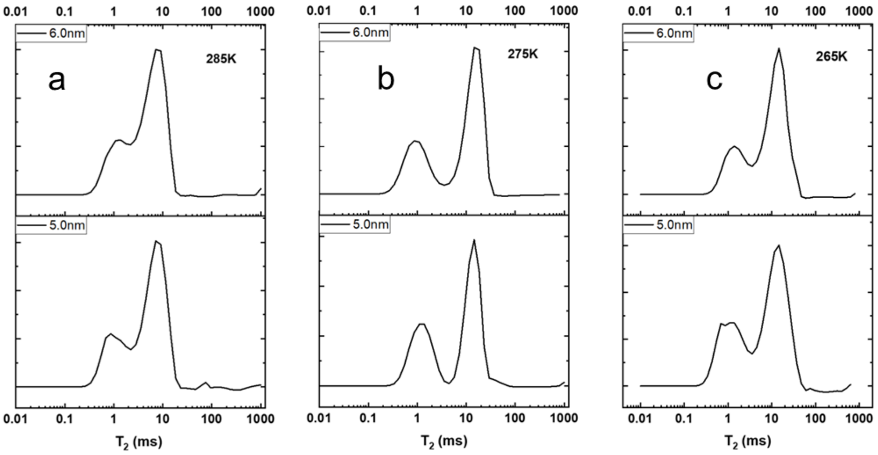

Figure 66. T_2 distributions of water inside 5.0 nm and 6.0nm MWCNT, at three different temperatures (a) 285K (b) 275K and (c) 265K.

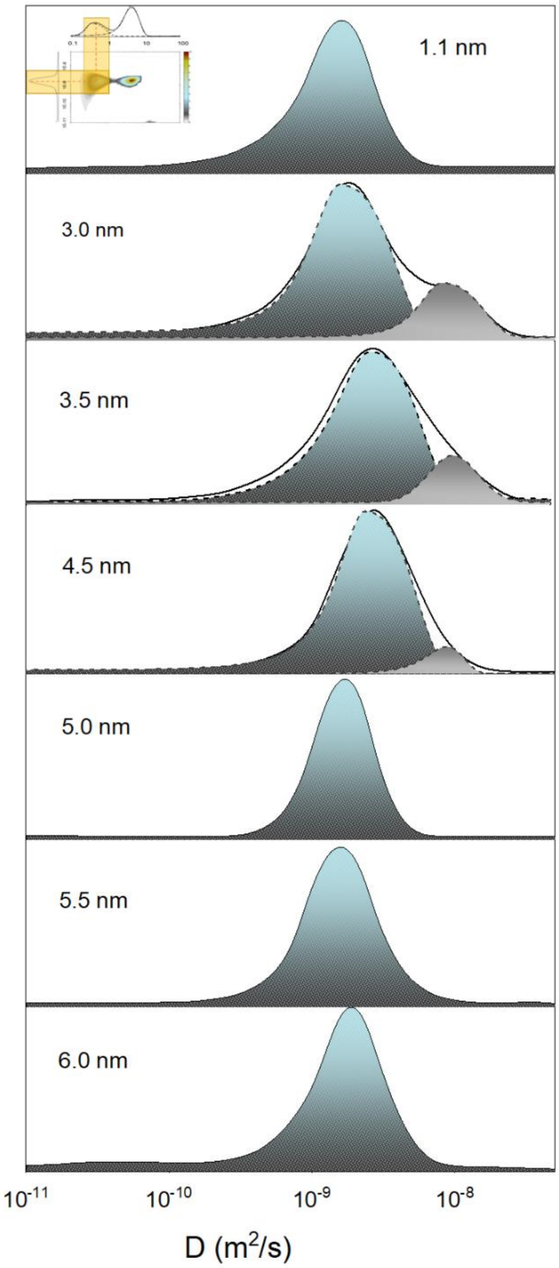

Figure 67. ^{1}H NMR Diffusion projections (solid lines) from the 2D D-T_2 spectra of the internal nanotube water in different CNT sizes, at 285 K. Diffusion projections at certain CNT sizes (3.0nm, 3.5nm and 4.5nm) are resolved into two components (dashed curves), represented by the main and the shoulder peaks

However, when water is enclosed into the hydrophobic CNT walls, the short T_2 values with $T_2 << T_1$ is a strong indication of a solid-like water arrangement [97]. This observation corroborates with the WTS structure in Figure 64 from the MD simulations. To uncover the nanotube water dynamics, we calculated separately the D projections corresponding to the short T_2 signal component. Figure 67 shows the diffusion profile of the nanotube water for all measured samples at 285 K. As seen, the diffusion profile at certain CNT sizes (3.0nm, 3.5nm and 4.5nm) can be fitted with two Gaussians, representing nanotube water groups with different dynamics. Furthermore, in the same CNT size range, the D values of the slow water component are sufficiently higher than those in the rest CNT sizes.

For instance, it is found that D~2.6 $x10^{-9}$ m^2/s in the 3.5 nm CNT, sufficiently higher than D~1.6 x 10^{-9} m^2/s in the 5.5 nm sample. This result is in agreement with previous studies [49, 103], which show that the mean D value of water in small CNT sizes is twice as large than in large CNT sizes. At higher CNT diameters, D acquires the value of bulk water. It is furthermore observed that in most cases the f(D) distribution shows a tail in the direction of the low D values, as expected in the case of one dimensional diffusion processes [47, 101].

In order to understand the split of water dynamics in two components, MD simulations were conducted at room temperature in different sizes of CNTs, to reveal the local density of the water layers and the diffusion coefficients. Results are presented in Figure 68. The stratified water arrangement is clearly seen within the CNTs. In small CNT size of 1.1nm, water molecules form a single tubular layer in agreement to the literature [80]. Due to the hydrophobic interaction between water molecules and carbon atoms of the CNT walls, water molecules of this layer are far from the CNT wall by ~0.3nm. Furthermore, the calculated D values are about ~$0.7x10^{-9}$ m^2/s as seen in Figure 68.

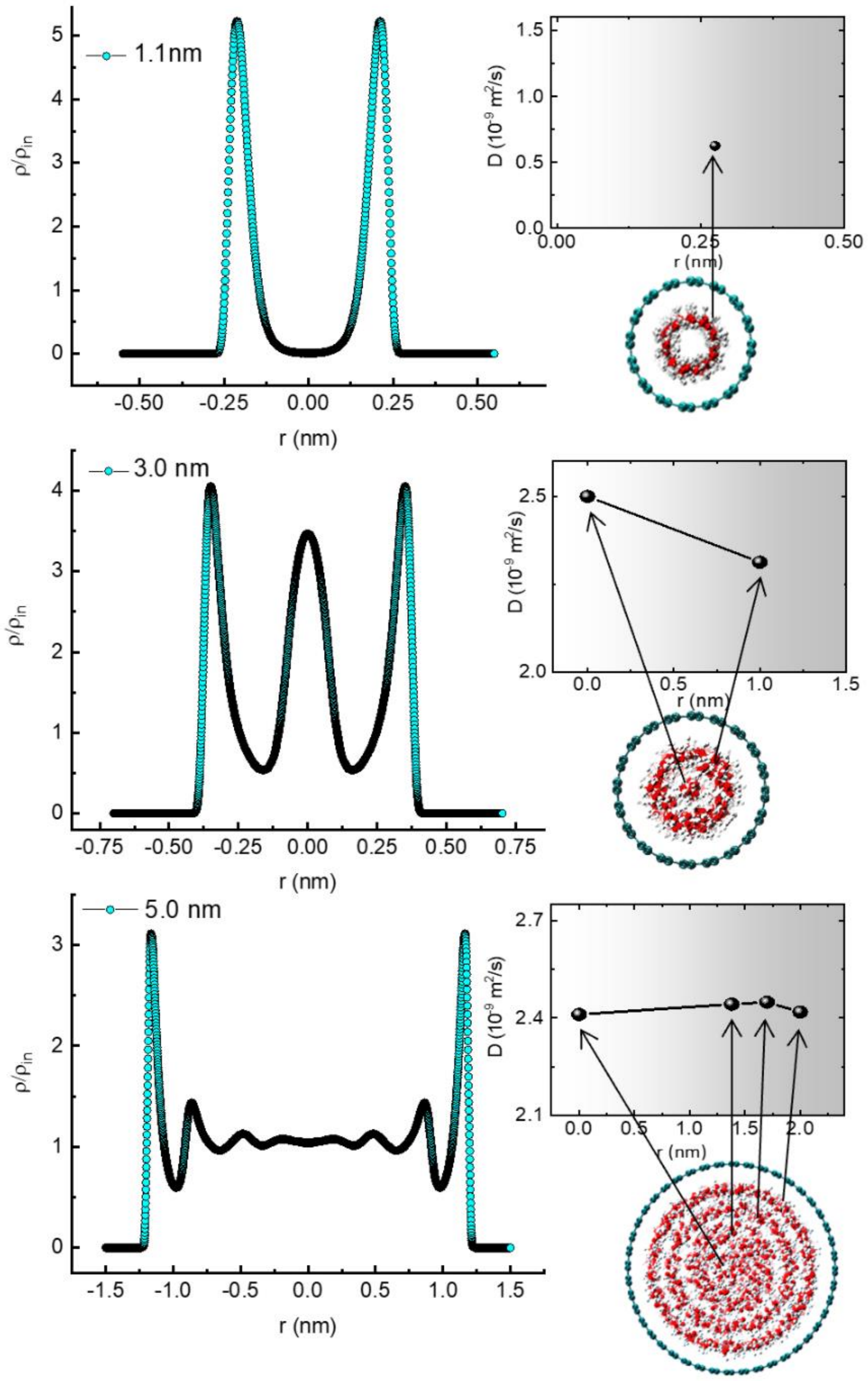

Figure 68. Water local density inside different CNT sizes along with their corresponding models obtained using MD simulations, at room temperature. The x-axis is the CNT inner diameter where zero represents the center of the nanotube. Self-diffusion coefficients for the observed water layers inside CNTs were also calculated.

Upon increasing the CNT diameter, additional water-layers are formed. In the 3.5nm size sample, MD simulations revealed two concentric WTS with different D values in agreement with the NMR results. The water density profiles indicate that the outer WTS close to the CNT wall corresponds to the main diffusion peak in Figure 67, while the central WTS corresponds to the fast diffusion component in .Figure 67. The outer WTS shows a mean D value of ~2.2×10^{-9} m^2/s, in agreement with the NMR results, however, the central WTS differs significantly from the experimentally measured D value at the center of the CNT channel. Finally, in the large diameter sample (5.0nm), although the MD simulation has revealed multiple water layers, their calculated D values are close to each other, unveiling uniform dynamics across the diameter, in agreement to the NMR results of Figure 67. Similar analysis was performed to all samples at various temperatures.

At this point, it is important to rule out diffusion of water molecules in the radial direction of the CNT channels. This is due to the large free-energy-barrier between consecutive layers in the radial direction, which might take values as high as 1-2 kcal/mol [57]. Therefore, radial diffusion is prohibited especially at low temperatures, where molecules do not have sufficient thermal energy to overcome the free energy barrier.

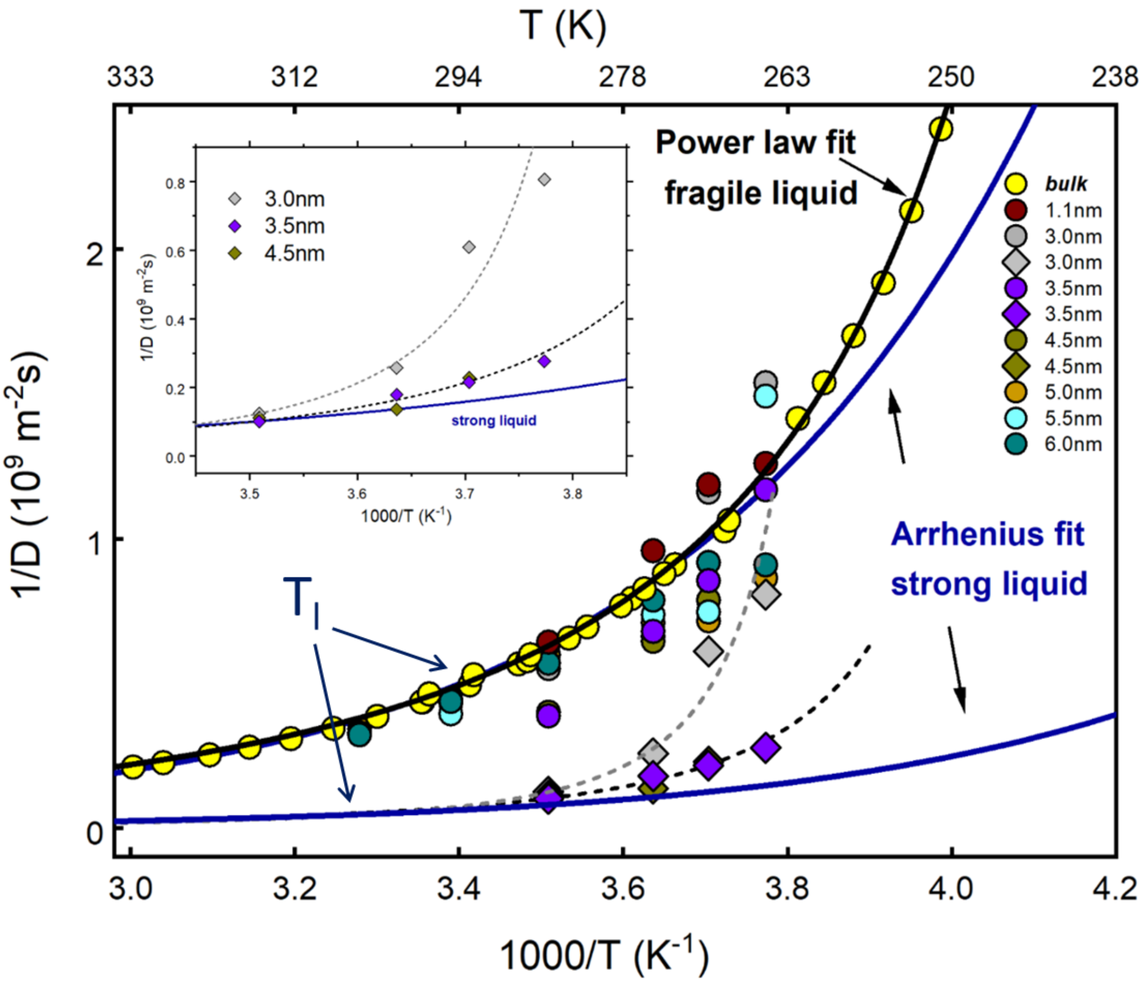

Figure 69. . Experimental 1/D vs. 1000/T of the nanotube water in CNTs of various sizes. The blue lines (in both the main figure and the inset) are theoretical 1/D vs. 1000/T curves of an ideal "strong" liquid obeying the Arrhenius law. The yellow circles and the black line are the experimental values of bulk water and the relevant power law fit. The self-diffusion data of bulk water at temperatures below 260 K were taken from ref [104] . In CNT sizes 3.0, 3.5, and 4.5 nm, two water groups are resolved with different dynamics (slow and fast) with fitting parameters T_s=218 K, γ=--3 (3.5nm, 4.5nm) and γ=-5 (3.0nm). The grey and the black dashed-lines are the power line fits of the data of the fast nanotube water group. The blue arrows are the relevant liquidus temperatures T_l. The inset is magnification of the 1/D vs. 1000/T curves of the fast water component for CNT sizes 3.0, 3.5, and 4.5 nm.

Figure 69 shows the temperature dependence of the inverse of the self-diffusion coefficient 1/D vs.1000/T, of the nanotube water in CNTs with sizes ranging from 1.1 nm to 6.0 nm, in the temperature range of 265K to 305K. The blue lines is the 1/D vs. T curve of an ideal liquid, denoted in the literature as strong liquid [105], which obeys the Arrhenius law

$$\frac{1}{D} = \frac{1}{D_0}\exp\left(\frac{U}{k_B T}\right) \tag{60}$$

For two different initial $1/D_0$ values. Such liquids are denoted in the literature as strong liquids [105] The yellow circles are the experimental values of bulk water; at high temperatures water follows the Arrhenius law, however below the liquidus temperature at $T_l \approx 273K$ Figure 69 strong deviation from the Arrhenius law is observed, while by approaching the glass forming transition temperature, $1/D$ obeys the Arrhenius behavior again[106] Liquids with this kind of behavior are denoted as “fragile” liquids. The high temperature Arrhenious-non Arrhenious dynamic crossover at the liquidus temperature T_l (the temperature above which a material is completely liquid) has been observed in many glass-forming systems [107]

Similar to bulk water, the temperature dependence of the diffusion coefficients of water in our samples shows a non-Arrhenius behavior. Many theoretical explanations have been proposed to explain this behavior, such as the change in the translational and reorientation dynamics [108], the coexistence of high and low-density liquid structures [109, 110], the increasingly collective character of water motions at low temperatures [111] the freezing of some collective motions [112] [113] and a connection of hydrogen-bond exchange dynamics to local structural fluctuations [114]. For a quantitative description of our data we adopted the Speedy-Angell power-law approach, having the following form [20]

$$\frac{\mathbf{1}}{\mathbf{D_{eff}}} = \frac{\mathbf{1}}{\mathbf{D_0}}[\mathbf{T}/\mathbf{T_S} - \mathbf{1}]^{\boldsymbol{\gamma}} \tag{61}$$

where T_s is the thermodynamic limit at which transport properties become zero [115], and the exponent γ may be associated with the existence of cooperative fluctuations within a formation of an open hydrogen-bonded network. The concept of fragility was introduced to describe the degree of concaveness in the temperature dependence plot, where the macroscopic transport coefficient under discussion (for instance the diffusion coefficient D or the viscosity η) or microscopic structural relaxation time was plotted as a function of the reduced temperature T_s/T [115] . Bulk water is considered to be fragile [64] [116], which means that it slows down gradually upon cooling and freezes rapidly near the water glass transition temperature (≈ 140 K). The black line is the power-law fit to the experimental data (yellow circles) of bulk water with T_s=218 K and γ=-2 in agreement with previously reported values [117]. In small and large CNT sizes (1.1, 5.0, 5.5 and 6.0 nm), the nanotube water dynamics is similar to that of bulk water, while in the CNT size range 3.0 nm, to 4.5 nm, two nanotube water groups with different dynamics (slow and fast) are resolved (circles and rhombus). In the 3.5 nm, the ratio of the D values of the fast water component over the slow water component (D_{fast}/D_{slow}) is ~4.0, while for the 3.0 nm and 4.5 nm samples, D_{fast}/D_{slow} is ~2.5 and ~3.5, respectively. The data of the fast nanotube water group (rhombus data points) can be fitted to the Speedy-Angell power-law only when γ values in the range of 2.0-5.0 are considered. This indicates that the fast axial water component attains a very fragile – almost liquid like structure [97], resisting to the formation of hydrogen bonds upon cooling. Besides, the liquidus temperature T_l of the fast water component, i.e. the temperature at which diffusion starts deviating from the Arrhenius behavior [107], shifts to higher temperatures; this kind of behavior resembles the size dependent raise of the melting temperature in single-walled CNTs by decreasing size [118, 119].

It is furthermore noticed that in the 3.0, 3.5 and 4.5 nm samples, the 1/D vs. T curve of the slow water component, deviates from that of bulk water indicating a higher fragility even for the outer WTS close to the CNT walls . It is important to mention that this assignment is different from the picture conveyed by some MD simulation reports [61] where water close to the CNT walls assumed to diffuse faster due to the “ideal” CNT wall assumption that often used in modeling CNT tubes. In those studies, pure hydrophobic interaction between water and CNT walls is typically which however fail to explain the complex spatial heterogeneity regarding the dynamics observed between the central and the outer WTS components revealed by our experiments. In addition, the fast diffusion data, for the 3.0, 3.5 and 4.5nm samples, shown in Figure 69 are assigned to the water molecules located at the center of the CNT channels, exhibiting an ultrafast-diffusion mechanism [95, 120] with D values ranging from two to four times than the corresponding values of the bulk water.

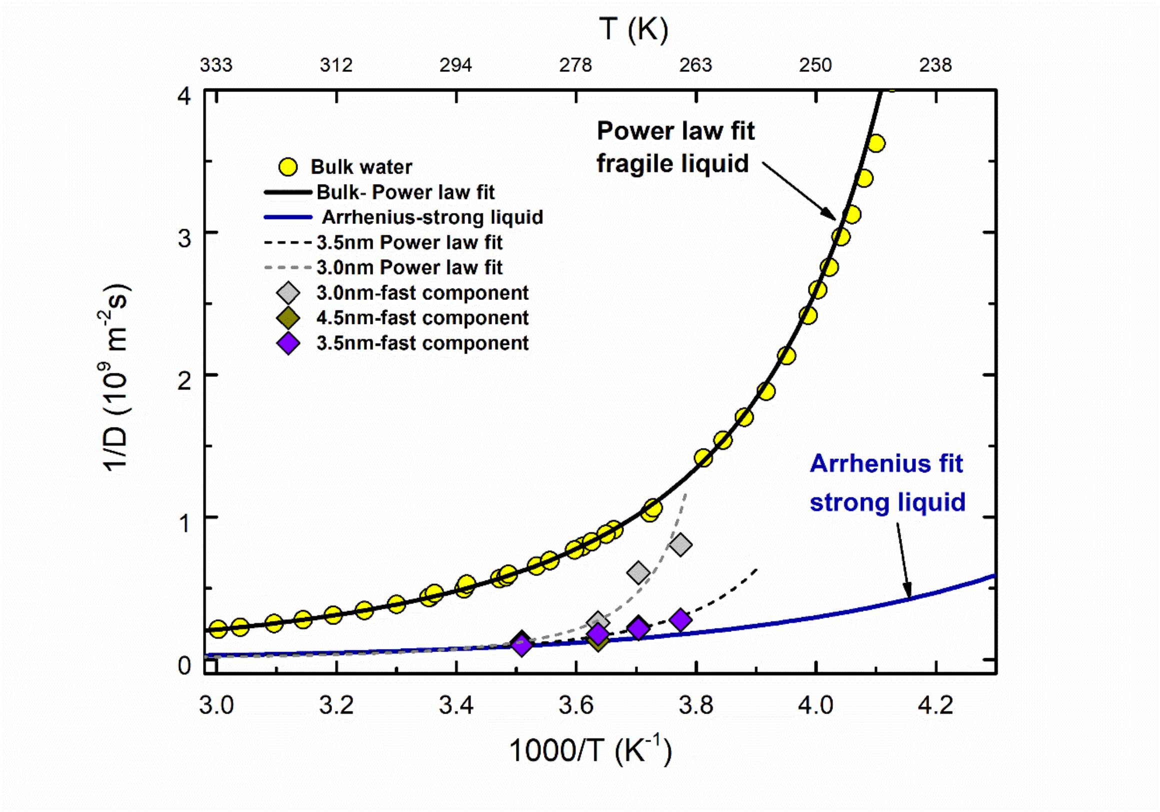

Figure 70. Temperature dependence of the inverse self-diffusion coefficient 1/D as a function of 1000/T of the bulk water (yellow circles).The blue line is the fit of an ideal strong liquid obeying Arrhenius law

The experimental temperature dependent self-diffusion coefficient D of bulk water is shown as yellow circles in Figure 70 The data have been compiled using two data set from the literature within the T range between 298K and 373K of boiling water down to the normal freezing temperature [121] and in the temperature range of supercooled water 298K-238K [104] All data were fitted with the Speedy Angell power law formula $D=D_0[(T/T_s)-1]^{\gamma}$ with fitted parameters $D_0=1.635\ m^2/s$, $T_s=215.05K$ and $\gamma=2.063$. It is seen from the above figure that for bulk water the experimental diffusion coefficient data deviate from the Arrhenius behavior (blue line, strong liquid) to a power law behavior at around 270K, essentially when the bulk water enters the metastable supercooled state below the ‘’normal’’ freezing point.

When water is confined inside the 3.5nm CNT this deviation point moves towards higher temperatures in particular at 285K. Thus the confinement of water this specific diameter obliviates the necessity of supercooling.

It is also observed that the degree of fragility which can be estimated from the γ index, is much higher than that of the bulk fragility. This is clearly seen by the steeper rise of 1/D data points as a function of temperature compared with that of the bulk. It is evident that only for that CNTs diameter there is an appreciable Arrhenius non Arrhenius deviation observed at this high temperature range.

Figure 71 shows the CNT size dependence of the experimental D values of the outer slow diffusing WTS component. A diffusion maximum is observed in the diameter range of 3.0 - 4.5 nm, as also shown in Figure 67. The maximum D value decreases by lowering temperature, indicating the freezing of the diffusion process. It is noticed that the MD simulation results (Black-solid triangle in Figure 71) which represent the D values of water in different sizes of CNT channels, at room temperature, follow excellently the relevant experimental curve. The low D values in the 1.0 nm CNT is caused by the extreme confinement effect and was reported in early studies on water in small CNT sizes [122, 123]

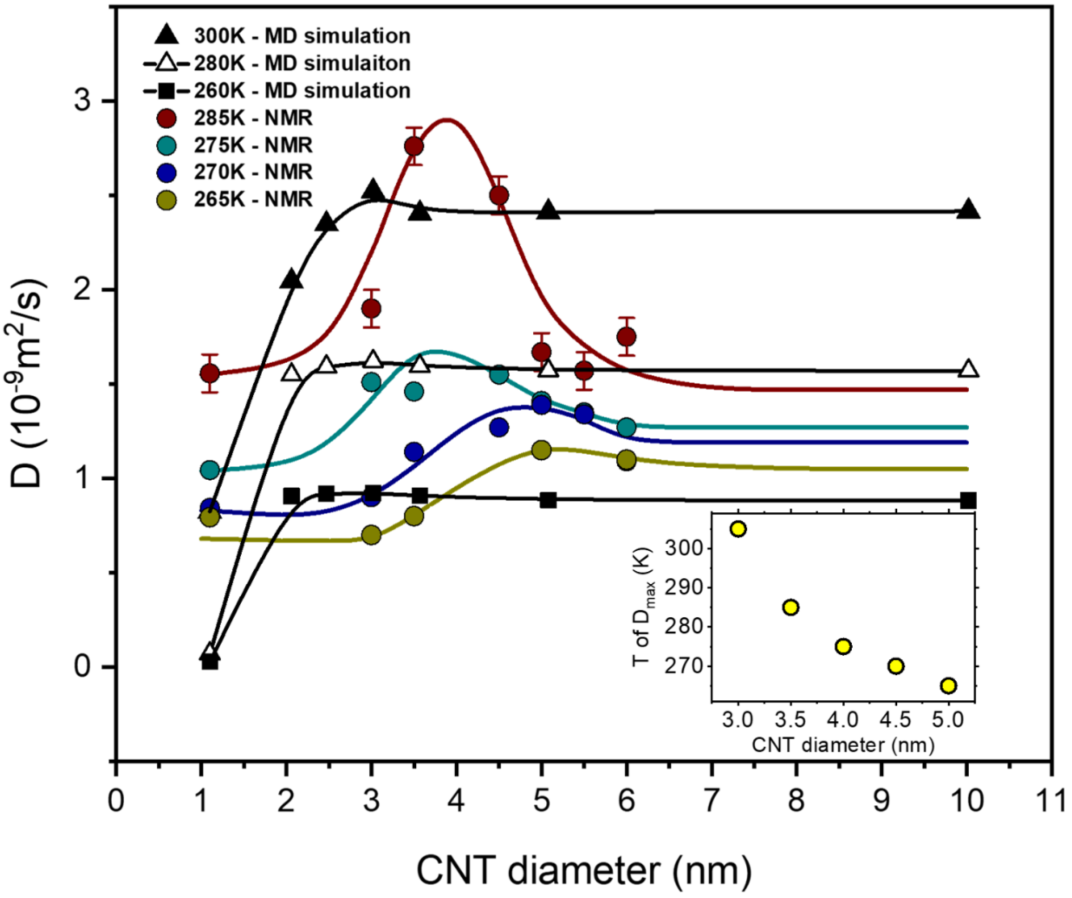

Figure 71. . NMR experimental self-Diffusion coefficients of the shell nanotube water group versus CNT sizes, at different temperatures (285K, 275K, 270K and 265K). The black solid triangles are our MD simulation results, at room temperature which are similar to those previously reported [61]. The lines

are guides to the eye. The inset shows the CNT diameter of maximum diffusion (diffusion peak) at each measured temperature.

Another important observation in the experimental data of Figure 71 is that the position of the diffusion peak depends strongly on both the temperature and the CNTs size. The inset in Figure 71 shows the position of the diffusion maximum D_{max}, in the T vs. d (CNTs diameter) diagram. The highest temperature of D_{max} is observed at d =3 nm. Evidently, this is linked with the anomalously high liquidus temperature observed in this material. By decreasing the CNTs size, atomic scale phenomena appear to control the nanotube water dynamics [119], leading to dynamically heterogeneous fragility [124] and radially depended water mobility [125]

The decreasing of the water dynamics in large CNT sizes dynamics of internal nanotube water beyond 3.5nm CNT size might be related to the fact that in large CNT tubes more stratified water layers are forming as confirmed by our MD results in Figure 71. It is reported [56] that above four or five layers the water gradually loses memory of the CNT wall and tends to acquire again the bulk water structure. Therefore, in large CNT channels, the structure of water molecules at the center of the tubes and the hydrogen bond network resemble that of the bulk water phase.

To the best of our knowledge, this is the first experiment result reporting the existence of a CNT diameter range at which maximum water diffusion occurs. A similar trend is obtained by the MD simulations in Figure 71, also in agreement with previous calculations [56, 59, 61, 80, 126, 127]. However, MD simulations fail to predict the experimentally detected anomalously high D values of the central axial water component. It is important therefore to emphasize the difficulty to quantitatively compare between NMR and MD simulation results: i) in most published MD simulation results, the calculated self-diffusion is based on the total number of water molecules inside the CNT channels (i.e. no water-layer analysis is used); except the present work, and ref. [127], where D is separately calculated, for water molecules close to CNT walls and at the center of the CNTs. ii) dynamical properties reported in MD literature are heavily depending on the water models and potential wells used [56], and iii) due to the computational power limitation, the time accessible to all MD works is in the range of ps to very few ns. On the other hand, in NMR, the accessible experimental time is typically 1-2 orders of magnitude longer than that of MD simulations.

Despite these factors, both MD simulations and NMR experiments show the same size dependence of CNTs water dynamics.

3.3.3 Conclusions

We have presented 2D NMR D-T_2 results of water inside CNTs of different sizes and at various temperatures in combination with MD simulations. Our experiments show in a unique way that a favorable CNT size range (3.0 nm – 4.5 nm) exists, with anomalously enhanced water diffusion. Furthermore, our results show that in this size range the water in the CNTs is further resolved into two components, with the central one exhibiting astonishing transport properties, with D values ranging from two to almost four times than the D values of the bulk water exhibiting astonishing transport properties, with extraordinary high liquidus temperature. Evidently, atomic scale interactions dominate water dynamics in this CNTs diameter range giving rise to the heterogeneity in the fragile behaviour between the central and the outer components of the confined water. The origin of this behaviour can be traced to the interrelation between the strength of the repulsive part of the interatomic potential and the liquid fragility [128] as well as to the associated hydrogen bond lifetimes of water within the carbon nanotubes nanotubes [129]. These nanotube water groups exhibit a non-Arrhenius 1/T temperature dependence signaling a fragile liquid behavior with a stronger fragility compared with that of the bulk water. According to the MD calculations the slower nanotube water component is the one close to the CNT wall. Furthermore, the experimental D values of the slower water component match excellently with those predicted by the MD simulations. To the best of our knowledge, this is the first experiment result reporting on the existence of a CNT diameter range at which maximum water diffusion occurs and simultaneously exhibiting a size dependent liquid fragility. In general, the existence of new phases of water inside CNTs can add a new prospective in the field and it is an important finding on the design of nano-channels for membrane separation and drug delivery systems.

4. Ionic Liquids

4.1 Introduction

Room-temperature ionic liquids (RTILs), materials composed entirely of ions in the liquid state at room temperature, have attracted much attention in recent years because of their unique and tunable properties which render them promising green alternatives for a broad range of applications. Ionic liquids (ILs) can effectively substitute the hazardous organic solvents, and are considered to be much more environmentally friendly due to their very low volatility. Systems of ILs confined within porous solids reveal great potential for applications in gas separation systems, lubricants, nanocomposites, capacitors, fuels and solar cells. The performance of these devices relies critically on the ionic transport of RTIL at the nanoscale.

NMR spectroscopy has proven to be an important non-invasive tool for investigating the dynamics and transport properties of ILs. In general NMR spectroscopy is widely used to study molecular conformational and rotational dynamics and orientational order in Ionic Liquid. In particular, Stray Field Gradient NMR experiments allow the translational diffusion coefficient (D_T) of both the cation and anion species of ILs to be directly measured.

In this chapter we report NMR results of ^{1}H relaxation rates and diffusivities of BMIM TCM in bulk and in confined geometries inside mesoporous silica materials (MCM-41 and SBA-15). Measurements were conducted in the fringe field of a 4.7T superconducting magnet providing a 34.7 T/m linear magnetic field gradient in the temperature range of 100K to 400K. The rotational and translational dynamics of BMIM TCM confined in MCM-41 and SBA-15 have been studied as a function of temperature by measuring both ^{1}H T_1 and T_2 relaxation times and Diffusion coefficient D_T measurements. These results are then compared with values obtained for the bulk substances.

Furthermore, the heating cycles of the samples that were implied in order to investigate the effect of thermal treatment. The measurements revealed the presence of 2 minima in the heating process which are attributed to the occurrence of corresponding phase transitions and to the direct connection of the correlation times of the different proton groups.

4.2 Studies of the Reorientational dynamics derived from temperature dependent NMR diffusion and relaxation data of Ionic Liquid and supported in two Mesoporous materials

Water and a number of liquids, have been studied in geometrical confinement for decades, and their behavior can be considered as reasonably well understood. They are subject to two concurring effects, the presence of the surface and the geometrical aspect of restricted space itself. While the latter affects thermodynamic properties such as melting point and glass transition temperatures, the former possesses the potential, depending on the nature of the solid surface, to enhance or reduce molecular order, and to restrict or even promote mobility on a molecular scale[130].

Room-temperature ionic liquids (RTILs) are organic salts with low melting points, which usually consist of large asymmetric organic cations, such as imidazolium, pyridinium, quaternary ammonium, or phosphonium, paired with inorganic or organic anions exhibiting a varying degree of complexity. RTILs have attracted much attention in recent years because of their unique and tunable properties which render them promising alternatives for a broad range of applications such as LI-on batteries, super capacitors, solar cells, gas absorption etc[130-133]

Information about the microscopic structure of RTILs can contribute substantially to the understanding of certain physicochemical, thermo-physical and transport properties of ionic liquids such as viscosity, self-diffusivity and ionic conductivity. The microscopic structure of bulk ILs is a result of the interplay of several types of interactions between the counter-ions. In particular, there is a balance between long-range strong electrostatic interactions among cationic head-groups and anions, hydrogen bonds (H-bonds), short-range dispersion forces. [134, 135]

ILs can be used both as bulk or within materials that possess large surface to ratio such as porous materials. It is very well established that IL confined within pores has a direct effect on its properties. The ordering and mobility of IL within pores of porous materials showed significant enhancement seen in catalytic activity [136], charge transport [137] and electrical conductivity [138, 139]. Therefore immobilization of ILs in solid porous materials make them more suitable for a broad range of applications. It has been proposed that the confinement changes the cation-anion distances. These interesting changes in the properties of IL is expected due to the effect of the spatial confinement on the ordering of cation and anions within a given IL [140]. Understanding the transport properties as well as the ionic and solvent interactions of ILs enables prediction of their physicochemical properties. The impact of structure, molecular organization, and cation/anion interactions on the physical properties of ILs is still a topic of major research interest. In general Ionic liquids in confinement are studied for plenty of reasons. The understanding of the deviations of microscopic and macroscopic properties of IL in comparison to the bulk is attempted and the behavior of ions in the presence of interfaces is of considerable interest.[141]

For understanding the solvent properties of ILs the characterization and understanding of the molecular motions are just as important as the knowledge of their structure. The recent years have seen a plethora of studies of ionic self-diffusion coefficient and relaxation studies on ILs in bulk such as confined in porous materials. Titania, Nanoporous silica, Carbon Nanotubes, graphene and other mesoporous materials etc. [142-151] are considered as the most suitable matrices for confinement studies. Nanoporous silica is one of the most preferred confining matrix because it is nontoxic and it is easy to synthesize it.[142, 144, 151, 152]

4.2.1 Materials

The RTILs used in this study were 1-butyl-3-methylimidazolium tricyanomethanide BMIM TCM provided by IoLiTech GmbH. The mass fraction purity of the IL was in excess of 98 % while the water content of the employed IL is [BMIM] (720 ppm).

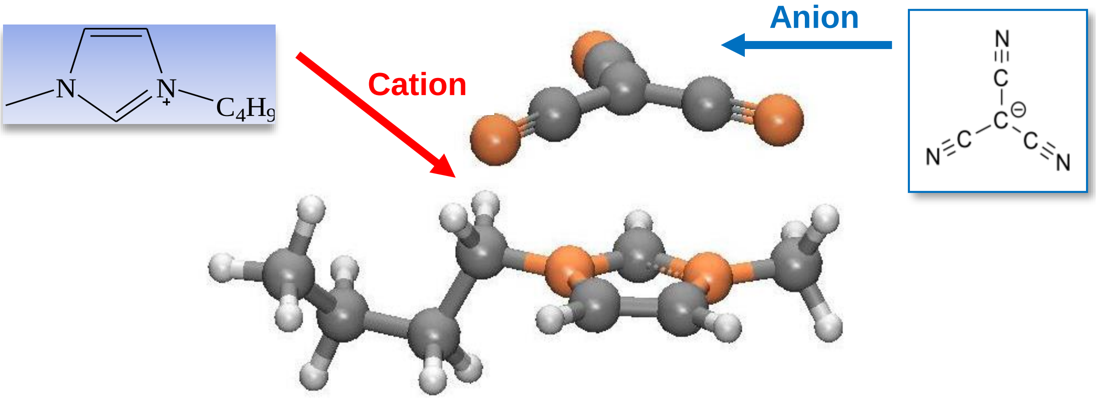

Figure 72. Structure of Ionic Liquid used in this study BMIM TCM

BMIM TCM confined in two different porous media (Mesoporous ordered silicas SBA-15 and MCM-41) is studied in this work [153]. SBA-15 is a porous medium composed by hexagonal-shaped porous and MCM-41 consists of pores of cylindrical geometry. The melting point of an organic salt is considered to have a strong proportional relationship to the symmetry of the ions as by increasing the symmetry of the ion the melting point increases because the ion–ion packing in the crystal cell is more efficient. Imidazolium cation (BMIM) is a low symmetry ion and it causes a distortion from the ideal close packing of the ionic charges in the solid state lattice, a reduction of lattice energy and as a result a depression of the melting point of IL. Furthermore it contain alkyl groups that do not participate in charge delocalization [154].

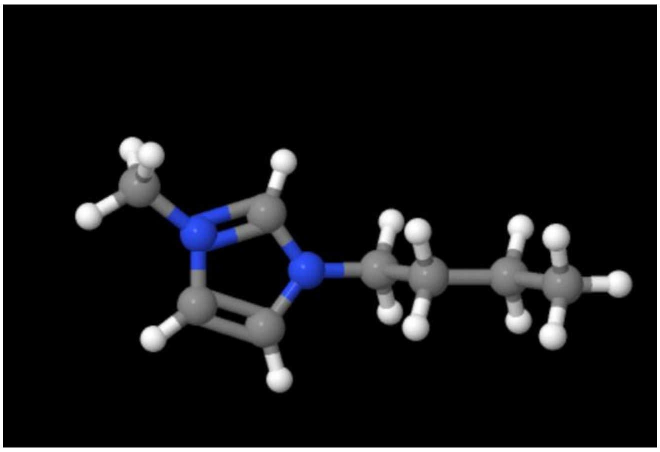

Figure 73. 3D representation of BMIM cation 1-butyl-3-methylimidazolium $C_8H_{15}N_2$

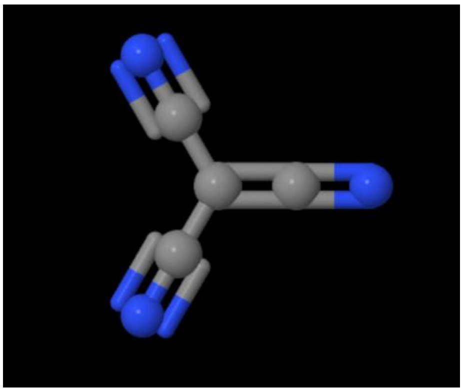

Figure 74. Tricyanomethanide C_4N_3

The BMIM molecule contains fifteen ^{1}H nuclei, chemically bound into five different atomic groups. In this study we were able to provide quantitative details on the molecular dynamics of the liquid and supercooled liquid phases of the BMIM TCM, which should be taken into account when using this IL for specific applications.

For the NMR measurements, the three samples were prepared inside NMR quartz tubes inner diameter 3 mm outer 5mm and length 25 mm. Specifically, IL in the bulk form was inserted into the tube and the for the other two samples IL was immersed with the 2 silica materials and then were let to come to equilibrium at room temperature for a couple of hours. The NMR tubes were then connected to a vacuum system and air was carefully pumped out to ensure IL enters into the Silica porous materials. Subsequently, the NMR tubes were left at ambient conditions for a couple of hours and then each sample was flame sealed under low vacuum. The prepared samples are shown in the following figure.

Figure 75. NMR samples of ILs and IL in SBA-15 and MCM-41

In order to investigate the thermal behavior of the confined RTIL phase, DSC experiments were performed of the ILs in their neat liquid state. The samples were quenched down to -180°C and then heated up to the temperature of 150°C at a rate of 10°C·min^{-1}. The thermographs of the bulk IL BMIM TCM showed only the T_g transition occurring at -84.37°C (188.78K) while neither crystallization nor melting were recorded at higher temperatures as illustrated in Figure 76. In the following table the results of DSC for the bulk substance and confined in 2 different membranes of different pore size are presented.

The non-observation of T_m in the bulk ILs might reflect irregular packing of the ion pairs during the quench step. It has been reported in the literature that imidazolium based ILs ([C_nMIM][X]) bearing alkyl chains of intermediate lengths like the one here in BMIM TCM lead to a wide liquid range (e.g. up to 400°C when BF_4 is the anion), with low freezing points, and the tendency to form glasses upon cooling due to the reduction of lattice energies resulting from less effective packing.[155, 156]

Ionic liquid	Pore size	Membrane	Tg (C)	ΔTg (C)	Tg (K)
[BMIM][TCM]	Neat liquid	-	-84.37	-	188.78
	1 nm	SILM2	-89.88	-5.51	183.27
	10 nm	SILM7	-88.49	-4.12	184.66

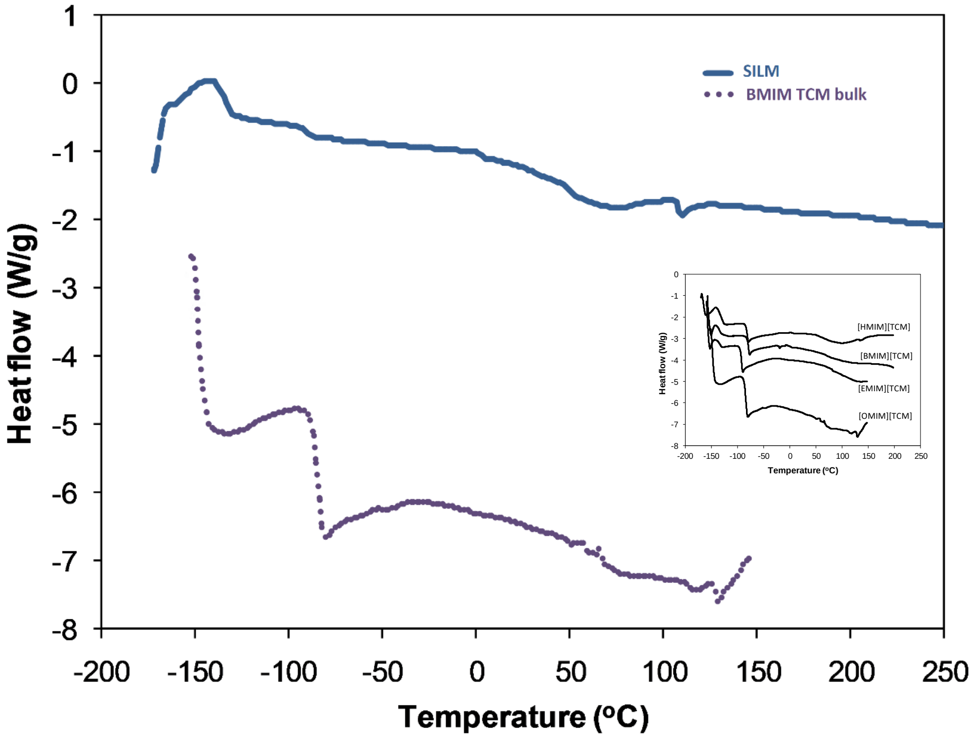

Figure 76. DSC thermographs of the bulk and immobilized (supported) Ionic Liquid BMIM TCM after quenching [156]

4.2.2 T_1 , T_2 and D Diffusion and Relaxation Measurements

^1H NMR relaxation T_1 measurements and the 2D D-T_2 experiments were conducted in the fringe field of a 4.7 T Bruker magnet which provides a 34.7 T/m constant field gradient with ^1H NMR frequency of 101.123MHz. To acquire temperatures down to 100K we used liquid Helium and the stabilization of the temperature acquired by the use of ITC5 National Instruments Temperature Controller. The ^1H NMR T_1 pulse sequence is shown in Figure 77. The pulse sequence used for the T_1 measurements is illustrated in the following figure.

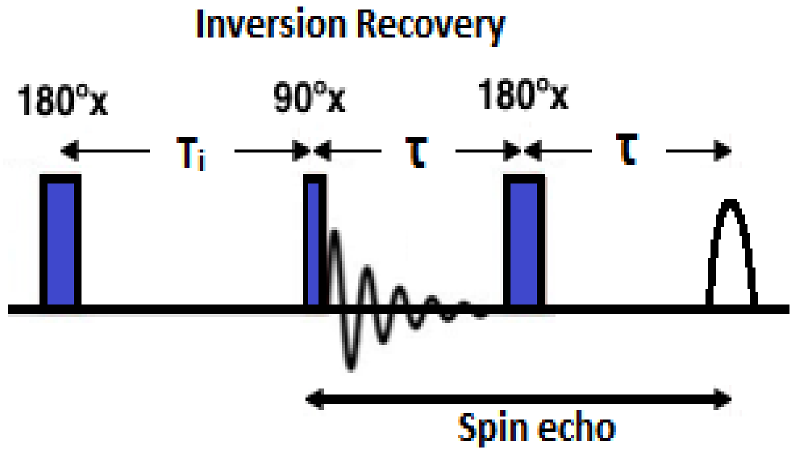

Figure 77. Inversion Recovery Pulse Sequence

It consists of a π - t_1 – $\pi/2$ – echo Inversion Recovery pulse sequence. The $\pi/2$ pulse duration was set to 3μs and the variable delay (time distance) ‘’T_i’’ between the pulses was varying. Overall, 40-50 experiments were performed in order to be able to determine the T_1 relaxation rate. In order to measure the T_1 relaxation rate we cooled the liquid down to 100K and after a waiting period of 2h for stabilization of the temperature we started the T_1 experiments in different temperatures while heating up to 400K. We followed the same procedure for other 2 samples SBA-15 BMIM TCM and MCM-41 BMIM TCM. The obtained data were fitted accordingly using equation 29 (described in the Theoretical part) as shown in Figure 78.

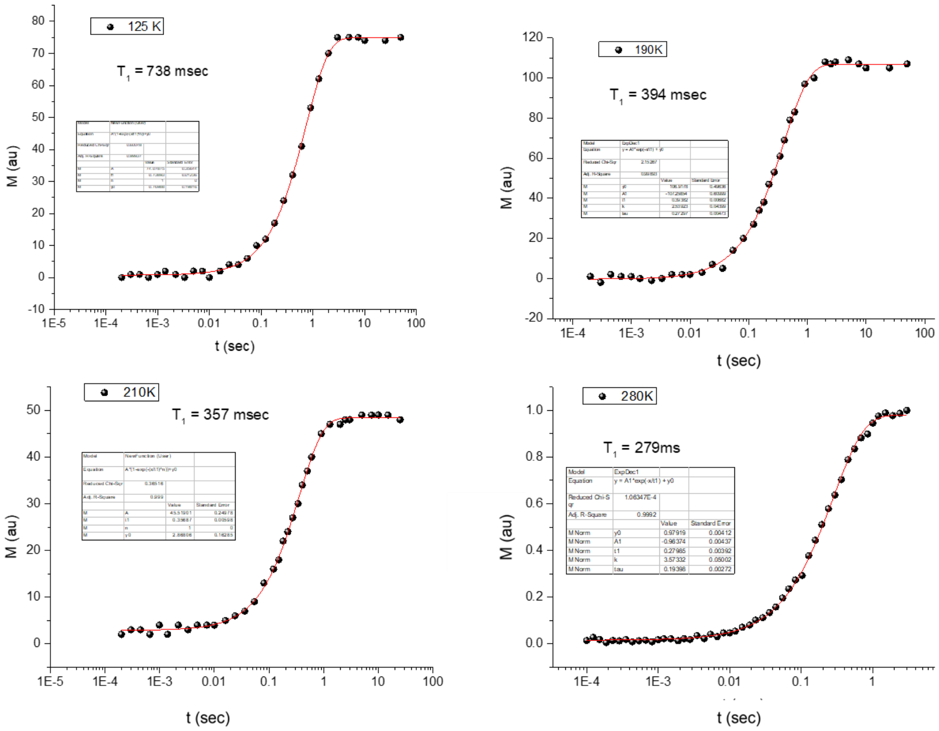

Model	NewFunction (User)		
Equation	A*(1-exp(-(x/t1)^n))+y0		
Reduced Chi-Sqr	0.38516		
Adj. R-Square	0.999		
		Value	Standard Error
M	A	45.51901	0.24978
M	t1	0.35687	0.00598
M	n	1	0
M	y0	2.86806	0.16285

Model	ExpDec1		
Equation	y = A1*exp(-x/t1) + y0		
Reduced Chi-Sqr	1.06347E-4		
Adj. R-Square	0.9992		
		Value	Standard Error
M Norm	y0	0.97919	0.00412
M Norm	A1	-0.96374	0.00437
M Norm	t1	0.27985	0.00392
M Norm	k	3.57332	0.05002
M Norm	tau	0.19398	0.00272

Figure 78. Fitted experimental data of T1 relaxation measurements at selected temperatures

The measurements of the spin lattice relaxation time T_1 as a function of temperature for BMIM TCM and the IL confined in the two mesoporous silica materials are shown in Figure 79. As we can observe in the temperature range between 110 and 280K there is a double minima of T_1 which we will explain later.

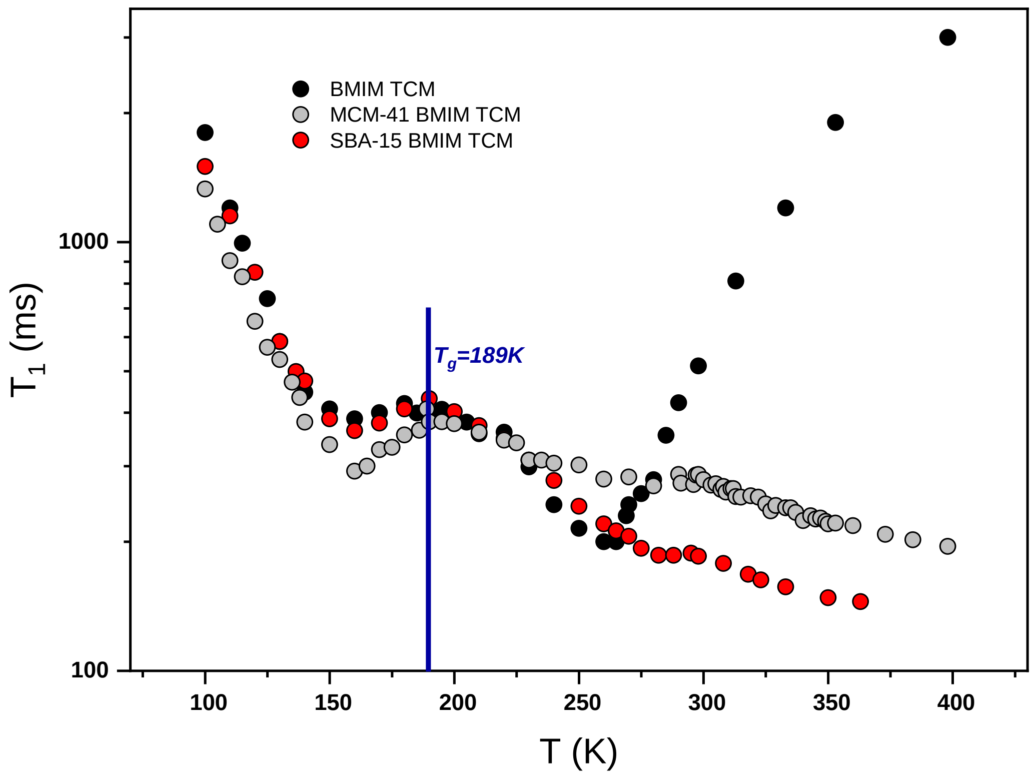

Figure 79. Relaxation time T_1 as a function of temperature during heating from 100K up to 400K

At the same temperature range we performed Hahn spin echo experiments on the three samples by using the ($\pi/2$ - t_1 – π – echo) Hahn spin echo pulse sequence and the $\pi/2$ pulse time duration between the pulses was set to 3μs. The obtained data were fitted accordingly using the exponential equation described in the Theoretical part in chapter 1.1.6 and we derived the diffusion coefficient and relaxation time T_2 as shown in the following figure (Figure 80).

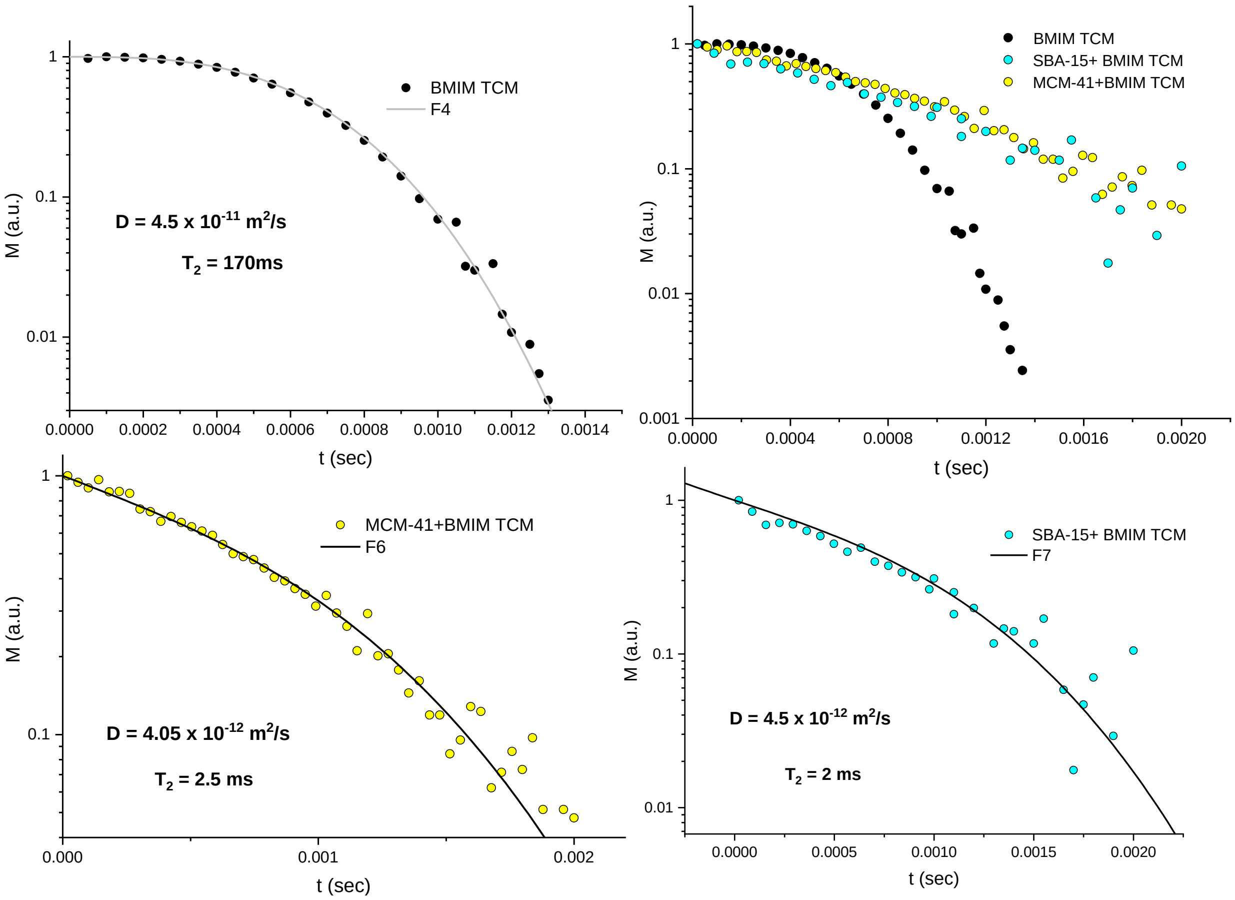

Figure 80. Hahn spin echo measurements for the 3 different samples

The results of T_2 as a function of temperature for BMIM TCM and the IL confined in the two mesoporous silica materials are shown in Figure 81.

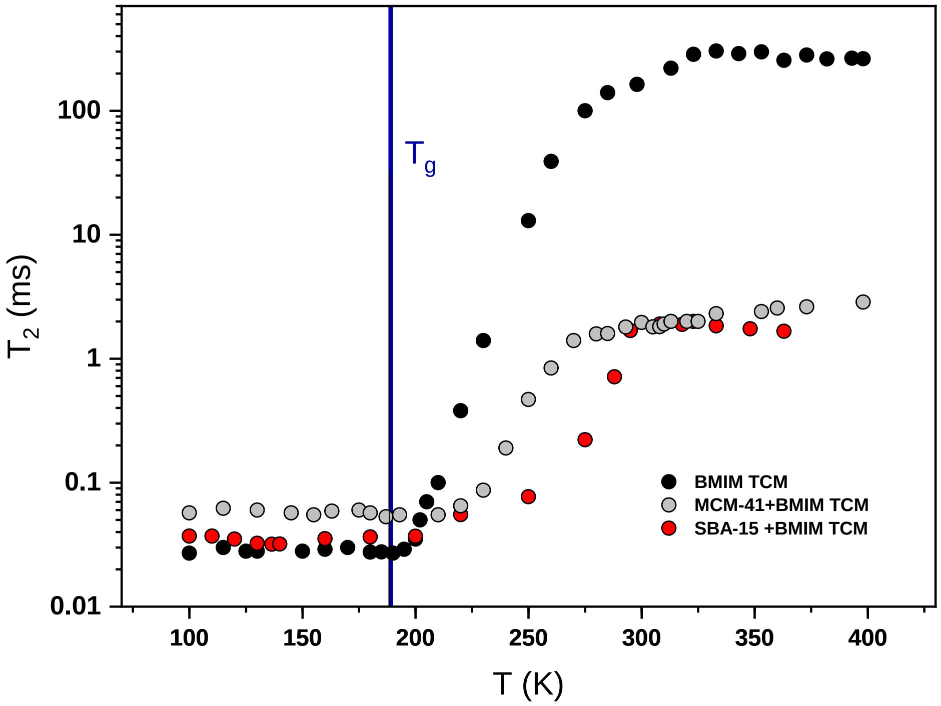

Figure 81. Spin-spin relaxation studies in BMIM TCM and under confinement

The following figure show in a log–linear plot versus 1000/T , the inverse of the self-diffusion coefficient D measured in the present NMR experiments on IL in MCM-41 mesoporous material of 4.5nm (grey circles) and in SBA-15 of 5.6nm (red circles) and for comparison that of pure bulk IL (black circles), measured with the same technique of Hahn spin echo as described above.

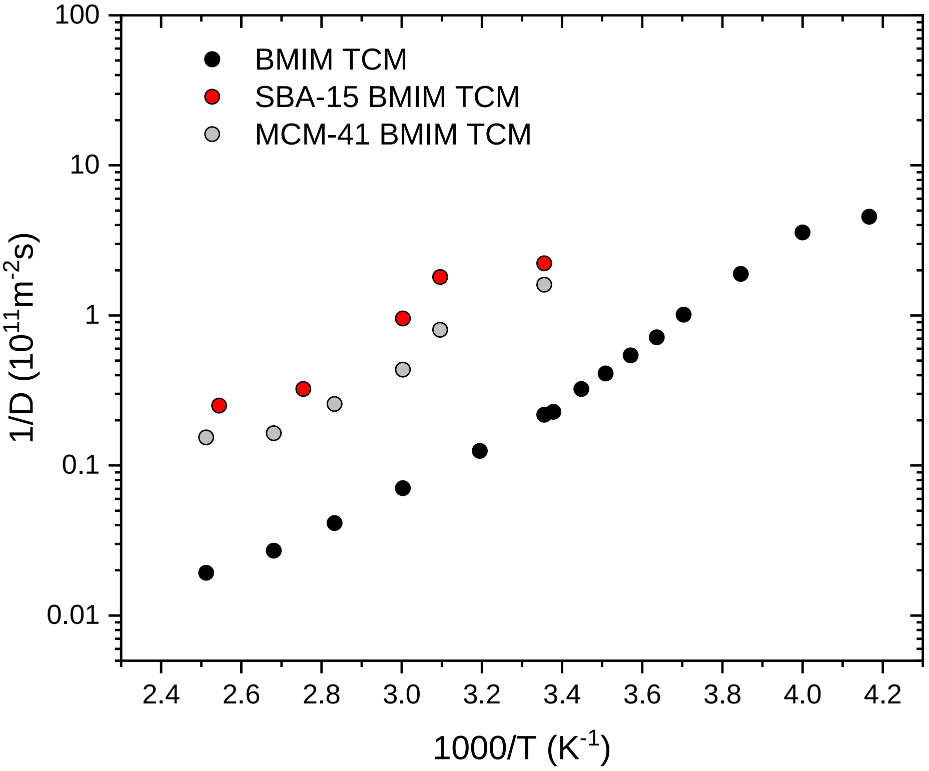

Figure 82. Inverse Diffusion coefficients versus 1000/T as obtained by NMR experiments for bulk and confined BMIM TCM (black circles) in MCM-41 (grey circles) and SBA-15 (red circles)

4.2.3 Relaxation times T_1 T_2

If we consider that the characteristic times of motion of the molecules can be described with the correlation time τ_c that can be considered analogue of the η/T as described in the theoretical part, then the T_1 and T_2 times where $T_1 > T_2$ are given according to Bloembergen, Purcell and Pound (BPP) [3] for the isotropic rotational movement of spins interacting with bipolar interactions, from the following relationships:[4]

$$\frac{1}{T_1} = K\left(\frac{\tau_c}{1+\omega_0^2\tau_c^2} + \frac{4\tau_c}{1+4\omega_0^2\tau_c^2}\right) \tag{62}$$

$$\frac{1}{T_2} = \frac{K}{2}\left(3\tau_c + \frac{5\tau_c}{1+\omega_0^2\tau_c^2} + \frac{2\tau_c}{1+4\omega_0^2\tau_c^2}\right) \tag{63}$$

$$\text{where} \qquad \mathbf{K} = \frac{3\mu_0^2}{160\pi^2}\left(\frac{\gamma^2 h}{r^3}\right)^2 \ \mathbf{for\ spin - 1/2} \qquad \mathbf{(64)}$$

Here, γ is the proton gyromagnetic ratio and the correlation time τ_c of the fluctuation varies with temperature according to the Arrhenius law $\tau_c = \tau_0 \exp(E_\alpha/kT)$ where activation energy E_α for the tumbling motion of molecules in the IL.

Based on the BPP theory, a minimum in the T_1 values occur when the frequency of variations ($1/\tau_c$) of the interaction is equal to the Larmor frequency of the system under investigation. One big advantage of NMR is that it is able to calculate precisely the time of interaction of molecules due to the movement of the molecule whether it is translational or rotational without the need of the theoretical (ab initio) calculations.

In the solid state (low-temperature regime), the hindered molecular motion reflects on long T_1 values observed at large correlation time τ_c, so small tumbling frequency $\omega_0\tau_c >> 1$. On the other side, all correlation in the spin system persist for times short compared with the nuclear Larmor period. This is the extreme narrowing limit $\omega_0\tau_c << 1$. In rapid motion associated with short τ_c, long T_1 values are expected, however the distribution of relaxation times exhibits a minimum at the gyromagnetic frequency in which $\omega_0\tau_c \sim 1$.

In our experimental data we observe two minimum in the values of T_1 in the bulk form of the ionic liquid BMIM TCM. The behavior of bulk material is different for T_1 values with the ones obtained when it is confined into the two silicon mesoporous structures. The minimum in the T_1 data at 260K for 101.123MHz for the bulk form of the ionic liquid is fitted successfully with the BPP theoretical fit.

Considering a single relaxation process, the time correlation function would be insufficient to take into account different relaxation times relevant to motion on different timescales. The LS model-free approach [157, 158] is based on the product of a correlation function for overall tumbling and one for internal motions. While the first one decays exponentially with the overall isotropic rotational correlation time τ_c of the molecule, the latest introduces the generalized order parameter S^2 which describes the spatial restriction of the internal motion with the effective correlation time τ_e. The corresponding spectral density function, assuming isotropic tumbling of the molecule, is given by two Lorentzian terms

$$J(\omega) = S^2 \frac{\tau_c}{1+\omega_0{}^2\tau_c{}^2} + \left(1-S^2\right)\frac{\tau}{1+\omega_0{}^2\tau^2} \qquad \textbf{(65)}$$

where $\tau = \tau_c\tau_e / \left(\tau_c + \tau_e\right)$

The T_1 spin-lattice relaxation times as a function of temperature for BMIM TCM and the IL confined in SBA-15 and MCM-41 are shown in the following Figure. Near transition point at T=260 K, we observe that T_1 experimental values for the BMIM TCM exhibit an inverted-bell shape as well expected by the BPP theory. We fitted our experimental data successfully by using equation 62 in the data range of 240K-400K as shown in Figure 83 where the T_1 minimum is observed. We fitted the correlation time τ_c of the fluctuations with temperature according to the Arrhenius law $\tau_c = \tau_0 \exp(E_\alpha/kT)$ where activation energy E_α for the tumbling motion of molecules in the IL (also shown in Figure 85). The estimated activation energy is E_α=2900K for the tumbling motion derived from the fitted equation. By cooling below 260 K, as fluctuations slow down,T_1 values do not follow the theoretical BPP theory fit. Hence, another relaxation mechanism contribute to the averaged overall relaxation of protons and freezing would be accompanied by an additional process. Indeed, a downturn in relaxation times measured at T=189K indicates that fluctuations persist in a viscous fluid state. Short range ordering of the glassy state and the formation of "agglomerates" add an internal dynamic process to the tumbling motion of the molecules and ultimately shows another local minimum on the T_1 values as temperature of the fluctuations slows down. In agreement with this , we observed that T_1 gradually drops until there is cooling enough to reduce the fluctuations of the methyl protons. At this transition point, detected at T=160 K, the system starts to freeze and the IL finally freezes completely when approaching the lowest temperatures where all movement slow down. Both the observed transition points at 160K and 260K are in agreement with T_g=189K which corresponds to crystallization point at which most of the motions freeze as shown in differential scanning calorimetry (DSC) thermographic measurements. Good fit to the experimental data near 160K were achieved by applying the LS model-free approach with the spectral density function given by equation 65. A single effective correlation time describing the internal motions was calculated to be τ_e=27ns with S=0.1 and the relative activation energy for the composite tumbling motion reaching 720K. By combining these two models in the different temperature regions we obtained the best fit to our experimental data for all temperatures as denoted by the cyan line in Figure 83.

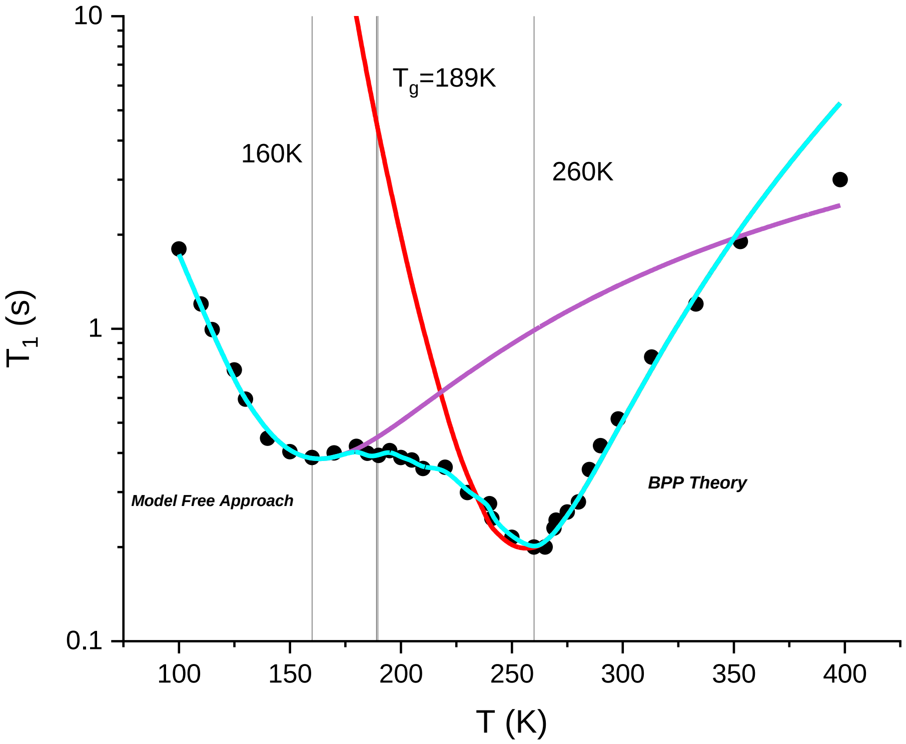

Figure 83. T_1 spin-lattice relaxation time as a function of temperature for BMIM TCM and confined in SBA-15 and MCM-41 silica porous media. The measurements were performed in the stray field of a 4.7 T Bruker superconductive magnet providing a 34.7 T/m constant magnetic field gradient at ^{1}H NMR frequency of 101.123 MHz while heating from 100K. The red and the purple curves are the theoretical fits according to the BBP model and LS model free approach. The cyan curve is the theoretical fit of the applying these two models in the specific temperature ranges.

There are plenty of work in the literature where methyl group reorientations have been studied by NMR methods in many materials [159-161]. These motions are inactive dielectrically and are difficult to measure them, NMR is considered as a technique that can play a unique role here. The low-temperature T_1 local minimum and T_l minima and the T_2 transition at 189K as shown in Figure 84 clearly indicate methyl rotation motions. As a result at temperatures lower than Tg we obtained this interesting type of Methyl group reorientations and we observe a second minimum in T_1 values.

In Figure 84 we can correlate the T_1 and T_2 values versus temperature. In general T_1 values involve the changes in the energy of the spin system and as described before the molecular motions induce these changes most efficiently when the correlation frequencies are comparable with the resonance frequency (BPP theory).T_2 on the other side involve only the decay of the transverse component of the magnetization and it is a purely entropy relaxation thus there is no energy associated with these values.

The cessation of long-range motions is the central fact associated with the glass transition temperature at 189K where the long-range motion does not occur at all below this temperature. T_1 relaxation studies in our IL reveal that some types of local motion do occur below T_g such as the methyl and side-group rotations. Between the area above T_g till 290K it is observed from T_2 that we have a phase transition in the IL.

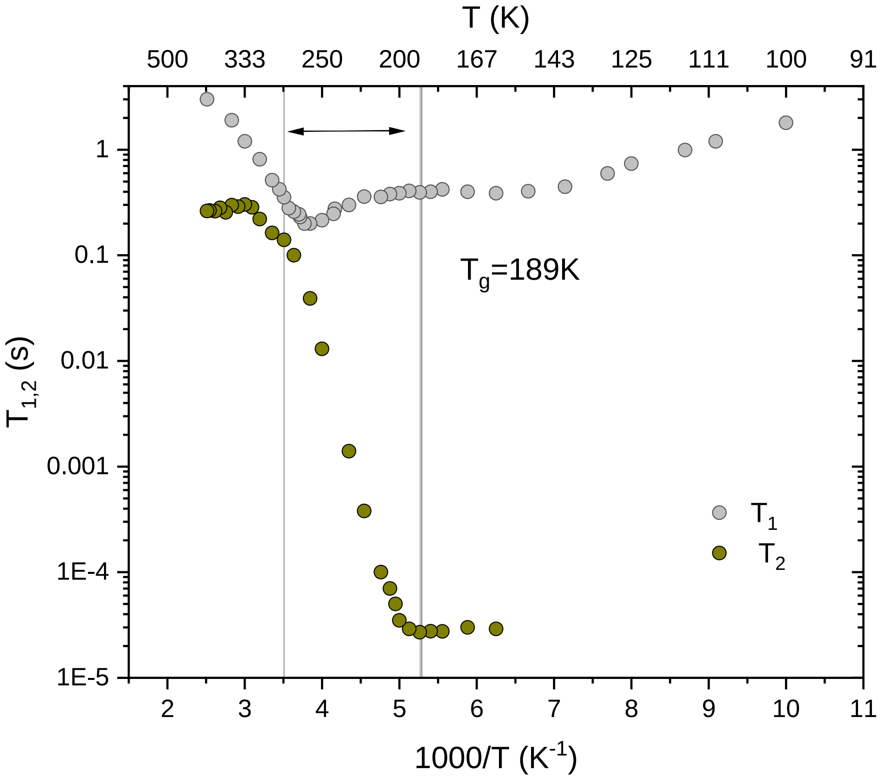

Figure 84. Temperature dependence of ^{1}H NMR relaxation times T_1 and T_2 measured for BMIM TCM

Dynamic heterogeneities have been confirmed by direct observations of T_2 at temperatures well above T_g and until around 290K.

In Figure 85 the calculated correlation times obtained by the two models applied to fit the experimental T_1 relaxation data are shown following an Arrhenius behavior for the BPP and the LS models approach.

The temperature-dependent frequencies $1/\tau_c$ (^{1}H) values calculated by the two mechanisms are shown. From the numerical calculations ($\nu_H = 101.123$ MHz), the T_1 minimums were obtained as $\tau_c = 1.7 \times 10^{-9}$ s and $\tau_c = 0.7 \times 10^{-9}$ s, which is close to the minimum condition $\omega\tau_c = 2\pi\nu_H\tau_c = 0.616$ $\omega\tau_c = 2\pi\nu_H\tau_c = 1.1$ for the two different minimums at 260K and 160K relaxation mechanisms.

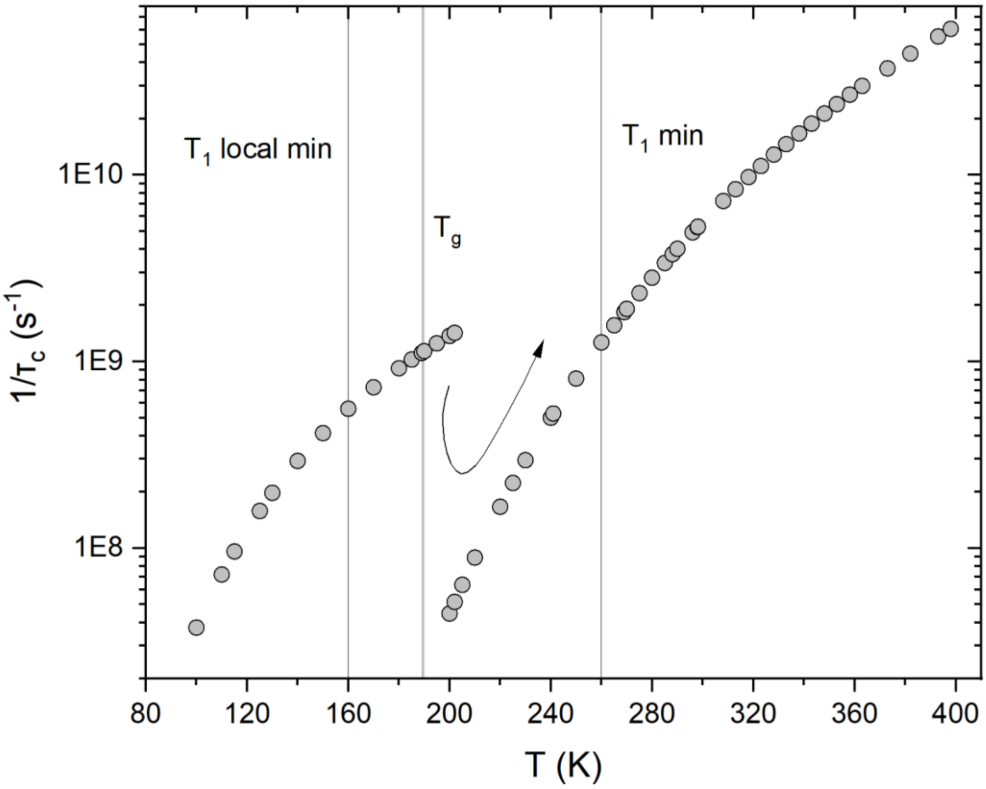

Figure 85. Plot of correlation frequencies obtained by the use of two different models BPP theoretical fit and LS Model Free approach.

As we can observe the difference in the calculation of $1/\tau_c$ by the two different models used the Arrhenius behavior in the calculated correlation times shown that below T_g the calculated correlation times are assigned to the methyl rotations when above T_g where the phase transition occurs the calculated $1/\tau_c$ is assigned to the additional translational motions. Approximately at 189K the calculated τ_c appear to ‘’jump’’ in bigger $1/\tau_c$ values. The low-temperature process is associated with highly hindered methyl rotation and the high-temperature process is the glass phase transition that occurs above T_g. Activation energies are proportional to the slopes of the curves derived from the Arrhenius plots as shown in Figure 86.

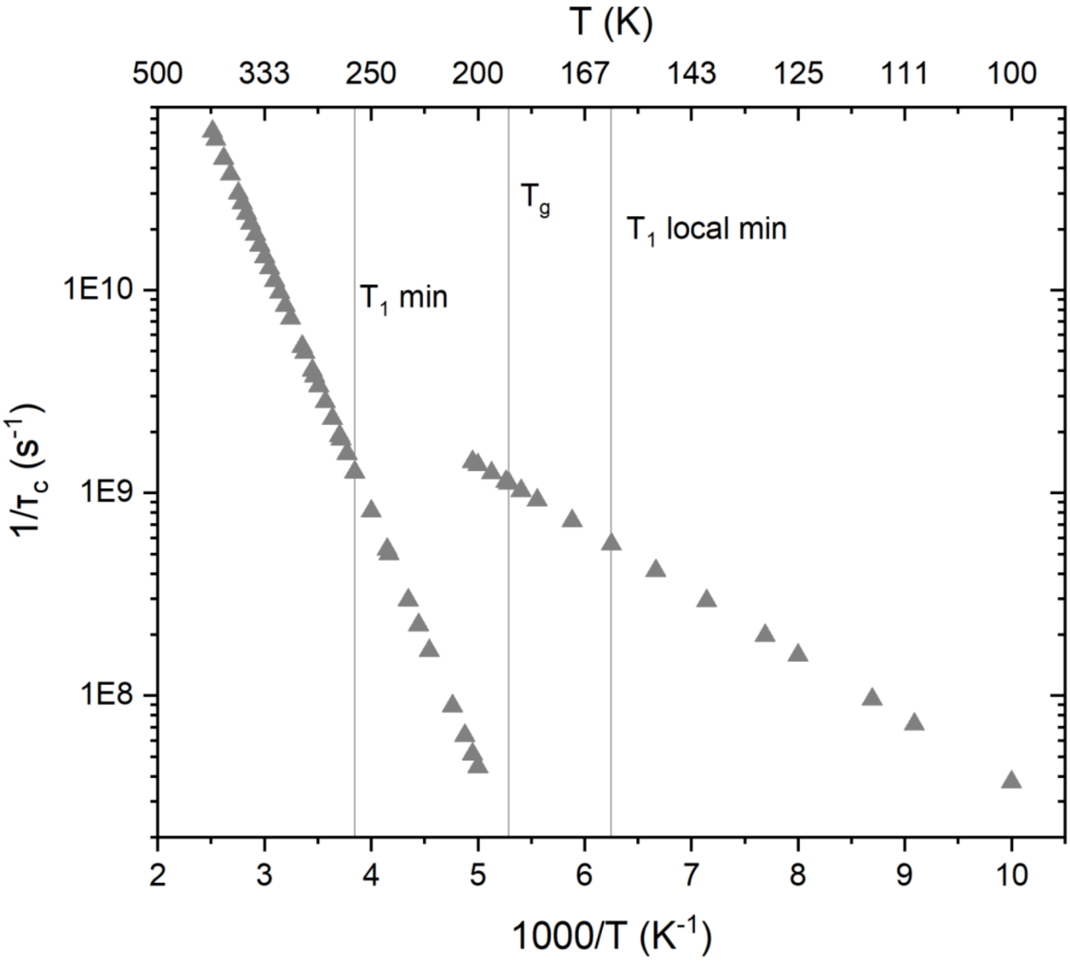

Figure 86. Arrhenius plot of correlation frequencies vs time

Figure 87 shows that all samples exhibit an inverted-bell curve at the same temperature T=160K of T_1 local minimum of the methyl protons. As we can observe T_1 relaxation times appear to be lower when the IL is confined in smallest pores.

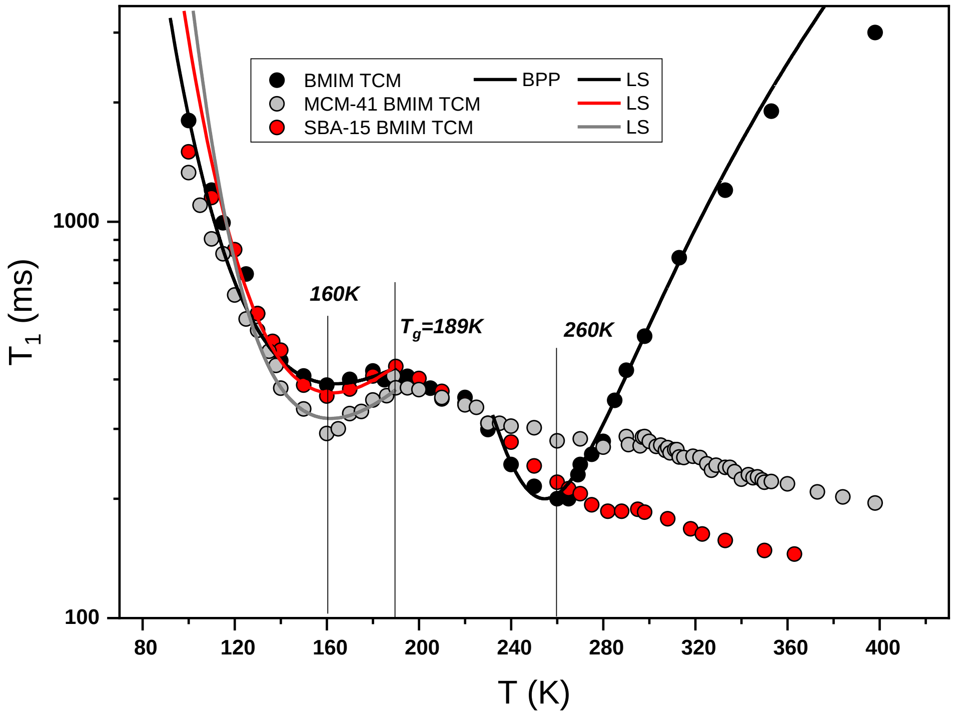

Figure 87. T_1 spin-lattice relaxation time as a function of temperature for BMIM TCM and confined in SBA-15 and MCM-41 silica porous media. The measurements were performed in the stray field of a 4.7 T Bruker superconductive magnet providing a 34.7 T/m constant magnetic field gradient at ^{1}H NMR frequency of 101.123 MHz. The solid black grey and red curves are the theoretical fits according to the BBP model and LS model free approach

Another observation is that correspondingly to the temperature behavior of the time T_1 of the bulk IL when in confinement the minima in the T_1 values is not observed in the area above the T_g temperature of the ionic liquid and below room temperature where the mobility of the molecules increases. This is due to the fact that the τ_c of the molecule has a higher value because the walls do not allow the rapid rotational movement observed in the bulk material at the same temperatures because the rotational movement decreases when we are in confined geometries. The relative activation energies for the composite tumbling motion were calculated with the same procedure as for the bulk mentioned above (reaching 720 K) to be 960 K and 1180 K for SBA-15 and MCM-41, respectively. The results on activation energies near T=160K for the SIL samples indicate that the glass transition point T_g shifts towards lower values than the one for the bulk material as mentioned in the literature [155]. In brief, as we can observe porous silica matrix of different pore sizes and geometry MCM-41 and SBA-15 can change the temperature behavior of T_1 relaxation time. Relaxation times of unconfined and confined IL are found to be different. T_1 relaxation times related to the alkyl chain (T_1 minimum) is less affected while the relaxation times of the aromatic ring of the ionic liquid change more on confinement in small pores (MCM-41/SBA-15). Theoretical calculations of these kind of interactions mentioned in the literature suggest that SiO_2 prefers to interact more with the C-H groups of the cyclic ring of the BMIM rather than those belonging to the tail of alkyl groups of BMIM

4.2.4 Self-Diffusion Coefficient and correlation with viscosity

The temperature dependence of the self-diffusion coefficient was measured. Viscosity (η) of BMIM TCM has been reported [156] and we used them here to see the correlation with the self-diffusion coefficient that we defined experimentally.

Figure 88 shows, in a log–linear plot versus 1000/T , the self-diffusion coefficient D measured in the present NMR experiment on BMIM TCM and the IL confined in MCM-41 nanopores of 4.5nm (yellow squares) and in SBA-15 nanopores of 5.6nm and for comparison all measured with the same technique as mentioned above.

To analyze our data over the temperature range of 240K-400K we tried different models.At first we tried to fit our data with Arrhenius law which is obeyed by strong glassformers which reflects the thermally activated transport over the energy barrier E_a. For our ionic liquid and the two SILs forms we observed that diffusion coefficient values varied more rapidly indicating a fragile behavior. Following these we tested a parabolic law ($D = D_0 \exp[J^2(1/T-1/T_0)^2+E_a/k_BT)]$) which was introduced by Elmatad [162, 163] which was not able to reproduce the experimental data correctly.

The T behavior of the pure bulk ILs was finally successfully fitted with a Vogel–Fulcher–Tamman (VFT) law $D = D_0 \exp[-BT_0/(T - T_0)]$ (as shown by the solid line), where the fitted parameters are shown in Table 1. VFT formula is originally an empirical fit which can be interpreted within the Adam Gibs theory [164]which identifies the T_0 as the temperature where the configurational entropy vanishes, the isoentropic temperature also called Kauzman Temperature. T_0 lies below Tg and it is the temperature where the supercooled liquid would have the same entropy as in the crystalline phase.

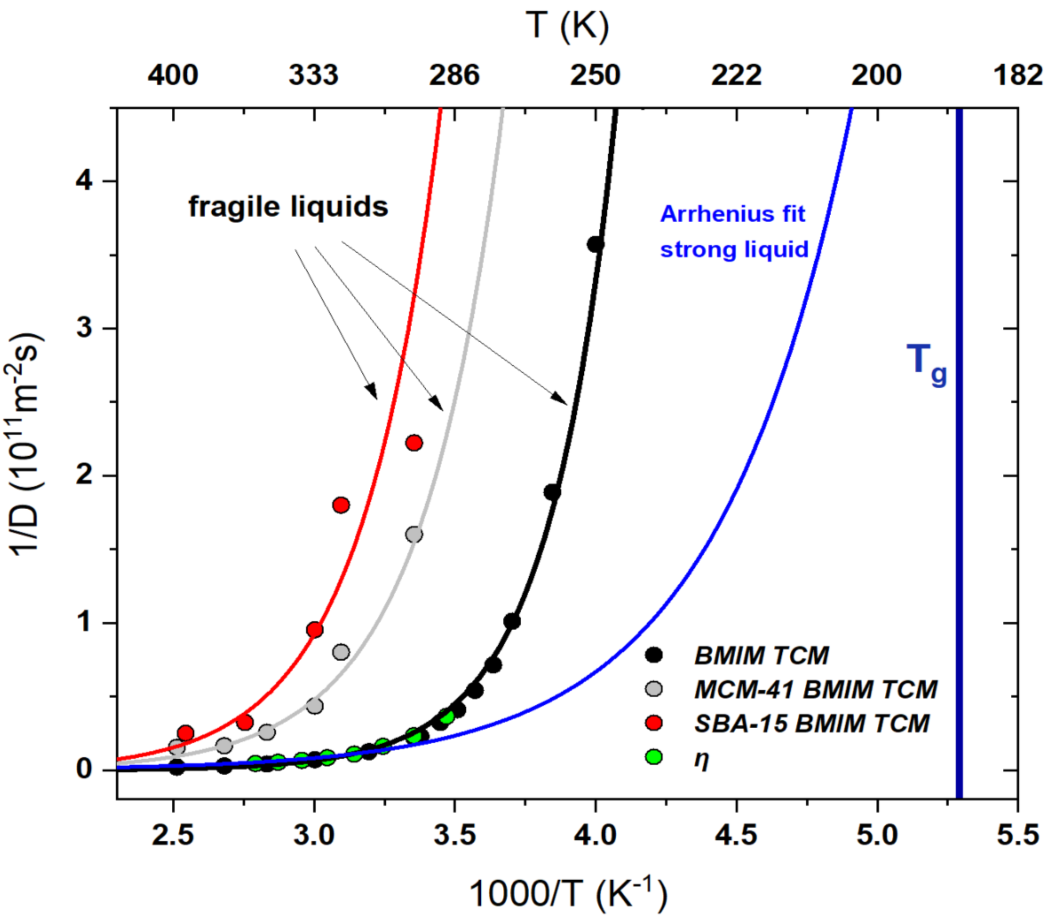

Figure 88 Arrhenius plots of diffusion coefficients for D measured by ^{1}H NMR experiments for BMIM TCM and for the IL confined in SBA-15 and MCM-41. The lines denote fits by VFT equation (black line grey line and red line) for each sample. . The lines were calculated by using the best-fit parameters given in Table 1.

	D_0	*B(K)*	*T_0 (K)*
BMIM TCM	1.6x10E-4	815	160
MCM-41 BMIM TCM	1.00x10E-4	1090	155
SBA-15 BMIM TCM	0.7x10E-4	1170	157

Table 1. Fitted parameters of the VFT formula

T_0 which is typically well below T_g is found to be here 160K for the bulk IL and 155K and 157K for the MCM-41 and SBA-15 matrices correspondingly.

For a more Hydrodynamic approach point of view many studies have focused on the coupling or decoupling between the dynamic quantities such as viscosity (η) and self-diffusion coefficients for translation (D_t) and rotation (D_r).

When molecules follow macroscopic hydrodynamics, the preceding quantities would be related violated through the Stokes–Einstein (SE), $Dt \propto T/\eta$, and Stokes–Einstein–Debye (SED), $Dr \propto T/\eta$, relations, where T is the temperature. These relations are indeed obeyed by many liquids at sufficiently high temperature. However, they might break down at low temperature. To a first approximation the self-diffusion coefficients and reorientational correlation times of the ions should reflect the viscous friction exerted by the surrounding particles. In the case of translational dynamics standard hydrodynamic theory describes this diffusion–viscosity relationship by the well-known Stoles– Einstein (SE) relation mentioned above as:

$$D = \frac{k_B T}{C\pi\eta R_S} \tag{66}$$

where η is the viscosity of the medium, R_S the hydrodynamic radius or Stokes radius of the diffusing particle, and k_B is the Boltzmann constant. The coupling factor $4 \leq C \leq 6$ accounts for the different hydrodynamic boundary conditions at the interface between the diffusing sphere and the medium. The upper bound applies to “sticky” boundary conditions, the lower bound to “slippy” conditions. Based on plausible estimates of the Stokes radii, ILs typically reveal coupling factors between C = 2 and 6, with interesting trends in the cation and anion dependence.

The measured self-diffusion coefficient at different temperatures for BMIM TCM are plotted versus $kT/\pi\eta$ in Figure 89 and as it can be clearly seen that D is proportional to $1/\eta$. The value of cr_s was calculated from this data at two different regions as cr_s =1.3nm and 0.86nm respectively. The van der Waals ls radius of BMIM TCM is considered to be 0.9nm

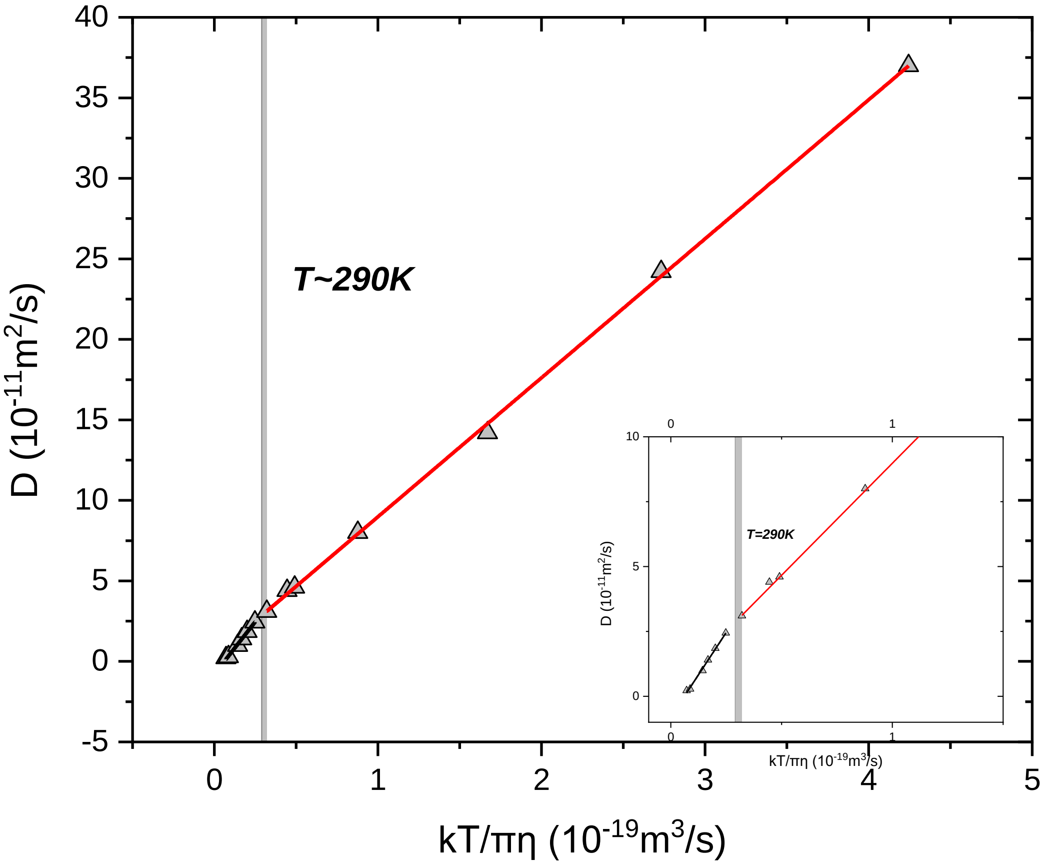

Figure 89. Diffusion coefficient plot versus kT/πη for the BMIM TCM IL. Linear fits are applied for two different regions shown by the red and the blue solid lines and the calculated values of cr$_s$ are 1.3nm and 0.86nm respectively

At a first glance, the observation drives us to the result that Stokes–Einstein relation is obeyed at sufficiently high temperature but around ~1.53Tg (290K), where T$_g$ is the glass transition temperature, thus indicating decoupling between translational diffusion and viscosity.

4.3 Conclusions

Nuclear Magnetic Resonance (NMR) has proved that it is the most suitable non-invasive experimental technique to study confined fluids. The two NMR applications used in this study of confined fluids are diffusion and relaxation experiments which are very sensitive to different time and length scales. NMR relaxation experiments on a constant field gradient gives us useful information about the thermal motions of the molecules and we are able to measure the mean square displacement of the molecules (of the nuclei which has spin). NMR is a powerful technique.

The BMIM TCM relaxation process was studied for IL in two confined environments MCM-41 and SBA-15. It thus becomes critical to find the models that best describes the temperature dependence of diffusion and relaxation rates by using the fewest possible number of fitting parameters. For the diffusion values because two parameters are needed for a simple Arrhenius description, modeling of BMIM TCM behavior requires a minimum of three parameters. We tried three-parameter models only, with the goal of describing the universal physics of these kind of liquids. Finally, the self-diffusion coefficient and the T_1 T_2 relaxation values of BMIM TCM ionic liquid and the IL confined in two porous media were measured and subsequently analyzed using two different models (Free model approach and BPP theory) for the relaxation rates and the Vogel–Fulcher– Tammann (VFT) equation denoted as VFT formula for the diffusion values. The BPP theory is observed in the relaxation rates at high temperatures and above 290K ~1,53Tg however the free model approach theory was necessary to describe relaxation rates when temperature is decreased below these temperature. This is attributed to the appearance of a different relaxation mechanism and the correlation time τ_e which is inserted on the calculations of the correlation time of the molecule due to the onset of a more cooperative dynamics between the methyl proton rotation which persist even in temperatures below Tg.

BMIM TCM ionic liquid was confined in two porous SiO_2 nanoparticles. It is shown that the effect of the confinement in the nanopores leads to a compression of the diffusion rates varying by the size of the pore. The pore size of SiO_2 and the geometry of the pores is a key factor in tuning the diffusion rates and finally all the dynamics of the confined ionic liquid. Finally, it was observed that translational diffusion and viscosity decouple from each other at 1.53Tg temperature.

5. General Conclusions and Future Work

Nuclear Magnetic Resonance NMR is a very powerful technique. Diffusion coefficients (D) and relaxation rates (T_1,T_2) can be readily measured by nuclear magnetic resonance NMR spectroscopy. In the research described in this thesis, NMR is used to study fluids , with emphasis on fluids confined in mesoporous and Nanoporous materials.

A variety of Molecular Dynamics Simulations have been proposed in the scientific literature . This thesis describes experimental results for the first time unveiling the behavior of water confined in constrained geometries, specifically water inside CNTs of different structure (SWCNTs, SWCNTs and MWCNTs) and of different diameters (MWCNTs)

The restricted diffusion of water in this environment gives a diffusion coefficient which is selectable by position considering the hydrophobic nature of CNT walls. Thus, we were able to achieve conducting different kind of experiments the calculation of multiple diffusion coefficients and places where water molecules may possibly move.

Furthermore we were able to identify the temperature dependence and the coupling and the decoupling between the dynamic parameters of the Ionic Liquid BMIM TCM and in confinement in two different silica porous media.

What will happen when an IL is confined in the narrow hollow interior of a Carbon Nanotube? Many reports in the current literature have revealed that ILs possesses properties of both a solid and a liquid and it may be speculated that a transformation of an IL from liquid to solid state will occur if the IL is present in a confined space of a the Hydrophobic nature of the CNT walls.

As an extension of the findings of this PhD thesis we will conduct new temperature NMR experiments with the ionic liquid confined in MWCNTs and the results are going to be combined with Density Functional Theory DFT calculations in order to further examine the dynamics of the IL in confinement. We are aiming to study the behavior of the IL examined in this thesis, 1-butyl-3-methylimidazolium tricyanomethanide BMIM TCM, encapsulated in multiwalled carbon nanotubes (MWNTs) of different diameters. We will examine the confinement effect of MWNTs and the interaction and barrier energies for the encapsulated IL into the CNT and we will correlate the NMR experimental results with the DFT calculations.

In summary, we are going to examine experimentally and theoretically the behavior of IL inside MWCNTs and combine them with DFT theoretical results. Our results will provide a good addition to the development of new types of CNT-based materials, but they also will be helpful for the understanding of phase transitions of ILs in dimensionally confined environments and the related phenomena within the nanoscale.

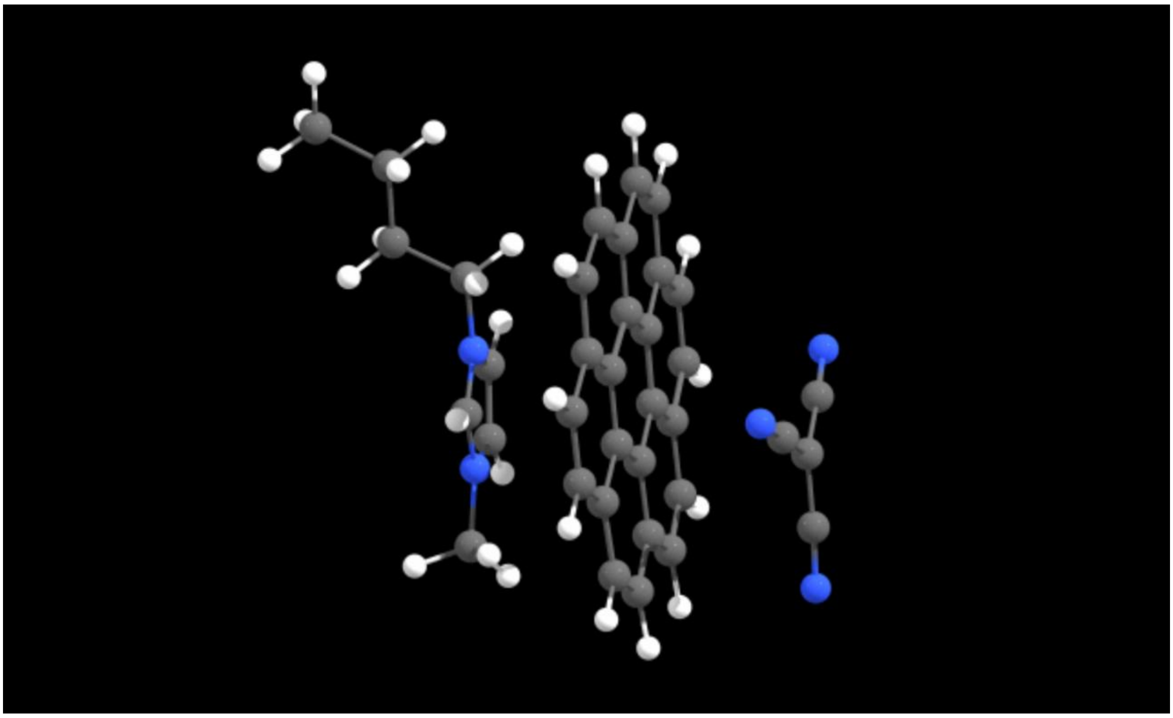

Picture from DFT Calculations (BMIM TCM + CNTs)

6. References

1. Breit, G. and Rabi, II, *On the interpretation of present values of nuclear moments.* Physical Review, 1934. **46**(3): p. 230.
2. Rabi, I.I., *On the Process of Space Quantization.* Physical Review, 1936. **49**(4): p. 324-328.
3. Bloembergen, N., E.M. Purcell, and R.V. Pound, *Relaxation Effects in Nuclear Magnetic Resonance Absorption.* Physical Review, 1948. **73**(7): p. 679-712.
4. Abragam, A. and A. Abragam, *The principles of nuclear magnetism*. 1961: Oxford university press.
5. Slichter, C.P., *Principles of magnetic resonance*. Vol. 1. 2013: Springer Science & Business Media.
6. Callaghan, T.P., *Principles of nuclear magnetic resonance microscopy*. 1993: Oxford University Press on Demand.
7. Fukushima, E., *Experimental pulse NMR: a nuts and bolts approach*. 2018: CRC Press.
8. Levitt, M.H., *Spin dynamics: basics of nuclear magnetic resonance*. 2001: John Wiley & Sons.
9. Duer, M.J., *Solid state NMR spectroscopy.* Blackwell Science Ltd., London, DOI, 2002. **10**: p. 9780470999394.
10. Keeler, J., *Understanding NMR spectroscopy*. 2011: John Wiley & Sons.
11. Bloch, F., *Nuclear induction.* Physical review, 1946. **70**(7-8): p. 460.
12. Kittel, C., P. McEuen, and P. McEuen, *Introduction to solid state physics*. Vol. 8. 1976: Wiley New York.
13. Questions, P. and P. Check, *Pulsed Nuclear Magnetic Resonance: Spin Echoes.* MIT Department of Physics, 2014.
14. Carr, H.Y. and E.M. Purcell, *Effects of diffusion on free precession in nuclear magnetic resonance experiments.* Physical review, 1954. **94**(3): p. 630.

15. Becker, E.D., *High resolution NMR: theory and chemical applications*. 1999: Elsevier.

16. Arrhenius, S., *Über die Dissociationswärme und den Einfluss der Temperatur auf den Dissociationsgrad der Elektrolyte.* Zeitschrift für physikalische Chemie, 1889. **4**(1): p. 96-116.

17. Angell, C.A., *Formation of glasses from liquids and biopolymers.* Science, 1995. **267**(5206): p. 1924-1935.

18. Angell, C.A., *Relaxation in liquids, polymers and plastic crystals—strong/fragile patterns and problems.* Journal of Non-Crystalline Solids, 1991. **131**: p. 13-31.

19. Angell, C.A., *Water II is a" strong" liquid.* The Journal of Physical Chemistry, 1993. **97**(24): p. 6339-6341.

20. Speedy, R.J. and C.A. Angell, *Isothermal compressibility of supercooled water and evidence for a thermodynamic singularity at −45°C.* The Journal of Chemical Physics, 1976. **65**(3): p. 851-858.

21. Mauro, N.A., et al., *A structural signature of liquid fragility.* Nature Communications, 2014. **5**: p. 4616.

22. Einstein, A., *Investigations on the Theory of the Brownian Movement*. 1956: Courier Corporation.

23. Stallmach, F. and P. Galvosas, *Spin echo NMR diffusion studies.* Annual reports on NMR spectroscopy, 2007. **61**: p. 51-131.

24. Wenzel, H., *Editor: E. Roubine, Mathematics Applied to Physics. XIX + 610 S. m. 40 Fig. Berlin/Heidelberg/New York/Paris 1970. Springer-Verlag/United Nations Educational, Scientific and Cultural Organization. Preis geb. DM 58,—.* ZAMM - Journal of Applied Mathematics and Mechanics / Zeitschrift für Angewandte Mathematik und Mechanik, 1972. **52**(9): p. 558-558.

25. Brownstein, K.R. and C.E. Tarr, *Importance of classical diffusion in NMR studies of water in biological cells.* Physical Review A, 1979. **19**(6): p. 2446-2453.

26. McDonald, P.J., et al., *Surface relaxation and chemical exchange in hydrating cement pastes: a two-dimensional NMR relaxation study.* Physical Review E, 2005. **72**(1): p. 011409.

27. Day, I.J., *On the inversion of diffusion NMR data: Tikhonov regularization and optimal choice of the regularization parameter.* 2011(1096-0856 (Electronic)).

28. Tikhonov, A.N. and V.Y. Arsenin, *Solutions of ill-posed problems. 1977.* WH Winston, Washington, DC, 1977. **330**.

29. Mitchell, J., T.C. Chandrasekera, and L.F. Gladden, *Numerical estimation of relaxation and diffusion distributions in two dimensions.* Progress in nuclear magnetic resonance spectroscopy, 2012. **62**: p. 34-50.

30. Butler, J.P., J.A. Reeds, and S.V. Dawson, *Estimating solutions of first kind integral equations with nonnegative constraints and optimal smoothing.* SIAM Journal on Numerical Analysis, 1981. **18**(3): p. 381-397.

31. Maher, A.D. and S.J. Rochfort, *Applications of NMR in dairy research.* Metabolites, 2014. **4**(1): p. 131-141.

32. Lee, J.H., et al., *Two-dimensional inverse Laplace transform NMR: altered relaxation times allow detection of exchange correlation.* Journal of the American Chemical Society, 1993. **115**(17): p. 7761-7764.

33. English, A.E., et al., *Quantitative Two-Dimensional time Correlation Relaxometry.* Magnetic Resonance in Medicine, 1991. **22**(2): p. 425-434.

34. Lee, J.H., et al., *Two-dimensional inverse Laplace transform NMR: altered relaxation times allow detection of exchange correlation.* Journal of the American Chemical Society, 1993. **115**(17): p. 7761-7764.

35. Peemoeller, H., R.K. Shenoy, and M.M. Pintar, *Two-dimensional nmr time evolution correlation spectroscopy in wet lysozyme.* Journal of Magnetic Resonance (1969), 1981. **45**(2): p. 193-204.

36. Song, Y.Q., et al., *T(1)--T(2) correlation spectra obtained using a fast two-dimensional Laplace inversion.* 2002(1090-7807 (Print)).

37. Striolo, A., *The Mechanism of Water Diffusion in Narrow Carbon Nanotubes.* Nano Letters, 2006. **6**(4): p. 633-639.

38. Seland, J.G., *High frequency modulated gradient spin echo diffusion measurements with chemical shift resolution.* 2010.

39. d’Eurydice, M.N. and P. Galvosas, *D–T2 correlation using the inhomogeneity of single sided NMR devices.* Microporous and Mesoporous Materials, 2015. **205**: p. 40-43.

40. d’Eurydice, M.N. and P. Galvosas, *Measuring diffusion–relaxation correlation maps using non-uniform field gradients of single-sided NMR devices.* Journal of Magnetic Resonance, 2014. **248**: p. 137-145.

41. Falk, K., et al., *Molecular Origin of Fast Water Transport in Carbon Nanotube Membranes: Superlubricity versus Curvature Dependent Friction.* Nano Letters, 2010. **10**(10): p. 4067-4073.

42. Lei, S., et al., *Curvature-dependent adsorption of water inside and outside armchair carbon nanotubes.* Journal of Computational Chemistry, 2016. **37**(14): p. 1313-1320.

43. Sekhaneh, W., et al., *High resolution NMR of water absorbed in single-wall carbon nanotubes.* Chemical Physics Letters, 2006. **428**(1-3): p. 143-147.

44. Katsiotis, M.S., et al., *Water Coordination, Proton Mobility, and Lewis Acidity in HY Nanozeolites: A High-Temperature 1H and 27Al NMR Study.* The Journal of Physical Chemistry C, 2015. **119**(6): p. 3428-3438.

45. Kimmich, R., et al., *NMR measurement of small self-diffusion coefficients in the fringe field of superconducting magnets.* Journal of Magnetic Resonance (1969), 1991. **91**(1): p. 136-140.

46. Leu, G., et al., *Fixed and pulsed gradient diffusion methods in low-field core analysis.* 2005(0730-725X (Print)).

47. Callaghan, P.T., K.W. Jolley, and J. Lelievre, *Diffusion of water in the endosperm tissue of wheat grains as studied by pulsed field gradient nuclear magnetic resonance.* Biophysical journal, 1979. **28**(1): p. 133-141.

48. Das, A., et al., *Single-file diffusion of confined water inside SWNTs: an NMR study.* ACS Nano, 2010(1936-086X (Electronic)).

49. Liu, X., et al., *Diffusion of Water Inside Carbon Nanotubes Studied by Pulsed Field Gradient NMR Spectroscopy.* Langmuir, 2014. **30**(27): p. 8036-8045.

50. Hassan, J., et al., *Water inside carbon nanotubes: structure and dynamics*, in *Nanotechnology Reviews*2016. p. 341.

51. Knauss, R., et al., *Pulsed field gradient NMR and nuclear magnetic relaxation studies of water mobility in hydrated collagen II.* Magnetic Resonance in Medicin, 1996. **36**(0740-3194 (Print)): p. 241-248.

52. Ashworth, E.N. and F.B. Abeles, *Freezing Behavior of Water in Small Pores and the Possible Role in the Freezing of Plant Tissues.* Plant Physiology, 1984. **76**(1): p. 201-204.

53. Telkki, V.-V., M. Yliniemi, and J. Jokisaari, *Moisture in softwoods: fiber saturation point, hydroxyl site content, and the amount of micropores as determined from NMR relaxation time distributions*, in *Holzforschung*2013. p. 291.

54. Wang, H.-J., et al., *Temperature-Induced Hydrophobic-Hydrophilic Transition Observed by Water Adsorption.* Science, 2008. **322**(5898): p. 80.

55. Kausik, R. and M.D. Hürlimann, *Sensitivity and resolution of two-dimensional NMR diffusion-relaxation measurements.* Journal of Magnetic Resonance, 2016. **270**: p. 12-23.

56. Alexiadis, A. and S. Kassinos, *Molecular Simulation of Water in Carbon Nanotubes.* Chemical Reviews, 2008. **108**(12): p. 5014-5034.

57. Kolesnikov, A.I., et al., *Anomalously soft dynamics of water in a nanotube: a revelation of nanoscale confinement.* Physical review letters, 2004. **93**(3): p. 035503.

58. Head-Gordon, T. and F.H. Stillinger, *An orientational perturbation theory for pure liquid water.* The Journal of Chemical Physics, 1993. **98**(4): p. 3313-3327.

59. Bordin, J.R., A. Diehl, and M.C. Barbosa, *Relation between flow enhancement factor and structure for core-softened fluids inside nanotubes.* The Journal of Physical Chemistry B, 2013. **117**(23): p. 7047-7056.

60. Joseph, S. and N. Aluru, *Why are carbon nanotubes fast transporters of water?* Nano letters, 2008. **8**(2): p. 452-458.

61. Barati Farimani, A. and N. Aluru, *Spatial diffusion of water in carbon nanotubes: from fickian to ballistic motion.* The Journal of Physical Chemistry B, 2011. **115**(42): p. 12145-12149.

62. Joseph, S. and N.R. Aluru, *Why Are Carbon Nanotubes Fast Transporters of Water?* Nano Letters, 2008. **8**(2): p. 452-458.

63. Striolo, A., et al., *Water in carbon nanotubes: Adsorption isotherms and thermodynamic properties from molecular simulation.* The Journal of chemical physics, 2005. **122**(23): p. 234712.

64. Prielmeier, F.X., et al., *Diffusion in supercooled water to 300 MPa.* Physical Review Letters, 1987. **59**(10): p. 1128-1131.

65. Dehaoui, A., B. Issenmann, and F. Caupin, *Viscosity of deeply supercooled water and its coupling to molecular diffusion.* Proceedings of the National Academy of Sciences of the United States of America, 2015. **112**(39): p. 12020-12025.

66. Perakis, F. and P. Hamm, *Two-Dimensional Infrared Spectroscopy of Supercooled Water.* The Journal of Physical Chemistry B, 2011. **115**(18): p. 5289-5293.

67. Gogotsi, Y., et al., *In situ multiphase fluid experiments in hydrothermal carbon nanotubes.* Applied Physics Letters, 2001. **79**(7): p. 1021-1023.

68. Köhler, M.H. and L.B. da Silva, *Size effects and the role of density on the viscosity of water confined in carbon nanotubes.* Chemical Physics Letters, 2016. **645**: p. 38-41.

69. García-Fandiño, R. and M.S.P. Sansom, *Designing biomimetic pores based on carbon nanotubes.* Proceedings of the National Academy of Sciences, 2012. **109**(18): p. 6939.

70. Geng, J., et al., *Stochastic transport through carbon nanotubes in lipid bilayers and live cell membranes.* Nature, 2014. **514**: p. 612.

71. Chen, Q., et al., *Transition from single-file to Fickian diffusion for binary mixtures in single-walled carbon nanotubes.* The Journal of chemical physics, 2010. **133**(9): p. 094501.

72. Liu, L., et al., *Ultrashort single-walled carbon nanotubes in a lipid bilayer as a new nanopore sensor.* Nature Communications, 2013. **4**: p. 2989.

73. Fornasiero, F., et al., *Ion exclusion by sub-2-nm carbon nanotube pores.* Proc. Natl. Acad. Sci. U.S.A., 2008(1091-6490 (Electronic)).

74. Das, R., et al., *Carbon nanotube membranes for water purification: A bright future in water desalination.* Desalination, 2014. **336**: p. 97-109.

75. Ketabi, S. and L. Rahmani, *Carbon nanotube as a carrier in drug delivery system for carnosine dipeptide: A computer simulation study.* Materials science & engineering. C, Materials for biological applications, 2017. **73**: p. 173-181.

76. Zhang, W., Y. Zhang Z Fau - Zhang, and Y. Zhang, *The application of carbon nanotubes in target drug delivery systems for cancer therapies.* Nanoscale Res Lett, 2011(1556-276X (Electronic)).

77. Costa, P.M., et al., *Functionalised carbon nanotubes: From intracellular uptake and cell-related toxicity to systemic brain delivery.* J Control Release, 2016(1873-4995 (Electronic)): p. 200-219.

78. Ma, S.-B., et al., *Electrochemical properties of manganese oxide coated onto carbon nanotubes for energy-storage applications.* Journal of Power Sources, 2008. **178**(1): p. 483-489.

79. Lee, Y.H., et al., *Applications of carbon nanotubes to energy storage devices.* New Diamond & Frontier Carbon Technology, 2002. **12**(4): p. 209.

80. Alexiadis, A. and S. Kassinos, *Self-diffusivity, hydrogen bonding and density of different water models in carbon nanotubes.* Molecular Simulation, 2008. **34**(7): p. 671-678.

81. Werder, T., et al., *On the Water−Carbon Interaction for Use in Molecular Dynamics Simulations of Graphite and Carbon Nanotubes.* The Journal of Physical Chemistry B, 2003. **107**(6): p. 1345-1352.

82. Holt, J.K., et al., *Fast Mass Transport Through Sub-2-Nanometer Carbon Nanotubes.* Science, 2006. **312**(5776): p. 1034.

83. Chen, J., et al., *Solution Properties of Single-Walled Carbon Nanotubes.* Science, 1998. **282**(5386): p. 95.

84. Kukovecz, A., et al., *A detailed Raman study on thin single-wall carbon nanotubes prepared by the HiPCO process.* The European Physical Journal B-Condensed Matter and Complex Systems, 2002. **28**(2): p. 223-230.

85. Campidelli, S., M. Meneghetti, and M. Prato, *Separation of metallic and semiconducting single-walled carbon nanotubes via covalent functionalization.* Small, 2007. **3**(10): p. 1672-1676.

86. Landi, B.J., et al., *Thermal oxidation profiling of single-walled carbon nanotubes.* Chemistry of materials, 2005. **17**(26): p. 6819-6834.

87. Bonifazi, D., et al., *Microscopic and spectroscopic characterization of paintbrush-like single-walled carbon nanotubes.* Nano letters, 2006. **6**(7): p. 1408-1414.

88. Gogotsi, Y., J.A. Libera, and M. Yoshimura, *Hydrothermal synthesis of multiwall carbon nanotubes.* Journal of Materials Research, 2000. **15**(12): p. 2591-2594.

89. Naguib, N., et al., *Observation of water confined in nanometer channels of closed carbon nanotubes.* Nano Letters, 2004. **4**(11): p. 2237-2243.

90. Ye, H., N. Naguib, and Y. Gogotsi, *TEM study of water in carbon nanotubes.* JEOL news, 2004. **39**(2): p. 2-7.

91. Reiter, G., et al., *Anomalous ground state of the electrons in nanoconfined water.* Physical review letters, 2013. **111**(3): p. 036803.

92. Reiter, G.F., et al., *Quantum coherence and temperature dependence of the anomalous state of nanoconfined water in carbon nanotubes.* The journal of physical chemistry letters, 2016. **7**(22): p. 4433-4437.

93. Matsuda, K., et al., *Water dynamics inside single-wall carbon nanotubes: NMR observations.* Physical Review B, 2006. **74**(7): p. 073415.

94. Kyakuno, H., et al., *Confined water inside single-walled carbon nanotubes: Global phase diagram and effect of finite length.* The Journal of chemical physics, 2011. **134**(24): p. 244501.

95. Das, A., et al., *Single-file diffusion of confined water inside SWNTs: an NMR study.* ACS nano, 2010. **4**(3): p. 1687-1695.

96. Ghosh, S., K.V. Ramanathan, and A.K. Sood, *Water at nanoscale confined in single-walled carbon nanotubes studied by NMR.* Europhysics Letters (EPL), 2004. **65**(5): p. 678-684.

97. Hassan, J., et al., *Ultrafast Stratified Diffusion of Water Inside Carbon Nanotubes; Direct Experimental Evidence with 2D D–T2 NMR Spectroscopy.* The Journal of Physical Chemistry C, 2018. **122**(19): p. 10600-10606.

98. Phillips, J.C., et al., *Scalable molecular dynamics with NAMD.* Journal of computational chemistry, 2005. **26**(16): p. 1781-1802.

99. Berendsen, H., J. Grigera, and T. Straatsma, *The missing term in effective pair potentials.* J. phys. Chem, 1987. **91**(24): p. 6269-6271.

100. Werder, T., et al., *On the water− carbon interaction for use in molecular dynamics simulations of graphite and carbon nanotubes.* The Journal of Physical Chemistry B, 2003. **107**(6): p. 1345-1352.

101. Hassan, J., et al., *Ultrafast Stratified Diffusion of Water Inside Carbon Nanotubes; Direct Experimental Evidence with 2D D–T 2 NMR Spectroscopy.* The Journal of Physical Chemistry C, 2018. **122**(19): p. 10600-10606.

102. Urbán, M., et al., *IR and NMR spectroscopic characterization of graphitization process occurring in the pores of mesoporous silicates in formation of carbon nanotubes.* Journal of molecular structure, 2005. **744**: p. 93-99.

103. Ohba, T., et al., *Rapid water transportation through narrow one-dimensional channels by restricted hydrogen bonds.* Langmuir, 2013. **29**(4): p. 1077-1082.

104. Price, W.S., *Water Signal Suppression in NMR Spectroscopy*, in *Annual Reports on NMR Spectroscopy*, G.A. Webb, Editor. 1999, Academic Press. p. 289-354.

105. Shi, R., J. Russo, and H. Tanaka, *Origin of the emergent fragile-to-strong transition in supercooled water.* Proceedings of the National Academy of Sciences, 2018. **115**(38): p. 9444-9449.

106. Chu, X.Q., et al., *Observation of a dynamic crossover in water confined in double-wall carbon nanotubes.* Phys Rev E Stat Nonlin Soft Matter Phys, 2007. **76(**2 Pt 1): p. 021505.

107. Wen, T., W. Yao, and N. Wang, *Correlation between the Arrhenius crossover and the glass forming ability in metallic glasses.* Scientific Reports, 2017. **7**(1): p. 13164.

108. Rozmanov, D. and P.G. Kusalik, *Transport coefficients of the TIP4P-2005 water model.* The Journal of Chemical Physics, 2012. **136**(4): p. 044507.

109. Xu, L., et al., *Relation between the Widom line and the dynamic crossover in systems with a liquid–liquid phase transition.* Proceedings of the National Academy of Sciences, 2005. **102**(46): p. 16558-16562.

110. Huang, C., et al., *The inhomogeneous structure of water at ambient conditions.* Proceedings of the National Academy of Sciences, 2009. **106**(36): p. 15214-15218.

111. Nicodemus, R.A., et al., *Collective hydrogen bond reorganization in water studied with temperature-dependent ultrafast infrared spectroscopy.* The Journal of Physical Chemistry B, 2011. **115**(18): p. 5604-5616.

112. Gallo, P., et al., *Slow Dynamics of Water Molecules in Supercooled States.* Physical Review Letters, 1996. **76**(15): p. 2730-2733.

113. Swenson, J. and J. Teixeira, *The glass transition and relaxation behavior of bulk water and a possible relation to confined water.* The Journal of chemical physics, 2010. **132**(1): p. 014508.

114. Stirnemann, G. and D. Laage, *Communication: On the origin of the non-Arrhenius behavior in water reorientation dynamics*, 2012, AIP.

115. Ngai, K., *Relaxation and diffusion in complex systems*. 2011: Springer Science & Business Media.

116. Dehaoui, A., B. Issenmann, and F. Caupin, *Viscosity of deeply supercooled water and its coupling to molecular diffusion.* Proceedings of the National Academy of Sciences, 2015. **112**(39): p. 12020.

117. Perakis, F. and P. Hamm, *Two-dimensional infrared spectroscopy of supercooled water.* The Journal of Physical Chemistry B, 2010. **115**(18): p. 5289-5293.

118. Maniwa, Y., et al., *Ordered water inside carbon nanotubes: formation of pentagonal to octagonal ice-nanotubes.* Chemical Physics Letters, 2005. **401**(4): p. 534-538.

119. Pugliese, P., et al., *Freezing Temperatures, Ice Nanotubes Structures, and Proton Ordering of TIP4P/ICE Water inside Single Wall Carbon Nanotubes.* J Phys Chem B, 2017. **121**(45): p. 10371-10381.

120. Kalra, A., S. Garde, and G. Hummer, *Osmotic water transport through carbon nanotube membranes.* Proceedings of the National Academy of Sciences, 2003. **100**(18): p. 10175-10180.

121. Holz, M., S.R. Heil, and A. Sacco, *Temperature-dependent self-diffusion coefficients of water and six selected molecular liquids for calibration in accurate 1H NMR PFG measurements.* Physical Chemistry Chemical Physics, 2000. **2**(20): p. 4740-4742.

122. Mashl, R.J., et al., *Anomalously immobilized water: a new water phase induced by confinement in nanotubes.* Nano Letters, 2003. **3**(5): p. 589-592.

123. Zuo, G., et al., *Transport properties of single-file water molecules inside a carbon nanotube biomimicking water channel.* Acs Nano, 2009. **4**(1): p. 205-210.

124. Richert, R., *Heterogeneous dynamics in liquids: fluctuations in space and time.* Journal of Physics: Condensed Matter, 2002. **14**(23): p. R703-R738.

125. Souza, N.R.d., et al., *Structure and dynamics of water confined in single-wall carbon nanotubes.* Journal of Physics: Condensed Matter, 2006. **18**(36): p. S2321-S2334.

126. Ye, H., et al., *Nanoconfinement induced anomalous water diffusion inside carbon nanotubes.* Microfluidics and Nanofluidics, 2011. **10**(6): p. 1359-1364.

127. Ohba, T., et al., *Fast Water Relaxation through One-Dimensional Channels by Rapid Energy Transfer.* ChemPhysChem, 2016. **17**(21): p. 3409-3415.

128. Pueblo, C.E., M. Sun, and K. Kelton, *Strength of the repulsive part of the interatomic potential determines fragility in metallic liquids.* Nature materials, 2017. **16**(8): p. 792.

129. Hanasaki, I. and A. Nakatani, *Hydrogen bond dynamics and microscopic structure of confined water inside carbon nanotubes.* The Journal of chemical physics, 2006. **124**(17): p. 174714.

130. Gupta, A.K., et al., *Studies on an Ionic Liquid Confined in Silica Nanopores: Change in Tg and Evidence of Organic–Inorganic Linkage at the Pore Wall Surface.* The Journal of Physical Chemistry C, 2014. **118**(3): p. 1530-1539.

131. Broussely, M., et al., *Main aging mechanisms in Li ion batteries.* Journal of Power Sources, 2005. **146**(1): p. 90-96.

132. Balducci, A., et al., *Ionic liquids for hybrid supercapacitors.* Electrochemistry Communications, 2004. **6**(6): p. 566-570.

133. Shi, W. and E.J. Maginn, *Molecular Simulation and Regular Solution Theory Modeling of Pure and Mixed Gas Absorption in the Ionic Liquid 1-n-Hexyl-3-*

methylimidazolium Bis(Trifluoromethylsulfonyl)amide ([hmim][Tf2N]). The Journal of Physical Chemistry B, 2008. **112**(51): p. 16710-16720.

134. Matsumoto, K., et al., *Syntheses, structures and properties of 1-ethyl-3-methylimidazolium salts of fluorocomplex anions.* Dalton Transactions, 2004(1): p. 144-149.

135. Yoshida, Y., et al., *1-Ethyl-3-methylimidazolium Based Ionic Liquids Containing Cyano Groups: Synthesis, Characterization, and Crystal Structure.* Inorganic Chemistry, 2004. **43**(4): p. 1458-1462.

136. Craythorne, S.J., et al., *The co-entrapment of a homogeneous catalyst and an ionic liquid by a sol-gel method: recyclable ionogel hydrogenation catalysts.* 2009(1521-3765 (Electronic)).

137. Iacob, C., et al., *Enhanced charge transport in nano-confined ionic liquids.* Soft Matter, 2012. **8**(2): p. 289-293.

138. Atkin, R. and G.G. Warr, *Structure in Confined Room-Temperature Ionic Liquids.* The Journal of Physical Chemistry C, 2007. **111**(13): p. 5162-5168.

139. Perkin, S., *Ionic liquids in confined geometries.* Physical Chemistry Chemical Physics, 2012. **14**(15): p. 5052-5062.

140. Li, C., et al., *Compression of ionic liquid when confined in porous silica nanoparticles.* RSC Advances, 2013. **3**(25): p. 9618-9621.

141. Ordikhani Seyedlar, A., S. Stapf, and C. Mattea, *Nuclear magnetic relaxation and diffusion study of the ionic liquids 1-ethyl- and 1-butyl-3-methylimidazolium bis(trifluoromethylsulfonyl)imide confined in porous glass.* Magnetic Resonance in Chemistry, 2019. **0**(0).

142. Le Bideau, J., L. Viau, and A. Vioux, *Ionogels, ionic liquid based hybrid materials.* Chemical Society Reviews, 2011. **40**(2): p. 907-925.

143. Dai, S., et al., *Preparation of silica aerogel using ionic liquids as solvents.* Chemical Communications, 2000(3): p. 243-244.

144. Néouze, M.-A., et al., *Ionogels, New Materials Arising from the Confinement of Ionic Liquids within Silica-Derived Networks.* Chemistry of Materials, 2006. **18**(17): p. 3931-3936.

145. Gupta, A.K., et al., *Low density ionogels obtained by rapid gellification of tetraethyl orthosilane assisted by ionic liquids.* Dalton Transactions, 2012. **41**(20): p. 6263-6271.

146. Verma, Y.L., et al., *Ionic liquid template assisted synthesis of porous nano-silica nails.* RSC Advances, 2014. **4**(75): p. 39978-39983.

147. Bellayer, S., et al., *Immobilization of ionic liquids in translucent tin dioxide monoliths by sol–gel processing.* Dalton Transactions, 2009(8): p. 1307-1313.

148. Chen, S., et al., *Morphology and melting behavior of ionic liquids inside single-walled carbon nanotubes.* J Am Chem Soc, 2009. **131**(41): p. 14850-6.

149. Im, J., et al., *Anomalous thermal transition and crystallization of ionic liquids confined in graphene multilayers.* Chem Commun (Camb), 2012. **48**(14): p. 2015-7.

150. Chen, S., et al., *Morphology and Melting Behavior of Ionic Liquids inside Single-Walled Carbon Nanotubes.* Journal of the American Chemical Society, 2009. **131**(41): p. 14850-14856.

151. Zhang, J., et al., *Nanocomposites of ionic liquids confined in mesoporous silica gels: preparation, characterization and performance.* Physical Chemistry Chemical Physics, 2010. **12**(8): p. 1971-1981.

152. Singh, M.P., R.K. Singh, and S. Chandra, *Properties of Ionic Liquid Confined in Porous Silica Matrix.* ChemPhysChem, 2010. **11**(9): p. 2036-2043.

153. Vangeli, O.C., et al., *Grafting of Imidazolium Based Ionic Liquid on the Pore Surface of Nanoporous Materials—Study of Physicochemical and Thermodynamic Properties.* The Journal of Physical Chemistry B, 2010. **114**(19): p. 6480-6491.

154. Wasserscheid, P. and T. Welton, *Ionic liquids in synthesis*. 2008: John Wiley & Sons.

155. Labropoulos, A.I., et al., *Alkyl-methylimidazolium Tricyanomethanide Ionic Liquids under Extreme Confinement onto Nanoporous Ceramic Membranes.* The Journal of Physical Chemistry C, 2013. **117**(19): p. 10114-10127.

156. Tzialla, O., et al., *Phase behavior and permeability of Alkyl-Methyl-Imidazolium Tricyanomethanide ionic liquids supported in nanoporous membranes.* Separation and Purification Technology, 2014. **135**: p. 22-34.

157. Lipari, G. and A. Szabo, *Model-free approach to the interpretation of nuclear magnetic resonance relaxation in macromolecules. 1. Theory and range of validity.* Journal of the American Chemical Society, 1982. **104**(17): p. 4546-4559.

158. Andrec, M., R.M. Montelione Gt Fau - Levy, and R.M. Levy, *Estimation of dynamic parameters from NMR relaxation data using the Lipari-Szabo model-free approach and Bayesian statistical methods.* 1999(1090-7807 (Print)).

159. McCall, D.W. and W.P. Slichter, *Molecular motion in polyethylene.* Journal of Polymer Science, 1957. **26**(113): p. 171-186.

160. McCall, D.W., *Nuclear magnetic resonance studies of molecular relaxation mechanisms in polymers.* Accounts of Chemical Research, 1971. **4**(6): p. 223-232.

161. Powles, J.G. and D.J. Neale, *Molecular Motion in Liquid Toluene by Proton Magnetic Resonance Relaxation.* Proceedings of the Physical Society, 1961. **77**(3): p. 737-747.

162. Elmatad, Y.S., D. Chandler, and J.P. Garrahan, *Corresponding States of Structural Glass Formers.* The Journal of Physical Chemistry B, 2009. **113**(16): p. 5563-5567.

163. Elmatad, Y.S., D. Chandler, and J.P. Garrahan, *Corresponding States of Structural Glass Formers. II.* The Journal of Physical Chemistry B, 2010. **114**(51): p. 17113-17119.

164. Adam, G. and J.H. Gibbs, *On the Temperature Dependence of Cooperative Relaxation Properties in Glass-Forming Liquids.* The Journal of Chemical Physics, 1965. **43**(1): p. 139-146.